Mass composition studies with the low energy extension HEAT at the Pierre Auger Observatory

von

Marcel Straub

Masterarbeit in Physik

vorgelegt der
Fakultät für Mathematik, Informatik und Naturwissenschaften
der
Rheinisch-Westfälischen Technischen Hochschule Aachen

im Januar des Jahres 2012

angefertigt am

III. Physikalischen Institut A

Erstgutachter und Betreuer

Prof. Dr. Thomas Hebbeker
III. Physikalisches Institut A
RWTH Aachen

Zweitgutachter

Prof. Dr. Christopher Wiebusch
III. Physikalisches Institut B
RWTH Aachen

Contents

List of Figures

1. Introduction

At the beginning of the 20th century Victor Hess measured ionizing radiation as a function of height. He found that up to a height of about 1000 m the radiation decreases but beyond that it becomes more intense. His interpretation of the measurements was that a very penetrative radiation from above the atmosphere causes this increasing radiation [1]. The observed ionizing radiation was later called *cosmic rays* by Robert Andrews Millikan. The discovery of cosmic rays was the beginning of high energy physics. It led to several discoveries, e.g. of the positron in 1932 [2], of the Muon (1936) [3] and of the Pion (1947) [4].

Last but not least, cosmic rays are messengers of high energetic processes in the universe. In 1939 Pierre Auger et al. used an array of several Geiger-Müller counters. They found coincidences with distances of up to 300 m between the detectors at high altitudes at the Jungfraujoch [5]. They interpreted the results as *extensive air showers*. The recorded coincidences favour showers with primary energies up to 10^{16} eV. This detection technique is very scalable so it is used in several other experiments. In 1962 the *Volcano Ranch Experiment* observed an event [6] with a primary energy of $1.0 \cdot 10^{20}$ eV.

An alternative approach to observe extensive air showers is the detection of fluorescence light from the excitation of atmospheric nitrogen by charged secondary particles. This method allows to observe the development of the shower. This technique is used by several experiments like *HiRes* (High Resolution Fly's Eye Cosmic Ray Detector) [7]. Due to its calorimetric principle it reduces the uncertainty in the energy determination but provides a smaller duty cycle because it can only operate on moonless and clear nights.

It was realized that both techniques are complementary in many ways and that a combination of both techniques, a hybrid detector, can achieve better results. The Pierre Auger Observatory is such a hybrid detector. With an instrumented area of 3000 km^2 it is also the largest detector of its kind and it is designed to measure extensive air showers in an energy range from 10^{18} to 10^{20} eV and above. The observable centre of mass energy is two magnitudes higher than at the largest available man-made particle accelerator, the LHC. In this energy region the primaries are not expected to be accelerated in our galaxy, because its size and magnetic field are too small to achieve these high energies. The exact energy range where the transition from galactic to extra galactic sources occurs is the subject of current research.

The energy spectrum of the cosmic rays can be well described by a power low $\mathrm{d}N/\mathrm{d}E \propto E^{\gamma}$ with the spectral index γ. Below the Auger energy range the spectrum shows two features the knee at $10^{15.6}$ eV [8] and the second knee at $10^{17.5}$ eV [8], where the spectrum becomes steeper. It is assumed that between 10^{17} eV and 10^{18} eV the source of the cosmic rays changes with increasing energy from galactic to extra galactic [8]. To be able to find this transition with the Pierre Auger Observatory, it is necessary to extend the observable energy range to lower energies. One of those extensions is the system of *High Elevation Auger Telescopes* (HEAT). It extends the field of view of the fluorescence detector by 30°

in elevation. This enables the detector to see higher-evolving and therefore lower energetic showers.

The fluorescence detector provides the ability to determine the longitudinal shower development and therefore the energy deposit at certain depths. By this measurement it is possible to determine the chemical composition of the cosmic rays on a statistical basis.

This work is based on data taken with the HEAT extension of the Pierre Auger Observatory, and contributes to the understanding of the mass composition in the range of primary energies from $10^{17.0}$ to $10^{18.5}$ eV. This is done by presenting an analysis of the depth of the shower maximum including the treatment of uncertainties with Monte Carlo simulations. At the beginning there is a check of the monitoring data (cf. sec. 4.4), which are used as an input for the Monte Carlo (cf. chap. 5), to get a most realistic simulation.

After showing the results of the Monte Carlo in chapter 5 a correction for the detector resolution is taken into account for the data analysis in chapter 6. Finally, the corrected mean depth of the shower maximum over the primaries' energies and the RMS of the shower maximum over the primaries' energies are presented and compared with the predictions of different hadronic interaction models in chapter 7.

2. Cosmic Rays

In the early 20th century during several balloon flights V. Hess measured [1] an increase of ionizing radiation with altitude. He concluded, that the origin of the radiation was from above the atmosphere. This radiation was later named cosmic rays by Robert Andrews Millikan. Some years later in 1929, W. Bothe and W. Kohlhörster used Geiger-Müller counters to measure coincident signals of cosmic rays [9]. They characterized them as charged particles by placing different absorbers between the detectors.

In 1939 Pierre Auger et al. used Geiger-Müller counters to measure coincident signals with detector spacings up to 300 m [5]. This complies with primary particles with a kinetic energy of up to 10^{16} eV hitting the atmosphere and producing secondary particles. Today's direct measurements of up to 10^{15} eV show a hadronic dominated chemical composition of the primaries [10] (cf. fig. 2.1).

2.1. Energy Spectrum

The energy spectrum of cosmic rays can be described by a power law $\frac{\mathrm{d}N}{\mathrm{d}E} \propto E^{\gamma}$ with the spectral index γ. For energies below $5 \cdot 10^{15}$ eV it is $\gamma \approx -2.7$, at higher energies the spectrum steepens to $\gamma = -3.1$. This point in the energy spectrum is called the *knee*, with a particle flux of $1\,\mathrm{m}^{-2}\,\mathrm{year}^{-1}$ at this energy. Another steepening called the *second knee* occurs at $4 \cdot 10^{17}$ eV. At the ankle at $4 \cdot 10^{18}$ eV it flattens again to $\gamma = -2.7$ and the flux decreases to $1\,\mathrm{km}^{-2}\,\mathrm{year}^{-1}$ at this point.

It is expected that at energies above $6 \cdot 10^{19}$ eV the *Greisen-Zatsepin-Kuzmin* (GZK) effect sets in [21, 22]. The GZK effect is the interaction of high energetic protons with the cosmic-microwave-background (CMB) and leads to an energy loss of the protons and to the production of pions.

$$p + \gamma_{\mathrm{CMB}} \rightarrow \Delta \rightarrow p' + \pi \tag{2.1}$$

The expected flux suppression from the GZK cut-off above $6 \cdot 10^{19}$ eV has been measured by the Pierre Auger Observatory [23] and the HiRes experiment [24].

Because of the low flux at higher energies, a direct measurement of cosmic rays is limited by detector size to energies of below 10^{15} eV. At higher energies indirect measurement methods are applied, which sample the secondary particles at ground level or their traces through the atmosphere. Fig. 2.2 shows the cosmic energy spectrum from several experiments.

The knee, second knee and ankle are often interpreted as a change of the acceleration method and/or changes in the chemical composition of the cosmic rays [8]. A common interpretation is that the knee is the maximal energy achievable for protons in our galaxy. For heavier elements with charge number Z this cut-off is expected at $E_{C,Z} = Z \cdot E_{C,p}$, with $E_{C,p}$ the cut-off energy of protons [25].

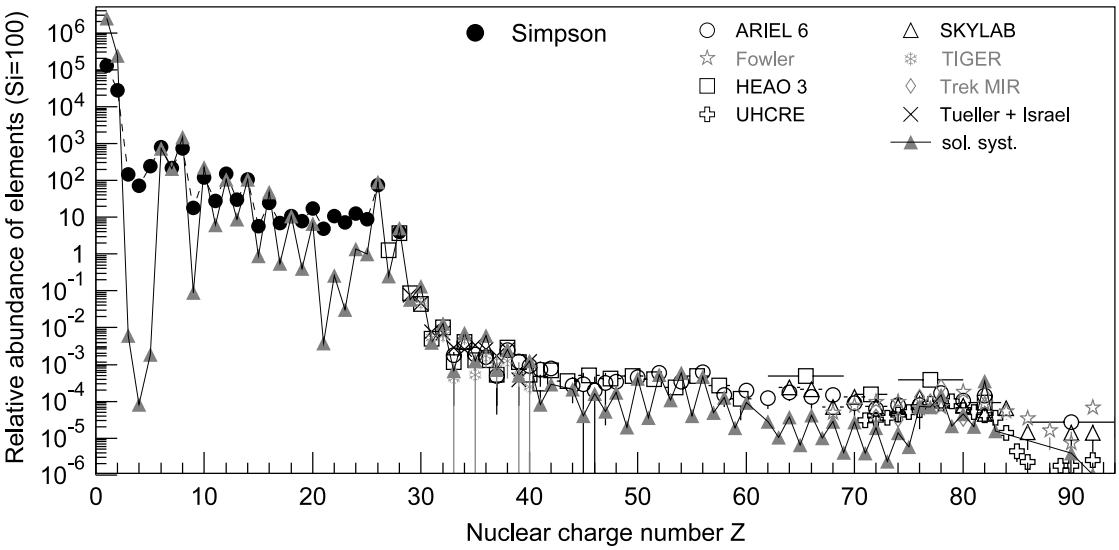

Figure 2.1.: Abundance of elements with an energy of about 1 GeV/nucleon in cosmic rays (taken from [8]). Measurements of primaries with atomic charge numbers below 28 $Z \leq 28$ taken from [11]. Data for heavy nuclei taken from ARIEL 6 [12, 13], HEAO3 [14], SKYLAB [15], TIGER [16], TREK/MIR [17, 18] and UHCRE [19]. The abundance of elements in the solar system according to [20] is also shown.

2.2. Sources of Cosmic Rays

The sources of high energetic cosmic rays are still subject of ongoing research. A common theory for accelerating particles to high energies is the *shock acceleration* [26] by supernovae remnants.

The shock front of a supernovae explosion propagates with the velocity β_s (in units of speed of light), which is higher than the sonic speed in the medium. The shock front is not a substantial entity but is the border between two magnetic domains. A relativistic particle, diffusely scattered in the rest frame of the medium, can stochastically cross the shock front. At each crossing the particle gains the energy

$$\Delta E \propto \beta_s \quad . \tag{2.2}$$

In the frame of this model a spectral index $\gamma = 2 + \varepsilon(\beta_s)$ is predicted.

Besides the mentioned β_s, the maximum achievable energy is also limited by the size of the source and the strength of its magnetic field, because with increasing energy of the accelerated particle its Larmor radius

$$r = 1.08\,\mathrm{pc} \cdot \frac{E/\mathrm{PeV}}{Z \cdot B/\mu\mathrm{G}} \tag{2.3}$$

also increases. If the Larmor radius is greater than the size of the source, the particle exits the acceleration process. Therefore, the maximum reachable energy [8] of the diffuse shock acceleration can be estimated as

$$E_{\max} \approx 10^{18}\,\mathrm{eV} \cdot Z \cdot \beta_s \left(\frac{R}{\mathrm{kpc}}\right) \left(\frac{B}{\mu G}\right) \tag{2.4}$$

for a particle with charge Z, size of the source R and the magnetic field strength B at the source. Possible sources are shown in fig. 2.3.

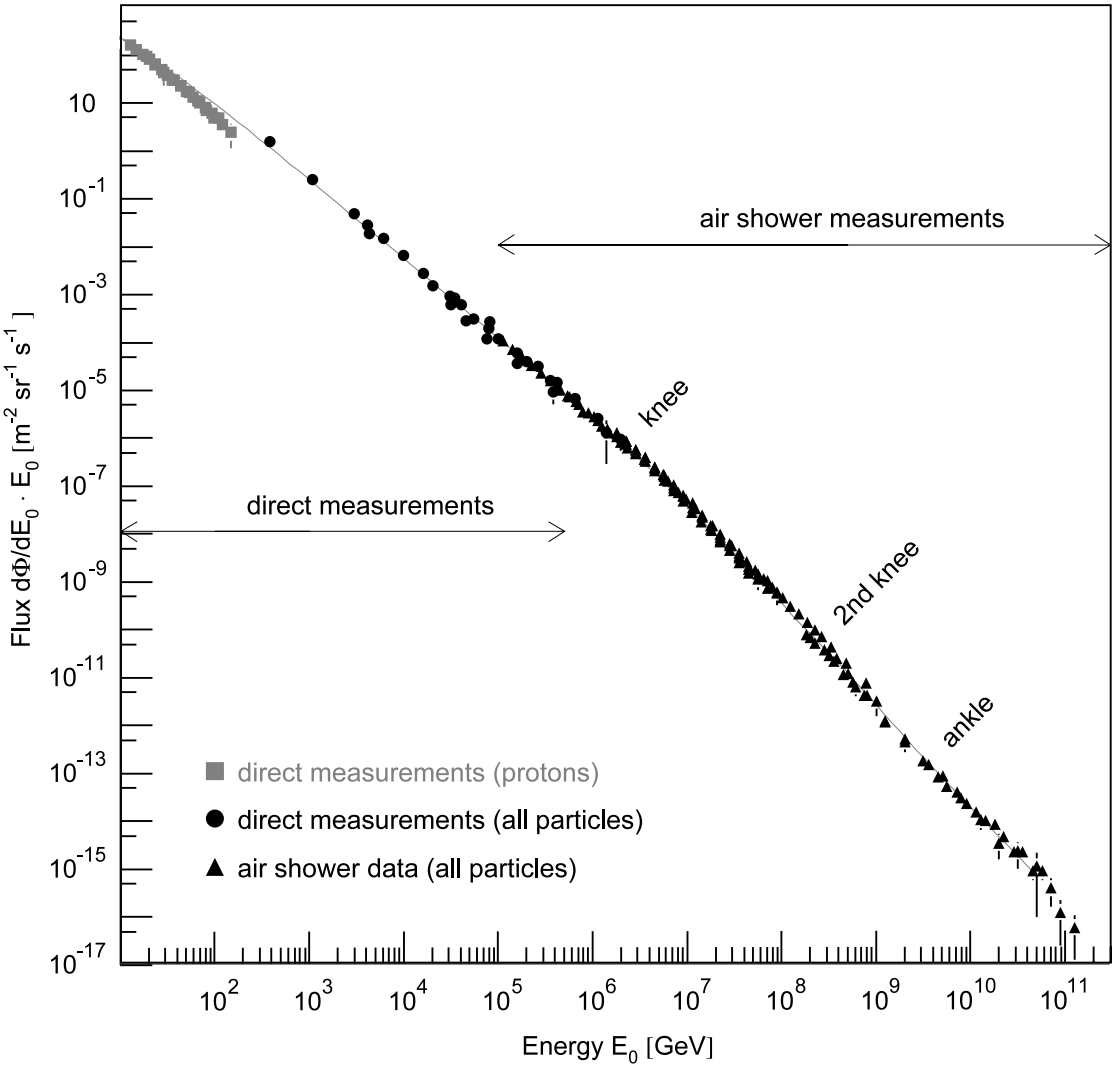

Figure 2.2.: Particle flux spectrum over energy from 10^{10} eV to 10^{20} eV, combining direct and indirect measurements. Taken from [8].

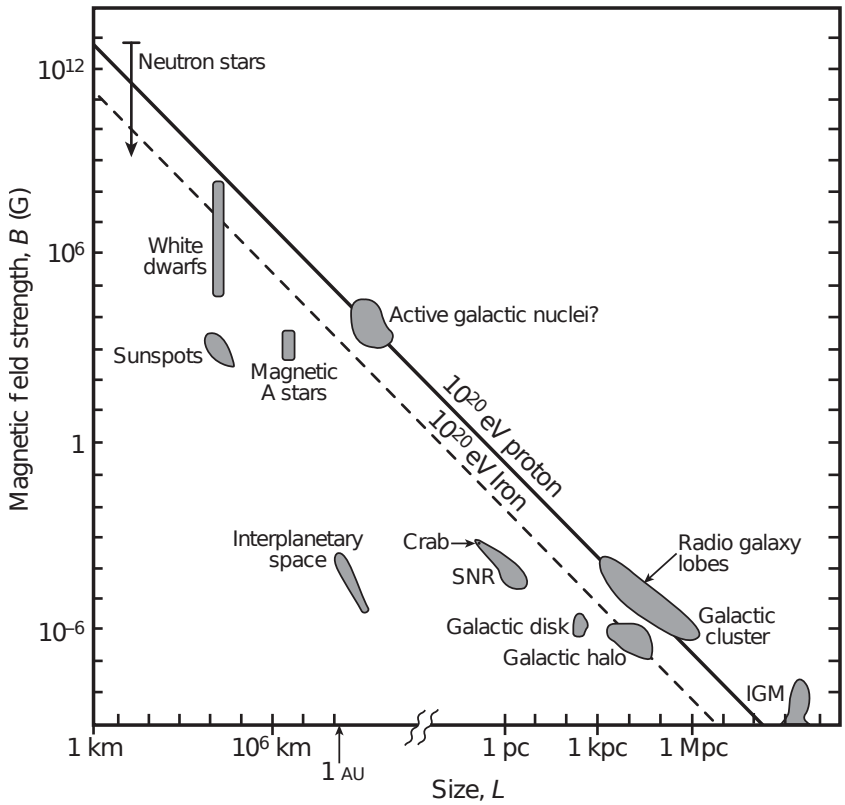

Figure 2.3.: Hillas plot of the magnetic field strength as a function of the size of astrophysical accelerator candidates [30]. The solid (dashed) diagonal line indicates possible combinations of magnetic field strengths and sizes of a source, which will allow the source to accelerate proton (iron) primaries to an energy of 10^{20} eV. Possible source candidates are displayed.

Another type of models that are able to explain the highest energy particles are the *Top-Down*-models. It is assumed, that highly energetic particles are created at the decay of currently unknown very heavy primary particles [27, 28] or topological defects [29].

2.3. Extensive Air Showers

High energy cosmic rays reaching earth interact with molecules in the atmosphere. This leads to multiple new secondary particles. These secondary particles again interact with the molecules in the atmosphere and start cascades of new reactions. This is called an extensive air shower (EAS). A shower consists of a hadronic, electromagnetic, muonic and neutrino component.

The processes involved are described by cross-sections depending on the traversed matter. Hence it is reasonable to introduce the concept of atmospheric depth. The atmospheric depth is defined by the path integral

$$X(s) = \int_s \rho(x)\,\mathrm{d}x \tag{2.5}$$

along the travelled track s, with the atmospheric density ρ at point x. X has the unit of $\mathrm{g\,cm^{-2}}$. An atmospheric depth of $0\,\mathrm{g\,cm^{-2}}$ means the top of the atmosphere and $\sim 1000\,\mathrm{g\,cm^{-2}}$ means close to the ground.

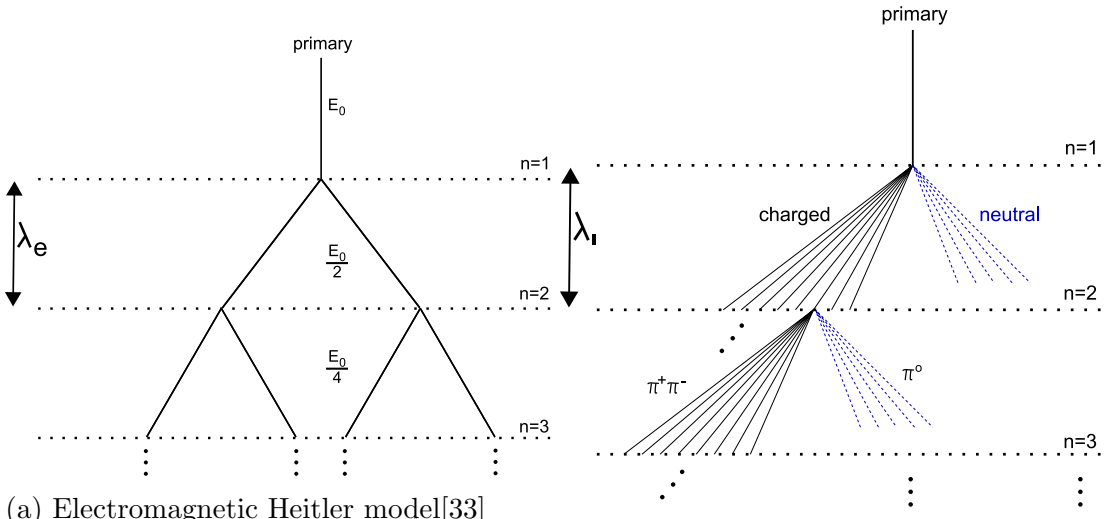

(a) Electromagnetic Heitler model[33]

(b) Hadronic Heitler-Matthews model[33]

Figure 2.4.: Development of electromagnetic (2.4a) and hadronic extensive air showers (2.4b).

2.3.1. Electromagnetic Component

A simple interaction model for electromagnetic cascades is the Heitler-Model [31]. It assumes that after a radiation length λ_e an electron or positron emits a photon, or that a photon produces an electron-positron pair (cf. fig. 2.4a). Therefore, each λ_e the particle number in the EAS doubles. Hence the EAS consists of $N = 2^{X/\lambda_e}$ electromagnetic particles after travelling through the atmospheric depth X.

For the electrons and positrons the relevant process at high energies like in an EAS is the emission of a *Bremsstrahlung's* photon. The dominant process for the photons is *pair production* of an electron-positron pair. If the energy of the secondary particles is below the critical energy $E_C \approx 85\,\mathrm{MeV}$ (in air), the production of new particles stops and the energy loss due to ionisation becomes dominant. Therefore, the maximum particle count is reached when the energy drops below E_C and is calculated by $N_{max} = E_0/E_C$. Therefore, the atmospheric depth of the shower maximum X_{max} depends on the energy

$$X_{\mathrm{max,em}} = \lambda_e \cdot \log_2\left(\frac{E_0}{E_C}\right) \propto \log E_0 \quad . \tag{2.6}$$

2.3.2. Hadronic Component

To describe proton induced EAS the Heitler model can be extended to the Heitler-Matthews model[32]. It assumes, that a proton hitting a molecule in the atmosphere produces multiple pions. About one-third of the pions are neutral π^0. These decay to photons, which initiate electromagnetic showers. On the other hand, charged pions travel a certain distance λ_I (interaction length) until they hit another molecule, and the next generations start (cf. fig. 2.4b). At each step in the hadronic part of the EAS one-third of the energy is transferred to neutral pions, which starts new electromagnetic cascades. Therefore, the observable fluorescence light (sec. 3.2.1) mainly emitted by the electromagnetic component is the superposition of several electromagnetic sub-showers.

As for the electromagnetic shower the hadronic cascade stops if the energy of individual charged pions drops below a critical energy. The critical energy is

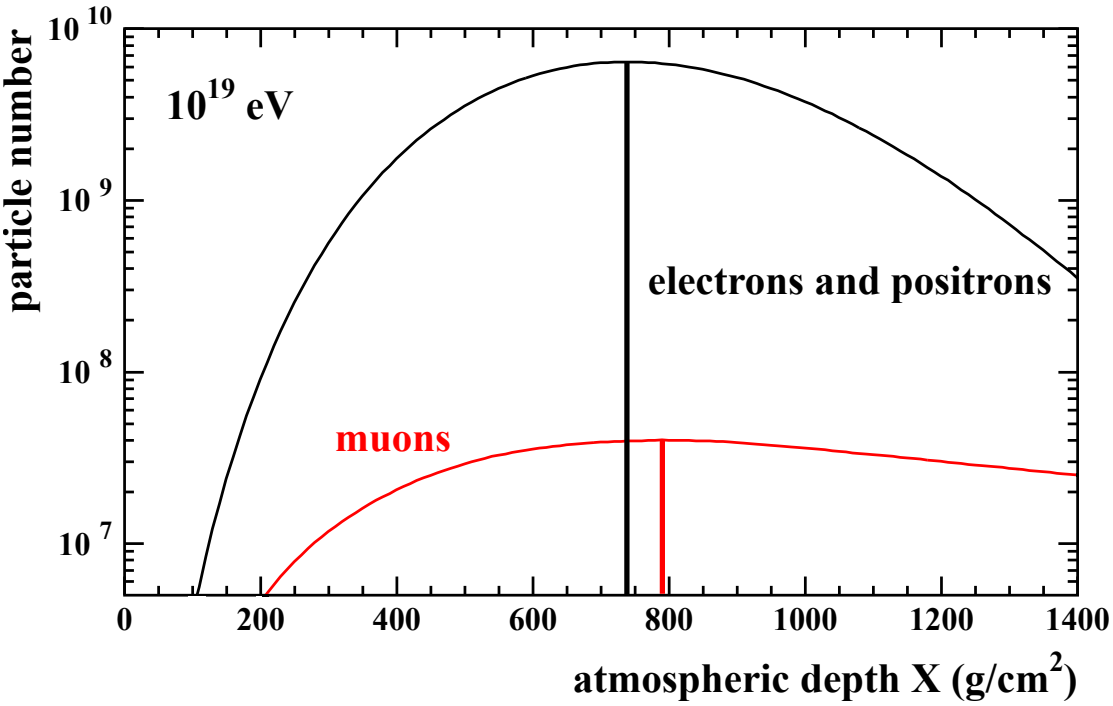

Figure 2.5.: Longitudinal profile of a typical proton induced EAS with a primary energy of 10^{19} eV subdivided into muons, electrons and protons. Marked are the maximum particle number of each component. Plot modified from [34].

reached if the pions decay before travelling another λ_I. These $\pi^{\pm}$ decay to muon-neutrino pairs. The aforementioned superposition of the electromagnetic shower component and the hadronic shower component reach their maximum particle number at different atmospheric depths (fig. 2.5).

As with the electromagnetic shower, the depth of the shower maximum of the hadronic component is proportional to the logarithm of the primary energy

$$X_{\mathrm{max,p}} = \alpha + \lambda_{\mathrm{e}} \cdot \ln(10) \cdot \log E_0 \tag{2.7}$$

where α holds the details of the first interaction and λ_{e} is the electromagnetic radiation length. This is just an approximation that only considers the first hadronic interaction. Compared to detailed simulations the resulting values of $X_{\mathrm{max,p}}$ are about $100\,\mathrm{g\,cm^{-2}}$ too low.

The processes in an EAS are subject to statistical fluctuations even for identical primaries entering the atmosphere [32]. The fluctuations can be traced back to statistical fluctuations in the first few interactions. These shower-to-shower fluctuations influence the depth of the hadronic and electromagnetic shower maximum. Consequently, only statistical statements about the value of X_{max} can be made. Therefore, the average X_{max} per energy interval and its root mean square (RMS) are used as observables for an analysis of the chemical composition of cosmic rays (cf. fig. 2.6).

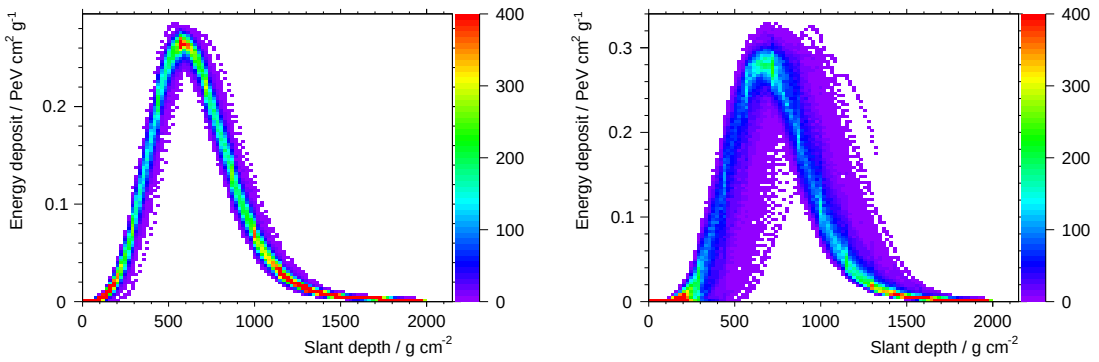

(a) Iron (b) Proton

Figure 2.6.: Energy deposit per atmospheric depth of 1000 showers from CONEX [36] simulations with EPOS [37] at $10^{17.25}$ eV.

EAS induced by heavier primaries with atomic mass number A and energy E_0 can be approximated by the superposition of A proton induced showers each carrying the energy E_0/A. This reduces the penetration depth of the shower (cf. fig. 2.7). Therefore, the $X_{\max}$ is sensitive to the mass of the primary

$$X_{\max,\mathrm{A}} = \alpha + \lambda' \left(\log E_0 - \log A\right) \quad . \tag{2.8}$$

According to [35] the shower-to-shower fluctuations also decrease with increasing atomic mass (cf. fig. 2.6). A first approximation is $\mathrm{RMS}(X_{\max}) \propto 1/\sqrt{A}$.

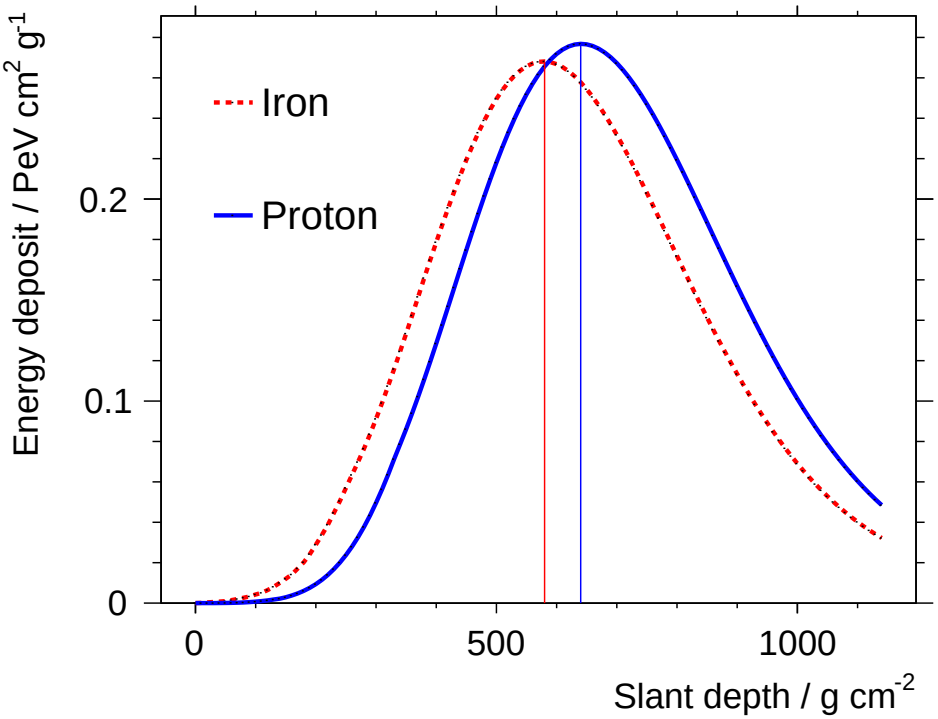

Figure 2.7.: Comparison of the energy deposit per slant depth for a typical iron (red, dashed line) and a typical proton (blue, solid line) induced shower from CONEX [36] simulations with EPOS [37] at $10^{17.25}$ eV.

3. The Pierre Auger Observatory

The Pierre Auger Observatory [38] in the Argentinean province of Mendoza is the world's largest cosmic ray observatory. It is located at an altitude of 1400 m a.s.l.. It was designed to measure the energy spectrum, the mass composition and the anisotropy of ultra-high-energy cosmic rays from 10^{18} eV to the highest observable energies. Due to the low flux of cosmic rays at these energies the detector covers an area of 3000 km^2. It features a hybrid detector design consisting of two complementary detection techniques: a surface detector and a fluorescence light detector.

The surface detector (SD) consists of 1600 water Cherenkov detector stations with a spacing of 1500 m and provides an uptime of nearly 100 %[39]. These stations are overseen by four fluorescence detector (FD) sites called eyes (cf. fig. 3.1). These eyes comprise six telescopes each. Since the FD can only operate on clear, moonless nights, its uptime is limited to about 13 % [40].

3.1. Surface Detector

The surface detector consists of single water Cherenkov detector stations (cf. fig. 3.2a). The single stations and their communication system are documented at [39]. Each station is filled with 12 m^3 of pure water. The Cherenkov light of traversing particles (mostly muons) is detected by three PMTs[1]. The stations are equipped with a small readout computer which communicates via a wireless network link with the central data acquisition system (CDAS). The wireless link supports a data rate of 1200 bits s^{-1} per station. The time synchronisation of each station is performed by a GPS receiver. Each detector is powered by two battery-buffered solar panels.

Each station autonomously records the local cosmic ray flux. Once a shower candidate is registered, the signals from the PMTs are digitized by a FADC[2] and are stored locally for 10 s. If this so called T1 trigger meets other criteria (cf. [43]) as well, a T2 trigger is sent to CDAS. If T2 triggers of multiple stations are spatially and temporally correlated, CDAS sends a T3 trigger to the SD array. The T3 trigger requests the FADC traces of all stations with a T1 or T2 trigger (if within 30 μs of T3).

3.2. Fluorescence Detector

The fluorescence detector of the Pierre Auger Observatory consists of 24 telescopes. They are organized in four sites (eyes), each consisting of six telescopes. Each telescope has a field of view (FOV) of $30° \times 30°$ in azimuth and elevation. With six telescopes per FD eye, a coverage of 180° in azimuth is achieved and a 100 % FD trigger efficiency for showers with energies above 10^{19} eV over the array is

[1] **P**hoto **M**ultiplier **T**ube
[2] **F**lash **A**nalog to **D**igital **C**onverter

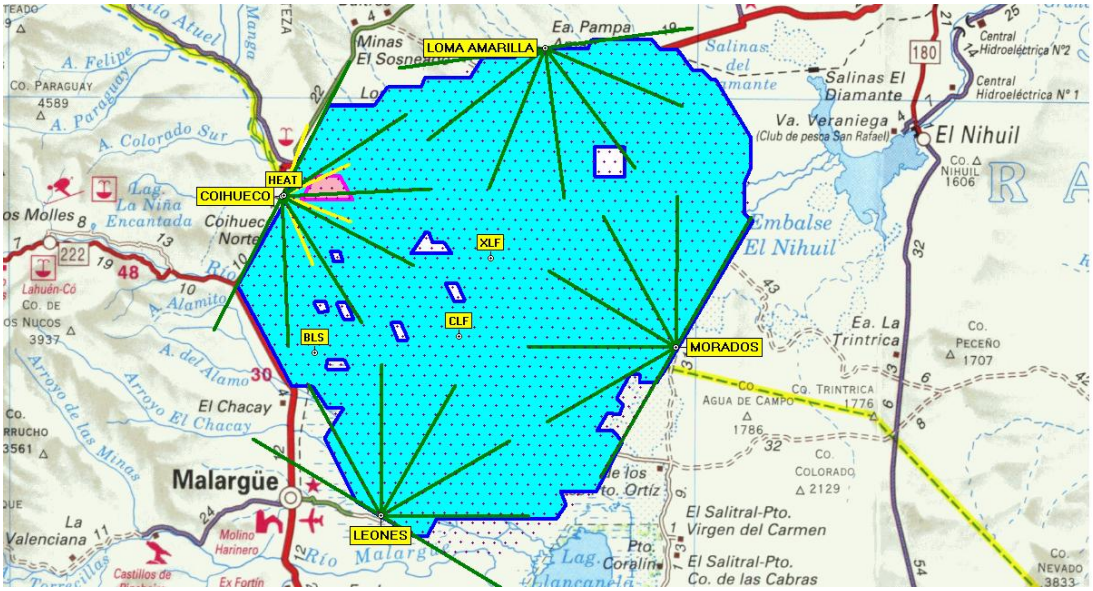

Figure 3.1.: The Pierre Auger Observatory in Argentina [41]. The blue dots mark the ideal SD positions. At the border of the SD array the four conventional FD and the HEAT eyes including the azimuthal field of view are marked. Besides the detectors also the atmospheric monitoring stations BLS (balloon launching station), CLF (central laser facility) and XLF (extreme laser facility) are plotted. Close to HEAT and Coihueco, the SD infill array with closer spacing between the stations is marked in red.

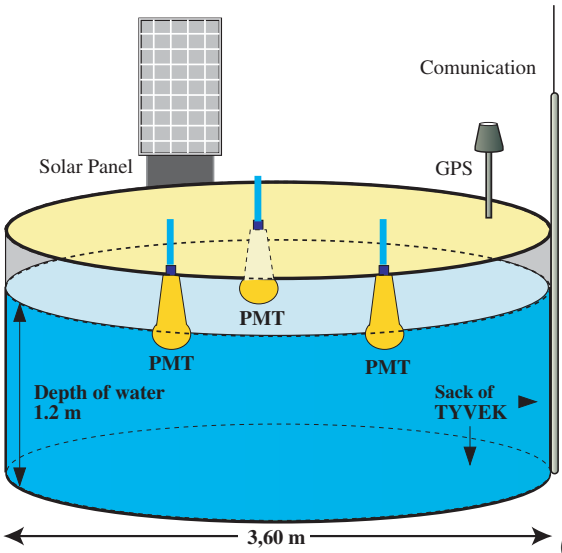

(a) Schematics of a surface detector station.

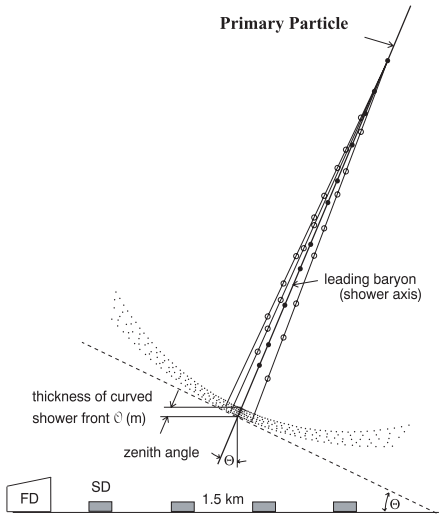

(b) Schematics of a shower relative to the Auger detectors.

Figure 3.2.: Both Drawings are take from [42].

assured. The telescopes observe the fluorescence light from evolving showers. The telescope's design is described in detail in [40].

3.2.1. Fluorescence Light Production

The fluorescence light observed by the telescopes is produced by charged secondary particles (mostly $e^{\pm}$) from EAS, which deposit energy in the atmosphere by ionization or excitation of molecules. The excited molecules isotropically emit fluorescence[3] light, while relaxing to their ground state. Therefore, a shower can be observed from all sides. The number of emitted photons $\mathrm{d}N_{\gamma,0}$ per atmospheric depth $\mathrm{d}X$ can be expressed by (cf. [44])

$$\frac{\mathrm{d}N_{\gamma,0}}{\mathrm{d}X} = \int\int Y(\lambda, P, T, u, E) \cdot \frac{\mathrm{d}N_{\mathrm{e}}(X)}{\mathrm{d}E} \frac{\mathrm{d}E_{\mathrm{dep}}}{\mathrm{d}X} \,\mathrm{d}E \,\mathrm{d}\lambda \tag{3.1}$$

with the $e^{\pm}$ energy spectrum $\mathrm{d}N_{\mathrm{e}}(X)/\mathrm{d}E$, the deposited energy $\mathrm{d}E_{\mathrm{dep}}/\mathrm{d}X$ per atmospheric depth and the fluorescence yield Y. The fluorescence yield describes the number of emitted photons per deposited energy E and depends on the wavelength λ of the fluorescence light, the atmospheric pressure P, the temperature T and the humidity u.

The number of fluorescence light photons $\mathrm{d}N_{\gamma}$ per atmospheric depth $\mathrm{d}X$ measured at the detector is described by (cf. [44])

$$\frac{\mathrm{d}N_{\gamma}}{\mathrm{d}X} = \frac{\mathrm{d}E_{\mathrm{dep,tot}}}{\mathrm{d}X} \int Y'(\lambda, P, T, u) \cdot \tau_{\mathrm{atm}}(\lambda, X) \cdot \varepsilon(\lambda, r) \,\mathrm{d}\lambda \tag{3.2}$$

with the total energy deposit per atmospheric depth $\mathrm{d}E_{\mathrm{dep,tot}}/\mathrm{d}X$, the energy independent fluorescence light yield Y', the transmission of the atmosphere τ_{atm} and the wavelength and distance r depending detection efficiency ε of the detector. Hence, the number of emitted and observed photons is proportional to the energy deposited by the charged particles, the longitudinal shower profile $\mathrm{d}E/\mathrm{d}X$ is measured.

However, other kinds of light like Cherenkov light and scattered light contribute to the measured light flux as well. To account only for the fluorescence light in the energy reconstruction, the measured light flux has to be split up into its components during reconstruction. Another inconvenience arises from secondary shower particles, which are *invisible* to the detector like neutrinos or muons. As a consequence a part of the shower energy is not observable with the direct calorimetric measurement. Both effects have to be considered in the shower reconstruction (cf. 3.3).

3.2.2. Hardware

The individual telescopes (cf. fig. 3.4) are placed in a clean and air-conditioned room. The ultra-violet fluorescence light enters the telescope room through an UV-passing filter[4] and corrector ring. The light is focused by a mirror onto a camera, which consists of 440 pixels each covering a field of view of 1.5° (cf. [40]). In front of the optics a shutter is placed, which avoids damage to the telescope at daylight or other occurrences of a too high light flux.

[3] UV light between 300 and 430 nm.

[4] Without the UV-passing filter, the camera would be saturated by visible light.

The camera is organized in 20 columns and 22 rows, consisting of hexagonal PMTs with light collectors to reduce the dead space between the pixels. The pixels are organized in ten groups of 44 pixels. The PMTs in each group have the same gain characteristics and are powered by one high voltage (HV) channel.

The pixels are directly connected to the front end electronics, which adapts the analog PMT pulses for digitization by analog-to-digital converters (ADCs). After digitization, the signals are fed into the trigger system. Each triggered event gets a timestamp. The fluorescence detector uses GPS for time synchronisation.

Each telescope has a control computer called MirrorPC, which controls the readout of triggered events. The MirrorPCs feed the recorded data further to a computer controlling the eye called the EyePC, which finally builds the event from the telescope data. The EyePC communicates also with the CDAS.

3.2.3. Trigger

The signal of each pixel is continuously digitized with an FADC at 10 MHz and temporarily stored. If the integrated ADC signal in a pixel is over threshold, a first level trigger (FLT) is generated. The threshold is dynamically adjusted to keep a FLT rate of 100 Hz (cf. [40]).

The pixel triggers generated by the FLT are read out by the second level trigger (SLT). The SLT tries to match the triggered pixels with straight tracks consisting of five pixels. To increase the fault-tolerance against pixels not hit in the centre (and therefore collecting too less light) and broken PMTs, only four triggered pixels out of five are required for a SLT. If a straight track is matched, the SLT is generated and the FADC traces are stored in a buffer for readout by the MirrorPC.

On events accepted by the SLT, a third trigger (TLT) is applied. The TLT is optimised for a fast removal of noise events, such as caused by lightning or muon impacts on the camera. Passing events are sent to the EyePC. Besides building the final event data structure from all coincident telescopes in its eye, the EyePC performs a preliminary geometry reconstruction. Including the results, a T3 trigger is sent to CDAS, which performs a readout of signals from SD stations recorded temporally and spatially close to the impact. Merging of SD and FD data for analysis is performed offline.

3.3. Hybrid Data Reconstruction

The reconstruction of events using information from SD and FD is called hybrid reconstruction. The hybrid reconstruction is performed with the Auger $\overline{\text{Off}}\underline{\text{line}}$ software package[45]. $\overline{\text{Off}}\underline{\text{line}}$ is an extensible framework written in `C++`. Besides for event reconstruction it is used for detector simulation.

The versatility of $\overline{\text{Off}}\underline{\text{line}}$ is achieved by several modules. All jobs like event reading, the steps in physical event reconstruction and detector simulation are performed by modules. The used chain of modules can be controlled by XML[46] steering cards. Besides the module sequence also the configuration of single modules can be configured by steering cards.

The hybrid data reconstruction is based on the fluorescence light recorded from FD. The FD ADC traces are converted to photon traces by applying a baseline correction and the corresponding calibration constant. From the temporal sequence of triggered pixels, the light track is determined. Based on this track, the shower

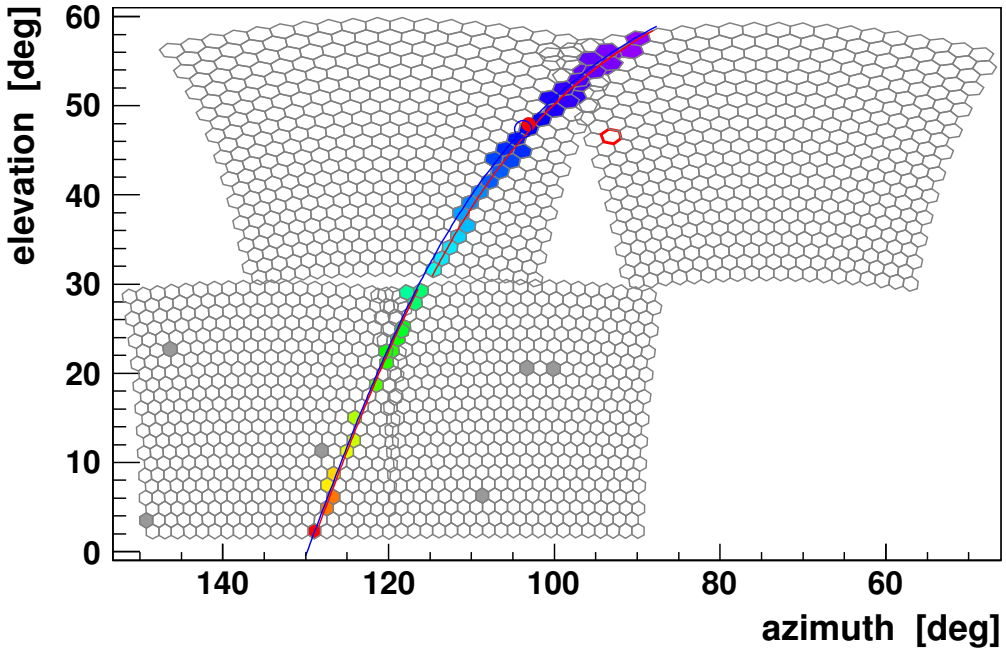

Figure 3.3.: Reconstructed shower detector plane of a simulated 10^{17} eV event.

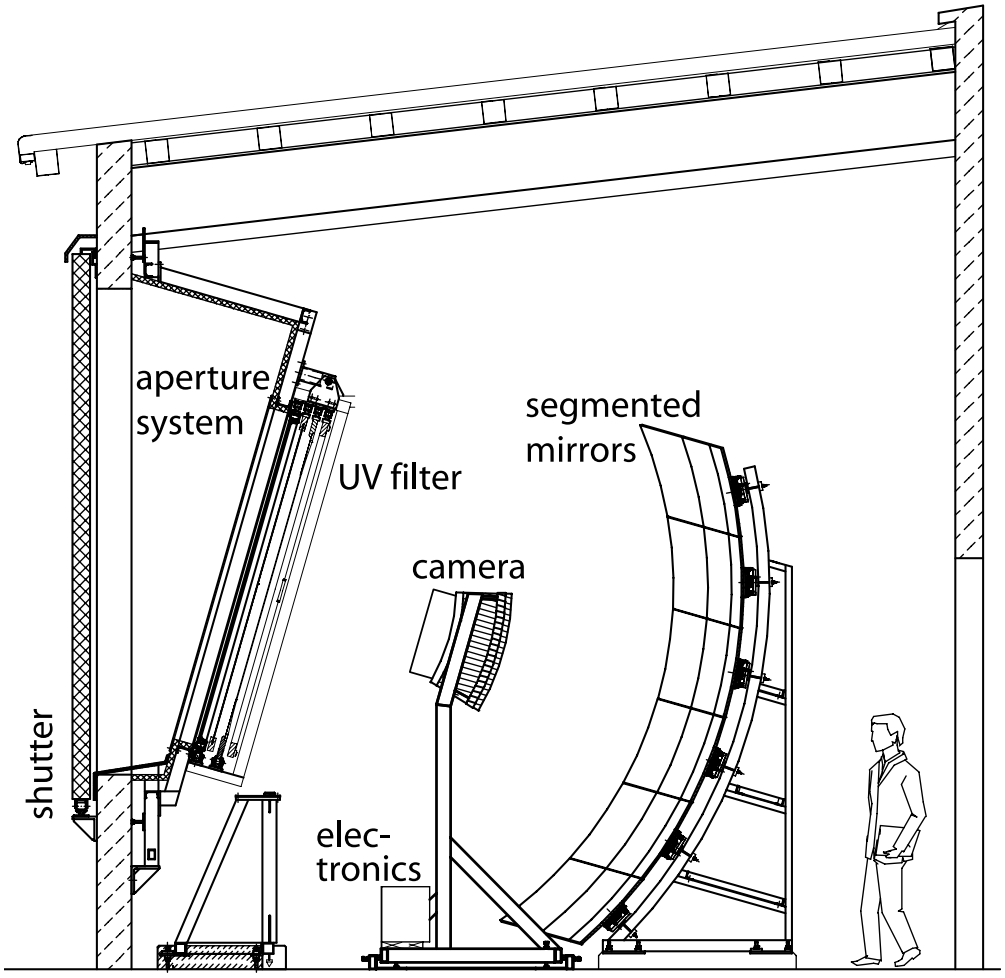

Figure 3.4.: Schematics of one Auger fluorescence telescope [40].

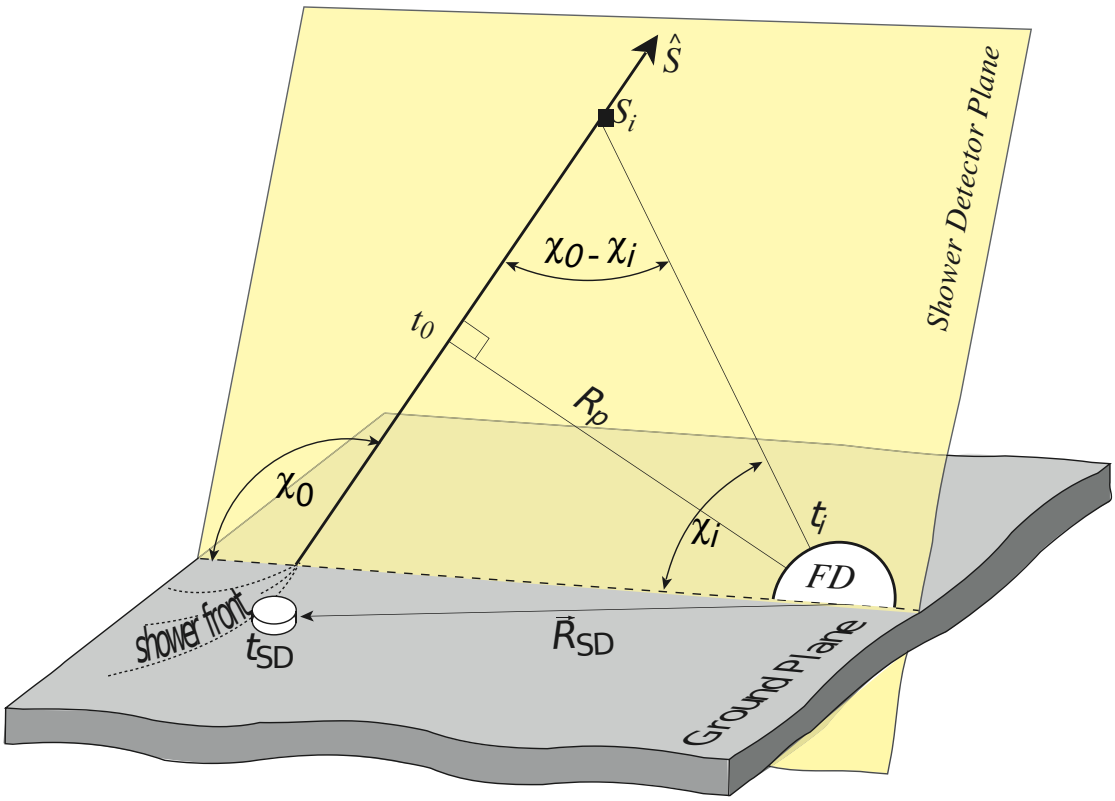

Figure 3.5.: Illustration of properties in geometry reconstruction [47].

detector plane (SDP), which contains the centre of the detector site and the shower axis, is determined (cf. [48]).

According to [49], the SDP vector $\vec{n}_{\mathrm{SDP}}$ is determined by minimizing the angular distance between the SDP vector and the pointing direction $\vec{v_i}$ of each pixel

$$S^2_{\mathrm{SDP}} = \sum_{i=0} \frac{\left(\frac{\pi}{2} - \arccos\left(\vec{n}_{\mathrm{SDP}} \cdot v_i\right)\right)^2}{\sigma_i^2} \tag{3.3}$$

weighted with $\sigma_i = 1/q_i$ and q_i the charge in the i-th pixel.

The orientation of the shower axis $\hat{S}$ in the SDP is described by the angle χ_0 relative to the detector's horizontal plane (cf. fig. 3.5). The angle is determined from the pixel timings[47] and the timing of the hottest SD station in the event. Besides χ_0, the closest distance R_p between detector and shower axis and the time t_0, at which the shower reaches R_p, are determined from a χ^2 minimization process. The χ^2 is defined as

$$\chi^2_{\text{Shower Axis}} = \sum_i \frac{(t_i - t_i^{\mathrm{exp}})^2}{(t_i^{\mathrm{err}})^2} + \frac{(t_{\mathrm{SD}} - t_{\mathrm{SD}}^{\mathrm{exp}})^2}{(t_{\mathrm{SD}}^{\mathrm{err}})^2} \tag{3.4}$$

with the measured light arrival time t_i from the shower point S_i at the i-th pixel, its uncertainty t_i^{err} and its expected arrival time t_i^{exp}. In addition, the trigger time of the hottest SD station in the event t_{SD}, its uncertainty $t_{\mathrm{SD}}^{\mathrm{err}}$ and expectation $t_{\mathrm{SD}}^{\mathrm{exp}}$ are used.

The expected arrival time of the photons at the FD pixels and the muons at the SD station can be determined by geometrical considerations. The current implementation for FD is described in [47]. It considers effects from a height-dependent molecular de-excitation time and domains of different refraction in the atmosphere.

After a successful geometry reconstruction, Cherenkov and scattered light contributions are calculated to isolate the fluorescence light contribution. Based on the determined fluorescence light profile, the energy deposit per atmospheric depth $\mathrm{d}E/\mathrm{d}X$ is determined and a four parameter Gaisser-Hillas function [50] is fitted on the deposit profile

$$\frac{\mathrm{d}E}{\mathrm{d}X}(X) = \left.\frac{\mathrm{d}E}{\mathrm{d}X}\right|_{X=X_{\max}} \left(\frac{X - X_0}{X_{\max} - X_0}\right)^{\frac{X_{\max}-X_0}{\lambda}} e^{\frac{X_{\max}-X}{\lambda}} \tag{3.5}$$

with the mean free path λ, the depth of first interaction X_0, depth of maximum energy deposit $X_{\max}$, and the maximum energy deposit per atmospheric depth $\mathrm{d}E/\mathrm{d}X(X = X_{\max})$.

The integral over the longitudinal shower profile is the calorimetric energy E_{cal}. The calorimetric energy is approximately 90 % of the primaries' energy E_0, because the energy carried away by neutrinos and muons is not visible in the FD (cf. [51, 52]). To determine the effect of invisible energy on the reconstructed primary energy, shower and detector simulations are used, which lead to a dependency on hadronic interaction models. The correction described in [53] is applied to Auger FD events during reconstruction.

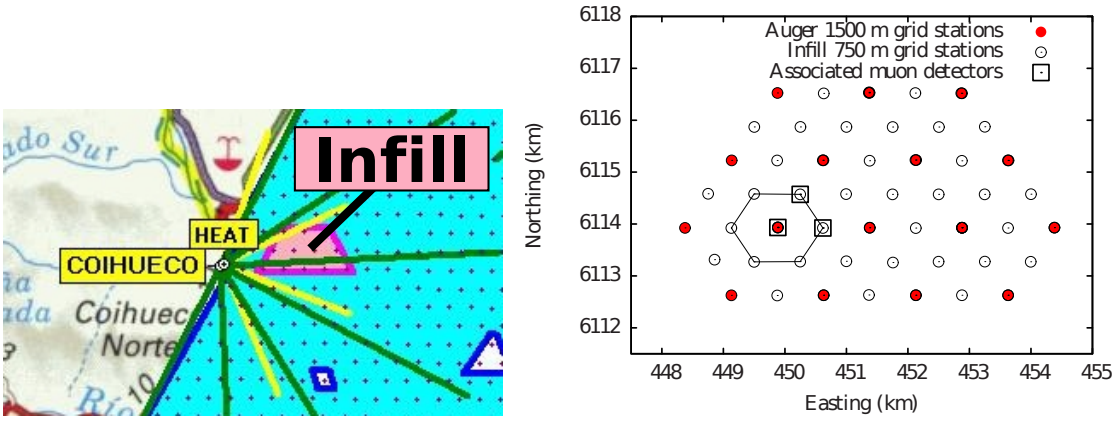

(a) Position of AMIGA in the SD array (modified from [41]).

(b) Detailed view on AMIGA (taken from [54])

Figure 3.6.: *Auger Muons and Infill for the Ground Array* (AMIGA).

3.4. Enhancements

In addition to the already existing detectors, three enhancements to the Pierre Auger Observatory are deployed. A part of these extensions are the *High Elevation Auger Telescopes* (HEAT). They extend the energy range of the regular FD to energies between 10^{17} eV and $10^{18.5}$ eV. HEAT is presented in more detail in chapter 4, the focus in this section lies on the other two enhancements.

The *Auger Muons and Infill for the Ground Array* (AMIGA) is the SD complement to HEAT, because it aims to extend the SD energy range down to 10^{17} eV [54]. AMIGA is located close to HEAT (cf. fig. 3.6a). It consists of a 23.5 km^2 infill area in the surface detector array, which reduces the spacing between SD stations to 750 m (cf. fig. 3.6b). In a smaller subset of this area of 5.9 km^2, a further reduction of the spacing between the stations to 433 m is planned. Furthermore, a set of buried muon scintillation detectors at a depth of 2.3 m is planned for each infill station. Currently, two stations are equipped with the buried muon scintillator. Due to the shielding of the scintillation detectors, the electromagnetic component is strongly suppressed compared to the SD stations. Therefore, AMIGA represents a third component in the Auger hybrid detection principle.

A new fourth detection principle for EAS is introduced to Auger with the *Auger Engineering Radio Array* (AERA) [54]. It exploits that EAS produce coherent broadband radio pulses in the VHF band (10..100 MHz). Currently, AERA consists of 21 radio-detection stations. For the final stage of the Auger Radio detector 160 radio stations covering an area of 20 km^2 are planned. As the other enhancements, AERA has an energy threshold of 10^{17} eV. Furthermore, AERA provides a 100 % duty cycle.

In addition, several methods to detect microwave emissions from EAS are explored. If the tests work out successfully, the microwave detection with its near 100 % duty cycle will be the fifth detection principle in the Auger's hybrid system.

4. HEAT

The reconstruction quality of EAS observed by the FD heavily relies on the observation of the depth of the shower maximum $X_{\max}$ (cf. sec. 6.1). The lower the energy and the higher the mass of the EAS inducing primary, the higher the $X_{\max}$ is located in the atmosphere (cf. sec. 2.3).

To extent the energy range of the regular FD below 10^{18} eV down to 10^{17} eV, the *High Elevation Auger Telescopes* (HEAT) were designed and built. It consists of three standard Auger FD telescopes, which are mounted in a tiltable housing, which can be tilted by 30° upwards. The tilting allows to observe showers evolving higher in the atmosphere (cf. fig. 4.1) [54]. This opens the gate for the Pierre Auger Observatory to the interesting energy region, where the transition from primaries of galactic origin to those of extragalactic origin is expected [8].

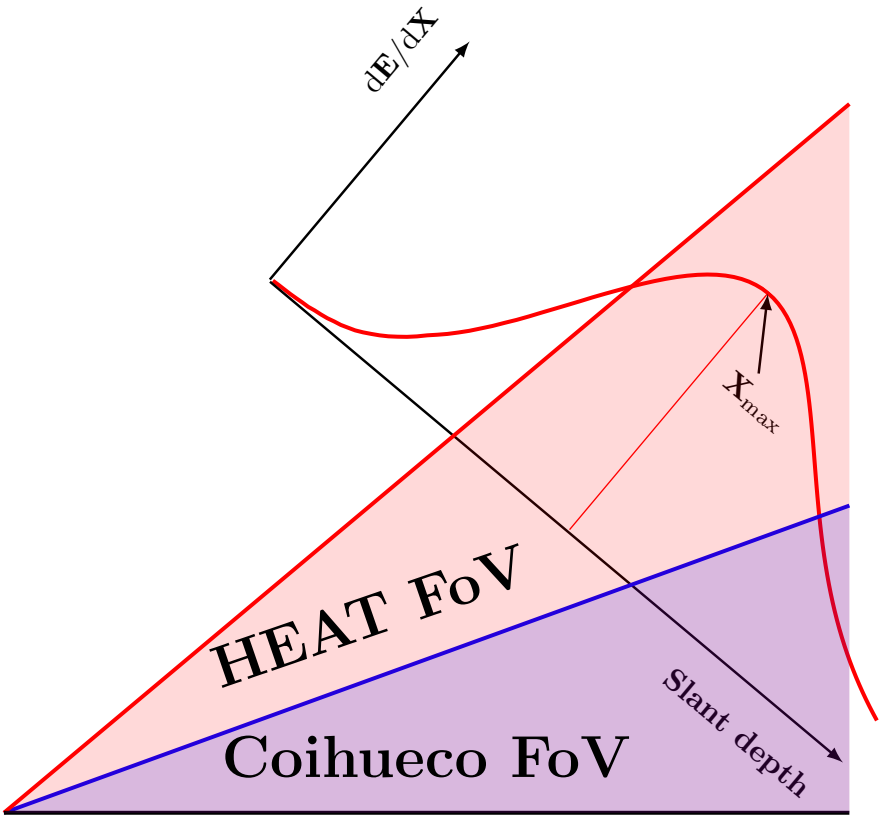

Figure 4.1.: Combined field of view (FoV) of a regular Auger FD telescope (Coihueco) and HEAT. The shown angles are not to scale. Additionally, the longitudinal energy deposit profile of a shower, which is only fully reconstructible in the HEAT extended FoV, is shown.

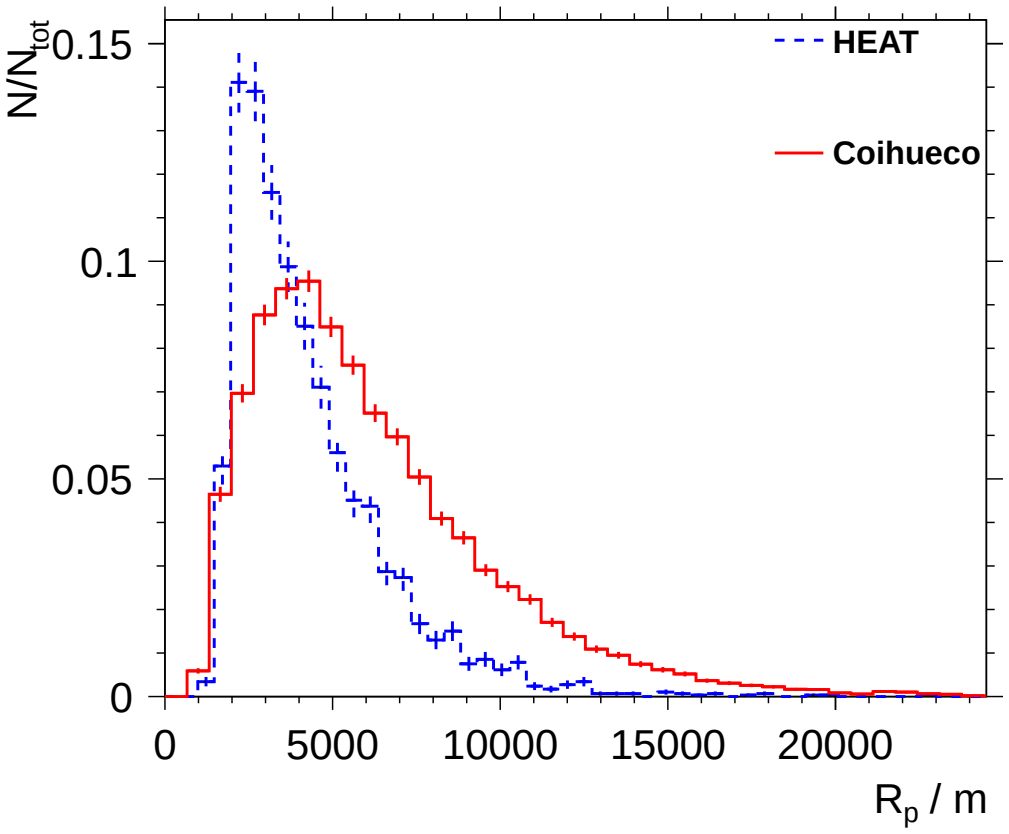

Figure 4.2.: Distribution of the distance R_p between the detector site and the closest point of the shower axis of measured showers for a successful geometry reconstruction. HEAT data is depicted in blue (dashed line). For comparison with standard FD the R_p distribution of Coihueco is shown in red (solid line).

4.1. HEAT Hardware

The HEAT tilting mechanism is a mechanical challenge, because for a good reconstruction of the observed showers it is important to precisely know the pointing[1] of each telescope at every time. To assure that the pointing does not change after an initial calibration, it is necessary to introduce a monitoring of the distances between camera and mirror, mirror and shutter and of the optical axis [55].

As mentioned in sec. 3.2.3, the signal of each PMT of one regular FD telescope is digitized with a FADC at a sampling rate of 10 MHz. The electronics used for HEAT supports a sampling rate of up to 40 MHz. As depicted in fig. 4.2 HEAT observes more close showers than the regular FD. Since close showers have a higher angular velocity, the higher sampling rate supports a better temporal and geometrical resolution. Finally, the HEAT FADCs are operated with a sampling rate of 20 MHz (cf. [54]), which corresponds to a FADC bin size of 50 ns. This causes the first level trigger interval to be reduced to 50 ns, too. The second level trigger is unaffected by these changes.

[1] Optical axis of a telescope.

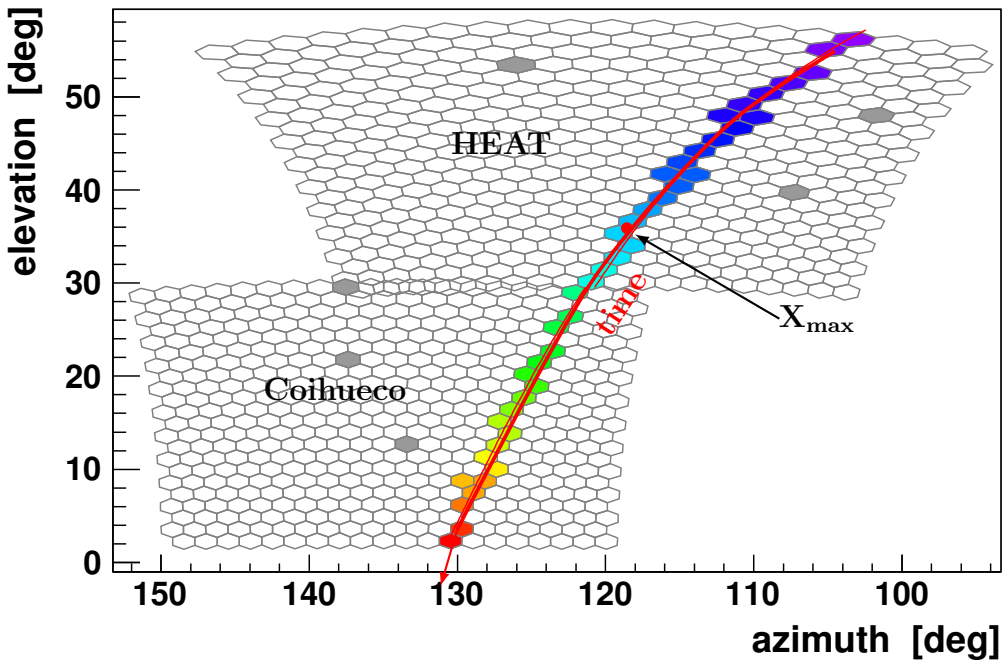

Figure 4.3.: Reconstructed shower axis of a shower seen by both HEAT and Coihueco. The temporal direction of the event is colour coded from blue (early) to red (late). The black line in each telescope denotes the reconstructed shower detector plane.

4.2. Shower Reconstruction

The standard FD reconstruction with the Auger $\overline{\text{Off}}\underline{\text{line}}$ software [45] (cf. sec. 3.3) works on the data provided by one eye[2]. Before HEAT was installed, an eye was the basic unit of the reconstruction. To reconstruct showers seen by multiple eyes, special modules exist, which have the disadvantage to not allow a combined energy reconstruction. Since events seen by multiple eyes have been very rare, this was not a problem.

As shown in fig. 3.1, HEAT is build as close as 170 m to the Coihueco eye. Therefore, many showers trigger both detectors and stereo events become the usual case. If HEAT is operated in tilted mode, the observed regions in the sky are complementary. Therefore, it is important to obtain a combined reconstruction of HEAT and Coihueco in all parameters, not only geometry. To achieve this goal, several parameters previously associated with an eye, such as the shower axis or the shower detector plane, became part of the telescopes description. So an eye became just a collection of telescopes. For the combined reconstruction of arbitrary telescope combinations, a *virtual eye* was introduced (cf. fig. 4.3) and implemented by S. Müller and M. Unger (both Karlsruhe group). The virtual eye, which is used for the combined reconstruction of HEAT and Coihueco, is called *CoHe*. Several $\overline{\text{Off}}\underline{\text{line}}$ modules needed to be modified to work with the changed structure [56].

[2]The FD buildings are called eye and consist of six telescopes.

4.2.1. T3 Rate Limiting

If HEAT is in its normal (tilted) operation mode, it observes low energy showers. Since the energy spectrum of the cosmic rays is described by a power law (cf. sec. 2.2), this implies a higher T3 trigger rate than at the regular detectors. A T3 trigger leads to a readout of the surface detector stations in the neighbourhood of the triggering eye. Because of the limited capacity of the wireless communication infrastructure between CDAS and the SD, the higher T3 trigger rate of HEAT leads to a saturation of this communication link and so disturbs the whole process of data taking. Therefore, the rate of HEAT T3s is limited to $0.02\,\mathrm{s}^{-1}$ to maintain a stable communication interface.

According to [56], it is assumed that up to two T3s in the time interval Δt are possible without disturbing the communication interface between CDAS and the SD. With an average event rate ω (this is the aforementioned rate of $0.02\,\mathrm{s}^{-1}$), the expected number of events in the time interval Δt is $N = \omega \cdot \Delta t$. The possibility to observe m events in Δt is given by Poisson statistics

$$P(m; \Delta t) = (\omega \cdot \Delta t)^m \, \frac{\mathrm{e}^{-\omega \cdot \Delta t}}{m!} \quad . \tag{4.1}$$

Therefore, the probability to observe more than two events in Δt is

$$P(m > 2; \Delta t) = 1 - \left(1 + \omega \cdot \Delta t + \frac{1}{2}\,(\omega \cdot \Delta t)^2\right) \mathrm{e}^{-\omega \cdot \Delta t} \quad . \tag{4.2}$$

If this probability is below 0.02 for two successive events (cf. [56]), which sent a T3 trigger to CDAS, the latest event is vetoed by the rate limiting of CDAS.

Because the rate limiting is only applied on T3 triggers sent from HEAT, this induces a bias on the field of view and consequently, a bias on the measured mass composition, too. The field of view bias is caused by the constraint that only hybrid events are used for the analysis, but those are rate limited for HEAT. To reduce the bias, the rate limiting has to be performed on the raw data again, but this time Coihueco events have to be treated such as HEAT. The correction leads to a suppression of Coihueco events, while HEAT was vetoed. Therefore, more events are lost.

The correction for the T3 rate limiting is performed with a small tool called `simpleMergerKG` written by S. Müller (Karlsruhe group). This tool is provided along with the development edition `OfflineKG`[3] and merges the raw data from Coihueco, HEAT and SD [56].

Currently, the Karlsruhe Group works on an alternative approach to solve the problem with the high T3 rate limiting. As at the energies below $10^{17.5}\,\mathrm{eV}$ in several events only the direct Cherenkov light is observed, which cannot be used for reconstruction with the existing setup, the alternative approaches aim to veto these non reconstructible events.

4.2.2. $\overline{\text{Off}}\underline{\text{line}}$ Module Sequence

The reconstruction of the merged raw data from HEAT, Coihueco and the SD is performed with the $\overline{\text{Off}}\underline{\text{line}}$ version v2r7p4 at the RWTH computing centre. The complete steering cards are located in the appendix A.1. An overview of the modules used for the FD hybrid reconstruction with HEAT is given here. The

[3] KG stands for **K**arlsruhe **G**roup which initiated it.

description is performed in the same order as their invocation in the reconstruction sequence.

FdCalibrator corrects each camera pixel for noise and baseline, and applies the calibration constant to convert the FD ADC traces to photon traces.

FdEyeMergerKG merges data from Coihueco and HEAT telescopes for a combined analysis in the virtual *CoHe* eye. In general, arbitrary telescopes can be added to the virtual eye.

FdPulseFinder determines the pulse centroid in time from the ADC trace of each pixel.

FdSDPFinder determines the shower detection plane (SDP) from the triggered pixels.

FdAxisFinder transforms the pointing of pixel i to angle χ_i and calculates the shower axis in the SDP.

HybridGeometryFinderOG uses the previously reconstructed shower geometry parameters of each telescope as initial values for a fit of χ_0, R_p and t_0 (cf. fig. 3.5) over all available telescopes in each eye. The timing information of the triggered SD station with the highest signal in a maximum distance of 2000 m is used, too.

HybridGeometryFinderWG like the HybridGeometryFinderOG uses previously determined shower geometry parameters as initial values for a fit on all telescopes available in the virtual eye.

FdApertureLightFinderKG calculates – based on the reconstructed shower geometry – the longitudinal light profile per telescope.

FdEnergyDepositFinderKG determines the Cherenkov and fluorescence ratio of the light trace. Based on the derived fluorescence light the energy deposit profile is determined and the Gaisser-Hillas function (eqn. 3.5) is fitted on this profile. The calorimetric energy of the shower is determined by integration over the determined Gaisser-Hillas function and an invisible energy correction is performed (cf. sec. 3.3). Also the depth of the shower maximum $X_{\max}$ is determined from the fit.

4.3. Reconstructed Showers

As stated earlier the goal of HEAT is to extend the observable energy range of the Pierre Auger Observatory to lower energies. To quickly check the reconstructed HEAT data, the soft cuts from table 4.1 are applied.

In fig. 4.4 the resulting energy and $X_{\max}$ distributions of HEAT and Coihueco (as a representative for a regular FD eye) are shown. As expected the reconstructible showers observed with HEAT are on average initiated by primaries with lower energy than for the regular FD. Also the $X_{\max}$ distribution measured with HEAT is on average lower than at regular FD. The conclusion from this very basic analysis of the HEAT data is, that HEAT is performing as expected.

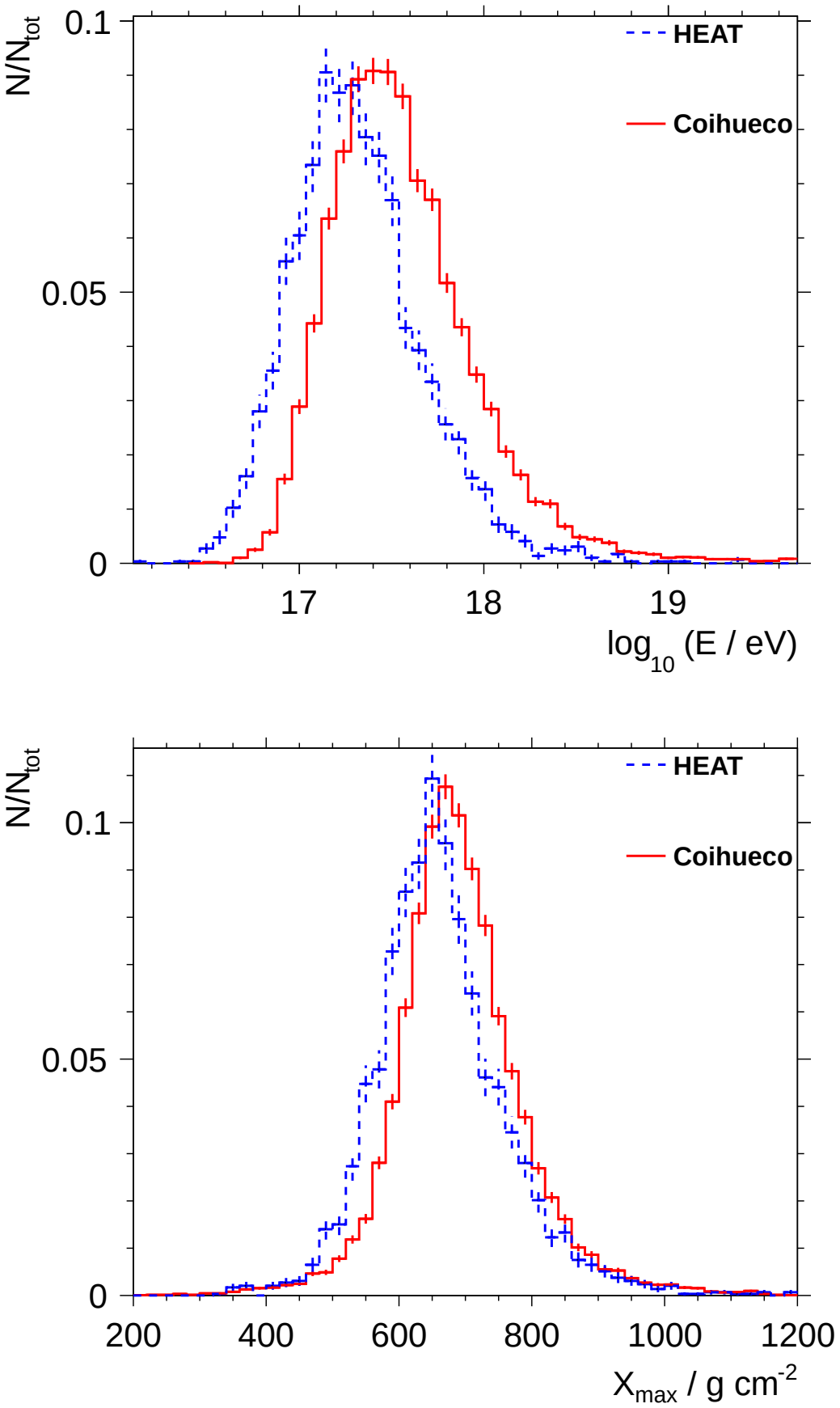

Figure 4.4.: Comparison of the energy and $X_{\max}$ distributions between HEAT (blue, dashed lined) and Coihueco (red, solid line) after applying soft cuts (cf. tab.4.1).

Cut	Event count	
	before	after
hybrid	359,966	78,339
$\sigma(E)/E < 100\,\%$	78,339	57,653
zenith angle $< 90°$	57,653	56,657
$\chi^2_{\mathrm{GH}}/N_{\mathrm{dof}} < \chi^2_{\mathrm{line}}/N_{\mathrm{dof}}$	56,657	24,013

Table 4.1.: Soft cuts used on CoHe data. $\chi^2_{\mathrm{GH}}/N_{\mathrm{dof}} < \chi^2_{\mathrm{line}}/N_{\mathrm{dof}}$ means that the longitudinal energy deposit profile must be better described by a Gaisser-Hillas function (eqn. 4.4) than a linear fit.

4.4. Monitoring

To get a better estimation of the performance of HEAT, it is necessary to take a look at the monitoring of the detector. Currently, the monitoring at the Pierre Auger Observatory consists of three parts:

- the atmospheric monitoring,
- the surface detector monitoring and
- the fluorescence detector monitoring.

The atmospheric monitoring covers the properties like temperature, air pressure, humidity, wind speed, cloud coverage and aerosol depth. For the SD and FD the uptime and parameters of the electronics are monitored. The FD properties are discussed in more detail in the following sections. Information about the SD monitoring can be found in [57].

The whole monitoring data is collected in a MySQL database located at the Pierre Auger Observatory's central campus in Malargüe. Besides, a mirror server exists in Wuppertal.

4.4.1. Uptime

A central part of the FD monitoring is the appropriate calculation of the uptime for several analyses, like the calculation of the exposure, which is needed for example for a FD energy spectrum analysis. Another important part is to check, whether the detector delivers data as expected.

Therefore, the FD data acquisition provides the start and stop time of each run. Additionally, it provides for each telescope and each telescope site ("eye") a dead time, which is generated by the electronics readout. Furthermore, the veto provided by the LIDARs[4], while laser shots for atmospheric monitoring are performed [58], is taken into account.

[4]The Light Detection And Ranging is used to monitor aerosols in the atmosphere.

Also the CDAS uptime and vetoes as well as disruptions of the communication between CDAS and the FD sites are considered in the monitoring. Finally, the following uptime parameters are provided by the observatory monitoring

- for each telescope site an uptime fraction,
- for each telescope the individual uptime fraction,
- CDAS uptime fraction,
- CDAS veto fraction,
- FDAS fraction and
- CDAS connection fraction.

For HEAT the monitoring was extended to also record the dead time induced by the T3 rate reduction. The monitoring data is provided in ten minute intervals. To compare the HEAT uptime with the uptime of the regular FD, the T3 rate reduction, if not stated else, is *not* considered in the uptime calculation.

The dead time of a telescope is mainly induced by the presence of the sun and nearly full moon on the sky. The presence of the moon within a distance of 5° to the field of view of a telescope and bad weather lead to dead time, too. Due to the astronomical restrictions on the operation of a telescope, most of the time not all telescopes are simultaneously operational. All telescopes at one site can be operated together on about eight days a month.

To analyse the HEAT uptime, only the runs with HEAT in upward mode are interesting, because this criterion is also used for the event selection. For the uptime calculations used in this analysis the period from 2010/06/01 until 2011/08/31 is considered. Fig. 4.5 shows the cumulated uptime calculated from the monitoring database for each of the three HEAT telescopes and for the complete HEAT eye. The eye uptime is an upper limit to the uptime of the single telescopes. The maximum uptime only constrained by the aforementioned astronomical restrictions, is shown as a dashed line. As it can be expected, the maximal possible uptime is never reached due to e.g. bad weather or artificial light sources interrupting runs. Due to a frozen tilting mechanism in August of 2010, all HEAT telescopes were in downward mode, which strongly reduced the integrated HEAT uptime.

To check whether the HEAT uptime diverges from the astronomically achievable uptime, the ratio of the gained uptime of the HEAT eye ($t_{\mathrm{Uptime,HEAT_{real}}}$) and the astronomically achievable uptime ($t_{\mathrm{Uptime,HEAT_{max}}}$) are considered (cf. fig. 4.6). Besides the drop of the ratio at August 2010, the ratio of the gained and the achievable uptime increases. Since April 2011 the ratio converges against a rather constant value of about 0.7, which means that HEAT reaches 70 % of the astronomically expected uptime without considering the T3 rate reduction as a dead time.

Another benchmark for the HEAT uptime is the uptime measured at a regular eye. This is a more realistic benchmark, because like HEAT the regular FD uptime is subject to readout, monitoring and weather induced dead times. A good FD eye for a comparison is the Coihueco eye, because of its proximity to HEAT both are probably affected in the same way by external influences. However, HEAT and Coihueco observe different parts of the sky, so e.g. the aforementioned higher trigger rate could effect the dead time. The integrated uptime of both eyes and the maximal achievable uptime is shown in fig. 4.7. Besides the frozen tilting

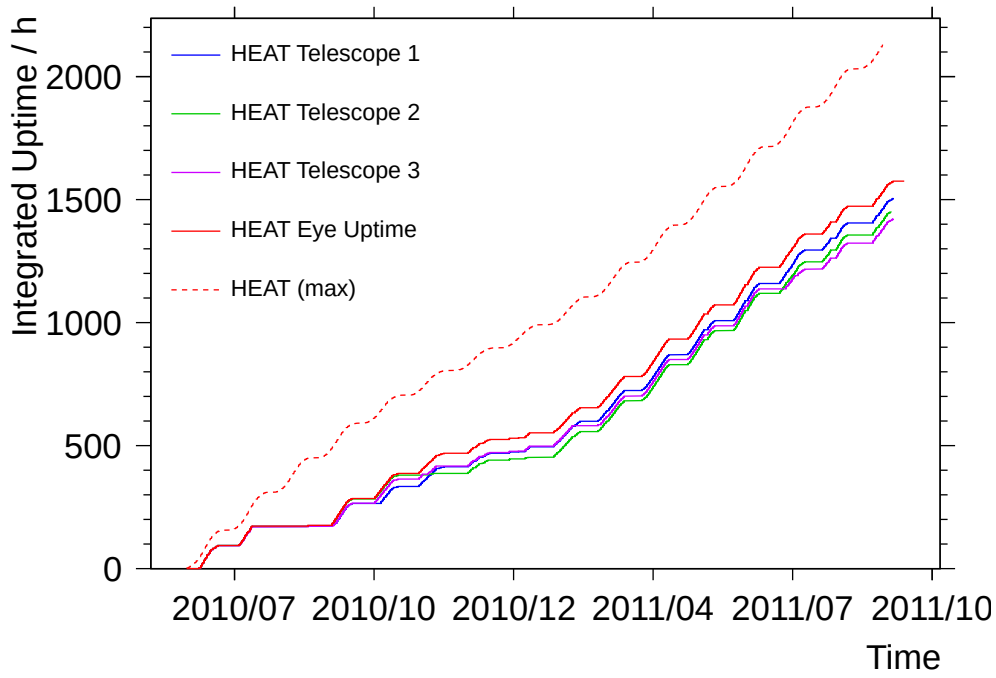

Figure 4.5.: Integrated uptime of each HEAT telescope and the whole eye (red solid line) in a ten minute binning. The dashed line denotes the maximal achievable uptime, which is only limited by astronomical constraints. Only times with telescopes in upward position are accounted for. T3 rate reduction is not considered. In August 2010 a downtime was induced by a frozen tilting mechanism.

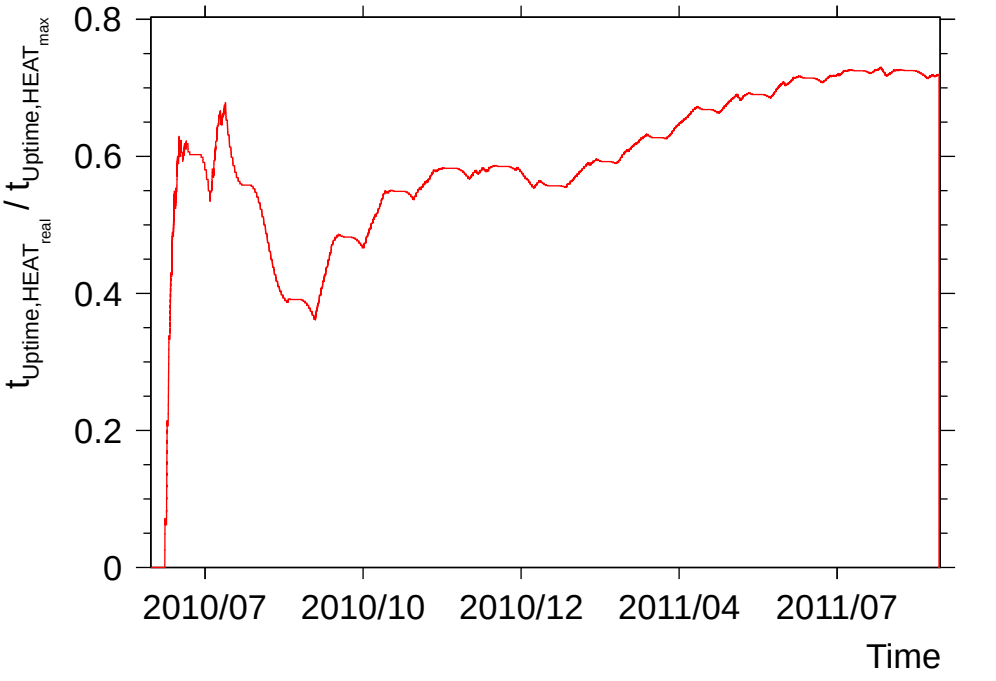

Figure 4.6.: The ratio of the gained uptime of the HEAT eye ($t_{\mathrm{Uptime,HEAT_{real}}}$) and the astronomical achievable uptime ($t_{\mathrm{Uptime,HEAT_{max}}}$). T3 rate reduction is not considered.

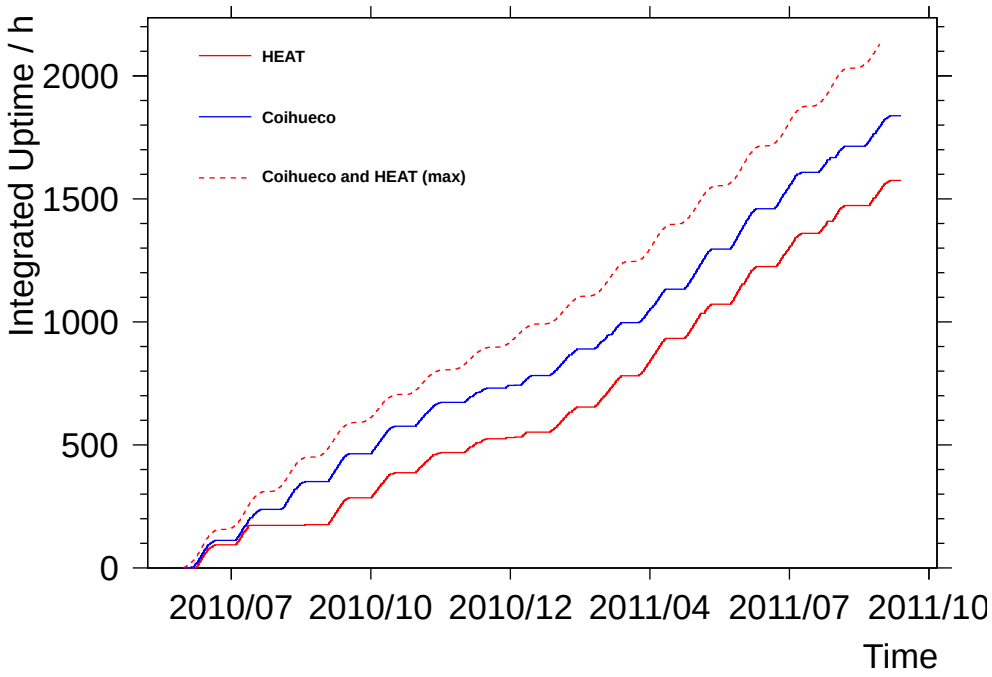

Figure 4.7.: Integrated uptime of HEAT and Coihueco including common maximal achievable uptime in a ten minute binning. All Coihueco uptimes are considered but only HEAT uptime periods in upward mode. T3 rate reduction is not considered.

mechanism of HEAT in August 2010 there are no apparent differences in the uptime between both eyes.

Like for the comparison of the gained HEAT uptime with the maximal achievable uptime, the ratio of the HEAT and the Coihueco uptime are considered (fig. 4.8). As before, a drop of the ratio in August 2010 is identifiable, which can be expected since Coihueco is not influenced by the frozen tilting mechanism of HEAT. Besides this drop, an increase of the ratio is evident. As expectable, because more dead time inducing effects are considered, the uptime ratio of HEAT and Coihueco is higher than the ratio of the HEAT uptime and the astronomically achievable uptime. However, since April 2011 the ratio hints on a constant value of the HEAT uptime, which is about 85 % of the Coihueco uptime without considering the T3 rate reduction as a dead time.

Additionally, fig. 4.9 shows the Coihueco and HEAT uptime, including the effect of the T3 rate reduction. Taking the T3 rate reduction into account, leads to an increasing difference between both eyes. In the time period accounted for, the HEAT uptime is reduced from 1575 to 1214 hours. This means a reduction of the uptime by about 23 % due to the limitations in the SD communication system (cf. fig. 4.10).

One can state that HEAT has a cumulated uptime of 1214 hours (including effects of T3 rate reduction) in upward mode from June 2010 until end of August 2011. In the same time the Coihueco eye gained an uptime of 1838 hours. Furthermore, it is noticeable that the introduced T3 rate limiting of HEAT triggers' reduces the effective HEAT uptime by about 20 %.

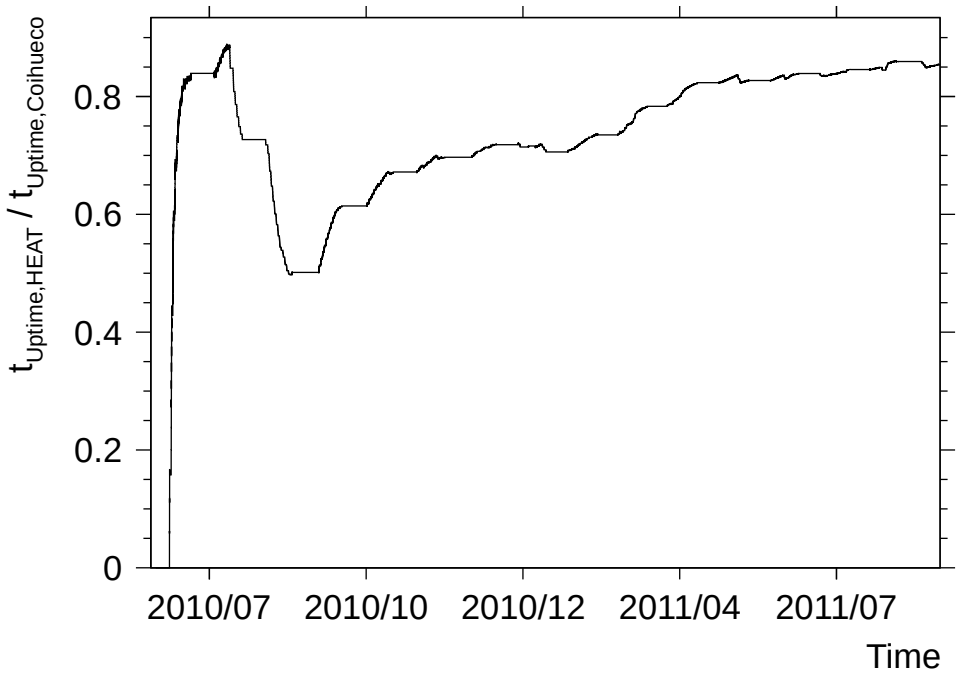

Figure 4.8.: The ratio of the uptime of HEAT ($t_{\mathrm{Uptime,HEAT}}$) and Coihueco ($t_{\mathrm{Uptime,Coihueco}}$). T3 rate reduction is not considered.

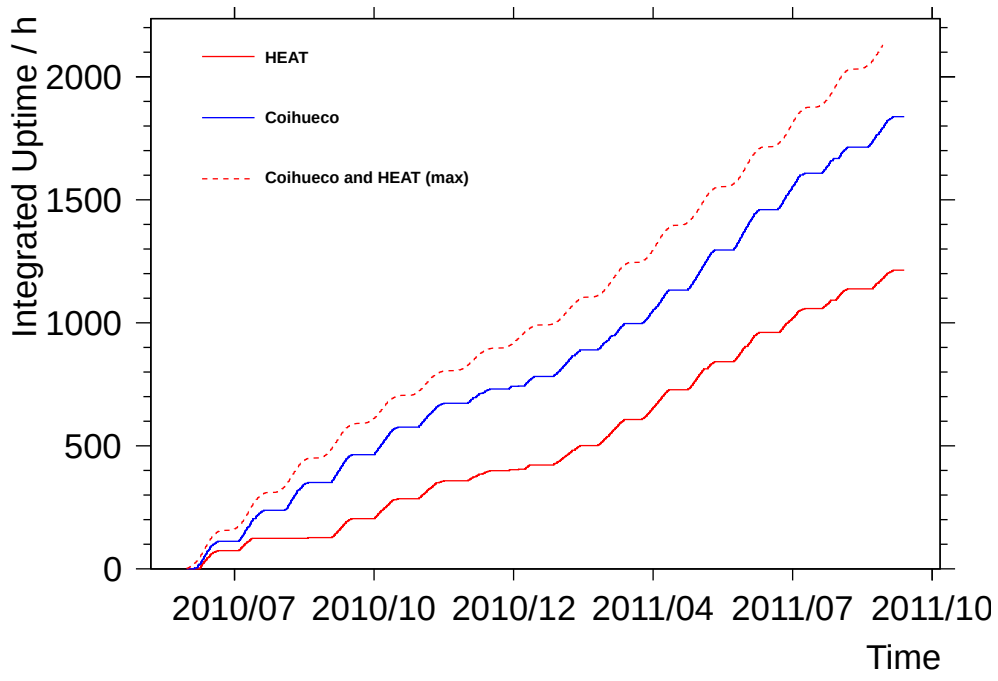

Figure 4.9.: Integrated HEAT upward and Coihueco eye uptime. HEAT T3 rate reduction is considered.

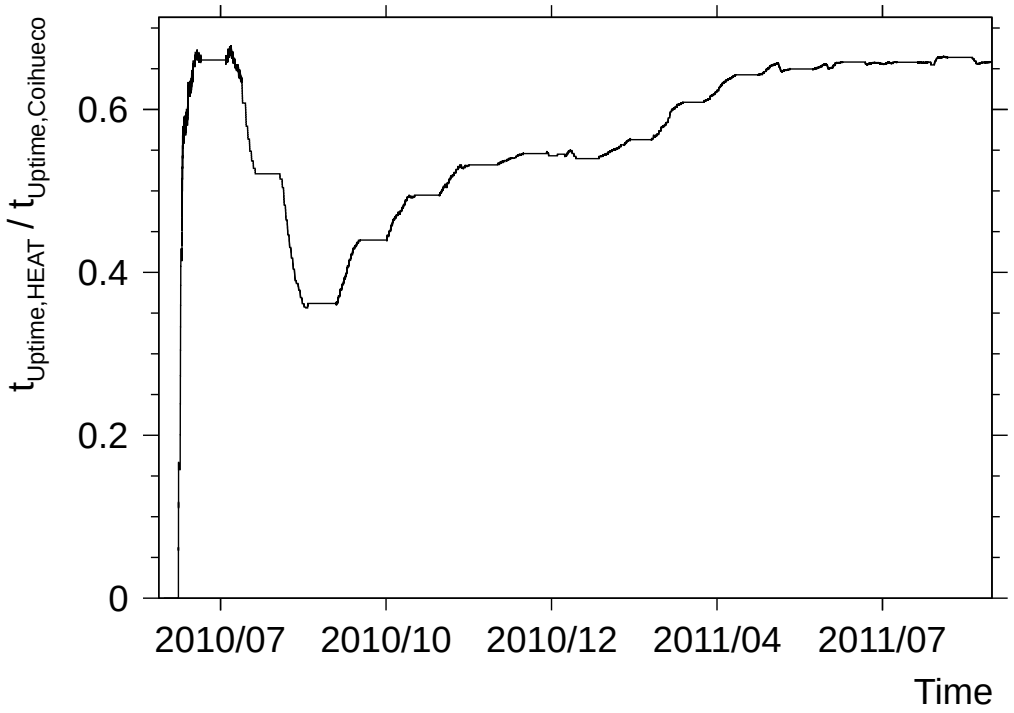

Figure 4.10.: The ratio of HEAT's ($t_{\mathrm{Uptime,HEAT}}$) and Coihueco's ($t_{\mathrm{Uptime,Coihueco}}$) uptime. T3 rate reduction is considered.

4.4.2. FD Electronics Monitoring

Additionally to the uptime, the state of the FD electronics is monitored. Following [59], the necessary information to understand the used quantities is presented.

Each camera row, which consists of 22 pixels, is processed by one front-end electronics module. A front-end module consists of four peripheral FPGAs[5] each handling six pixels and a controller FPGA, which acts as an interface to the MirrorPC and the analog front-end. Each pixel consists of one PMT.

Besides other functions like the first level trigger, the peripheral FPGAs implement the FD electronics monitoring. The monitoring calculates for each pixel the variance σ^2 and the pedestal μ. This is realized by calculating the sums $\sum_i x_i$ and $\sum_i x_i^2$ over $N = 2^{16} - 1$ successive 12-bit ADC values x_i. Shower signals are distinguished from the background by rejecting $x_i - x_{\text{mean}} \geq 256$ for the monitoring. The value of x_{mean} is derived during the calibration of the detector and is common for all pixels controlled by one peripheral FPGA.

The variance and pedestal per pixel are derived as

Pedestal

$$\mu = \frac{1}{N} \sum_{i=1}^{N} x_i \tag{4.3}$$

Variance

$$\sigma^2 = \frac{1}{N-1} \left(\sum_{i=1}^{N} x_i^2 - \mu N \right) \tag{4.4}$$

from these quantities. Every 30 s these values are fetched by the MirrorPC and are stored in the monitoring database.

According to [60], the calculated ADC variance is an estimator for the anode DC current, which itself is an estimator of the background light seen by the pixel. The background light sensitivity allows to track stars with the FD [61, 62, 63]. Stars like extensive air showers produce a track on the FD cameras. While stars move in the order of hours through the cameras' field of view, the relative slow electronics monitoring is capable to deliver precise enough timing information. With the knowledge of bright star's coordinates in the field of view of a telescope, and an algorithm to identify pixels with a relative high background light flux, it is possible to correlate the star positions with the pointing of these "hot" pixels. The star tracking allows a very precise calibration of the absolute pointing of the telescope. Compared to the pointing in use, the star tracking method shows a deviation of about $\pm 0.1°$ in elevation and azimuth (cf. [62]).

Furthermore, the ADC variance is also sensitive to changes in the PMT's operation parameters, e.g. it is possible to diagnose a high voltage supply not working at the designated voltage. In fig. 4.11a a block of 4×11 PMTs, at a lower than the designated operation voltage, is visible. This interpretation is supported by the operator's log of this shift. A contrary effect, a single pixel with very high ADC variances is visible in fig. 4.11b.

Besides variance and pedestal also the first level trigger threshold is stored. The threshold is recalculated every 1000 samples for each channel. The electronic counts the hits in the buffer and readjusts the threshold to maintain a first level trigger rate of 100 Hz.

[5] **F**ield **P**rogramable **G**ate **A**rray is an integrated circuit which can be configured after manufacturing.

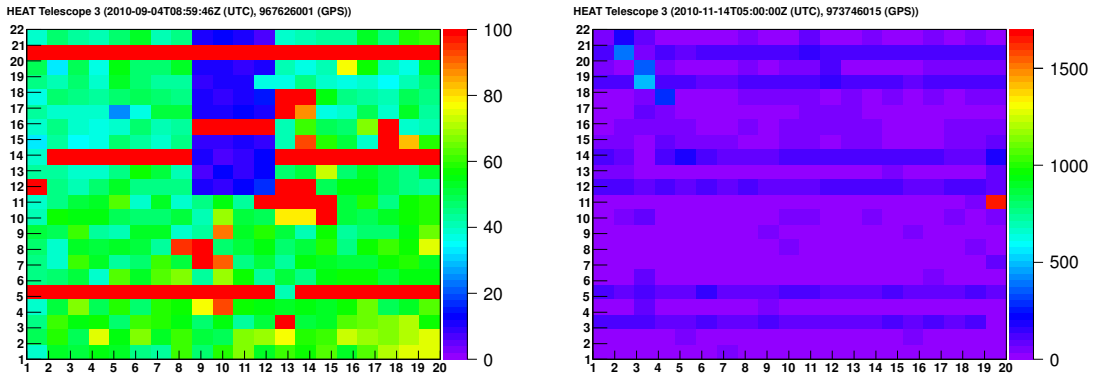

(a) A 4 × 11 PMT group not working at designated voltage.

(b) One camera pixel (red coded) showing a significantly higher ADC variance.

Figure 4.11.: Colour coded camera view of ADC variances in HEAT telescope 3 averaged over one hour. The vertical and horizontal axis codes the position of the PMTs and the colour code represents ADC variance in one pixel. The scaling of the $(\text{ADC Counts})^2$ (z-axis) is different for the two pictures.

Irregularities in HEAT monitoring

HEAT is a new detector based on the design of the regular telescopes of the Pierre Auger Observatory. But the differences in design (faster FADC) and the different observed part of the atmosphere can lead to a different behaviour in the monitoring. In the following, the ADC variance is considered as a self-contained observable. This can be justified because the ADC variance is an observable of the background light flux (cf. [60]).

In the following, the abbreviation AV means ADC Variance. The average ADC variance $\langle \text{AV} \rangle$ and the uncertainty on the average $\sigma(\text{AV})$ of N ADC variances is calculated by:

$$\langle \text{AV} \rangle = \frac{1}{N} \sum_{i=1}^{N} \text{AV}_i \tag{4.5}$$

$$\sigma\left(\text{AV}\right) = \sqrt{\frac{1}{N-1} \sum_{i=1}^{N} \left(\text{AV}_i - \langle \text{AV} \rangle\right)^2} \tag{4.6}$$

Fig. 4.12 shows the average of the ADC variances over all pixels per month of each telescope of HEAT and Coihueco (representative for a regular eye) from June 2010 to June 2011. The average ADC variances of Coihueco are between 20 and 30 $(\text{ADC Counts})^2$ with a statistical uncertainty of about 10 $(\text{ADC Counts})^2$ for each telescope (cf. table 4.3). The difference between the telescopes is much smaller than the statistical uncertainties.

In March 2011 the average ADC variances of all Coihueco telescopes increased by about 5 $(\text{ADC Counts})^2$ and the uncertainties on the average ADC variances are increased by a factor between 1.8 and 5.9. The small increase of the mean value compared to previous changes is not very uncommon. If the increased uncertainty on the average ADC variance is taken into account, too, this indicates that the background light flux fluctuated more in this month and that the light flux was higher than usual. According to the shifters' log, in this period works were nightly performed at the Coihueco site, which increased the background light.

Eye	Year 2010						
	6	**7**	**8**	**9**	**10**	**11**	**12**
Coihueco	21±2	24±1	28±3	29±2	29±1	29±2	25±2
HEAT	23±2	26±1	26±2	30±1	34±2	35±5	35±4

Eye	Year 2011					
	1	**2**	**3**	**4**	**5**	**6**
Coihueco	26±2	26±1	30±2	38±2	33±2	26±2
HEAT	28±5	30±7	36±6	40±5	35±4	28±1

Table 4.2.: Monthly averages of the ADC variance in $(\text{ADC Counts})^2$ over all Coihueco and HEAT telescopes from 2010/06 until 2011/06. The uncertainties are without propagation of the uncertainties per telescope from tab. 4.3.

Besides anthropogenic light, the dominant source of nightly background light is airglow. Airglow describes the fact that due to the UV radiation of the sun ionized atoms or dissociated molecules, recombine and emit photons. The contribution of airglow varies with the elevation. The more atmospheric mass is in the line-of-sight, the higher is the contribution of the airglow to the background light. For angles close to the horizon the contribution of airglow is largest. The parametrization used for the FD telescopes at the Pierre Auger Observatory is described in [64].

Therefore, a lower value of $\langle \text{AV} \rangle$ can be expected at HEAT. But table 4.2 shows that the value of $\langle \text{AV} \rangle$ of the HEAT cameras is on average higher than for Coihueco. However, they are at least compatible in overlapping 2σ intervals. More interesting are the statistical uncertainties on the monthly average of individual telescope's ADC Variance. These are between 1.5 and 8 times higher at HEAT than at Coihueco. This indicates higher fluctuations of the ADC variance during a month or between pixels, for example single noisy pixels. Therefore, a closer look on the monitoring data is necessary.

To inspect the reason of the big uncertainty on $\langle \text{AV} \rangle$ at HEAT, it is reasonable to take a look at the distribution of the ADC variance in all pixels of the camera. A representative example is shown in fig. 4.13. The ADC variance distributions of the other HEAT and Coihueco telescopes can be found in appendix C.1 p. 99. As one can expect from the previously presented monthly ADC variance averages (cf. tab. 4.3 and cf. fig. 4.12), the most time the monitoring records ADC variances between 20 and 50 $(\text{ADC Counts})^2$ in all pixels for both FD sites. At Coihueco the distribution flattens fast and values over 400 $(\text{ADC Counts})^2$ only occur sporadically. However, besides the main maximum at about 50 $(\text{ADC Counts})^2$ (about half a million entries) HEAT shows several local maxima with each about 1000 entries. This clearly leads to the elevated uncertainty on the telescopes' monthly ADC variance average.

To verify whether the local maxima are driven by single pixels or a group of pixels, the discrimination value between the lowest $x\,\%$ and highest $(100 - x)\,\%$ values of AV for each camera pixel is determined. As each available monitoring information about a pixel corresponds to a time period of ten minutes, the resulting value also means that at $x\,\%$ of the operation time the ADC Variances was below the determined quantile.

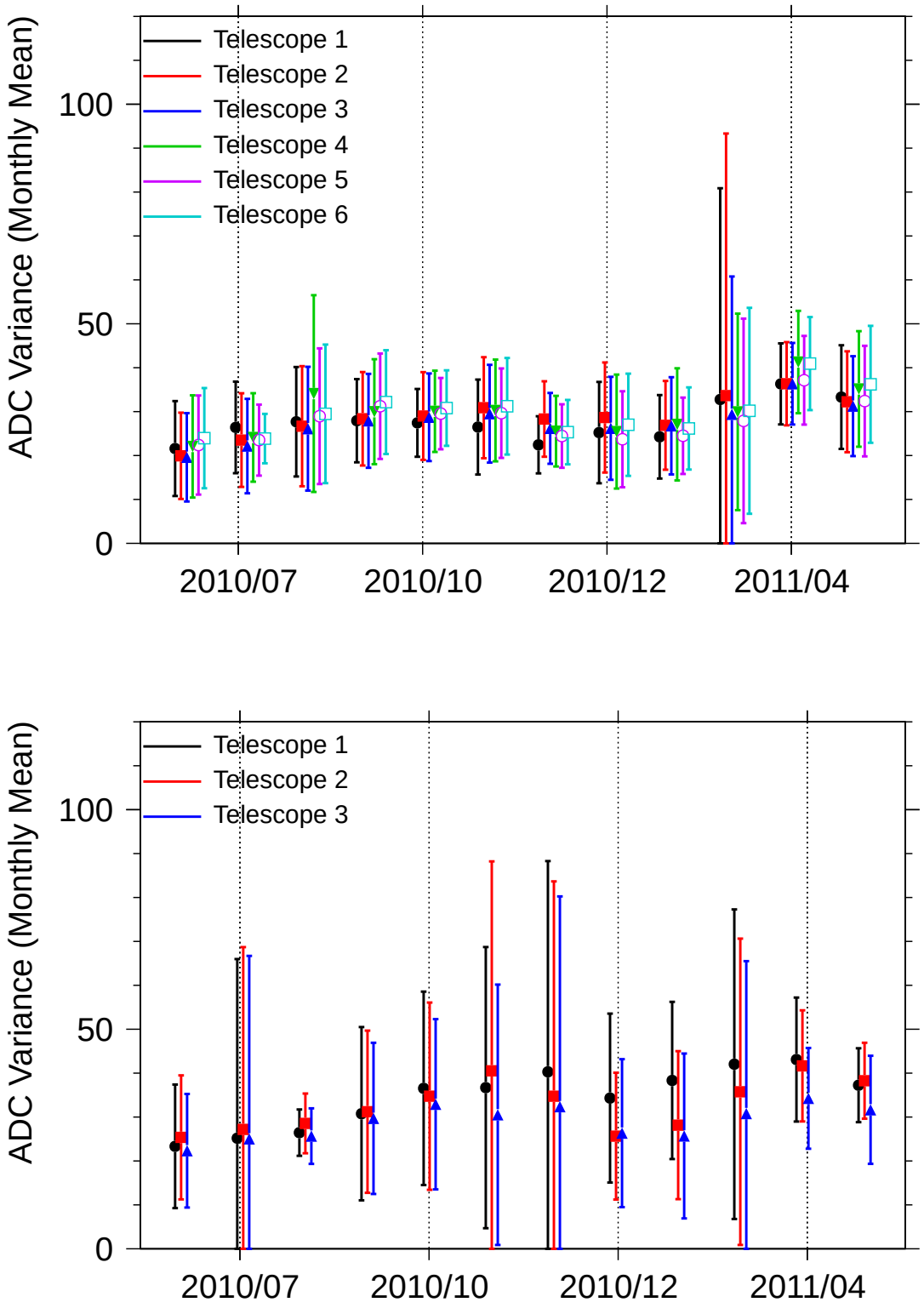

Figure 4.12.: Monthly average ADC Variances in units of (ADC Counts)^2 integrated over the whole camera for each HEAT and Coihueco telescope from June 2010 to June 2011.

Month	Coihueco Telescopes						HEAT Telescopes		
	1	2	3	4	5	6	1	2	3
2010/6	21^{+10}_{-10}	19^{+9}_{-9}	19^{+10}_{-10}	22^{+11}_{-11}	22^{+11}_{-11}	23^{+11}_{-11}	23^{+14}_{-14}	25^{+14}_{-14}	22^{+12}_{-12}
2010/7	26^{+10}_{-10}	23^{+10}_{-10}	22^{+10}_{-10}	24^{+10}_{-10}	23^{+8}_{-8}	23^{+5}_{-5}	25^{+40}_{-25}	27^{+41}_{-27}	25^{+41}_{-25}
2010/8	27^{+12}_{-12}	26^{+13}_{-13}	26^{+14}_{-14}	34^{+22}_{-22}	28^{+15}_{-15}	29^{+15}_{-15}	26^{+5}_{-5}	28^{+6}_{-6}	25^{+6}_{-6}
2010/9	27^{+9}_{-9}	28^{+10}_{-10}	27^{+10}_{-10}	29^{+11}_{-11}	31^{+12}_{-12}	32^{+11}_{-11}	30^{+19}_{-19}	31^{+18}_{-18}	29^{+17}_{-17}
2010/10	27^{+7}_{-7}	28^{+9}_{-9}	28^{+9}_{-9}	30^{+9}_{-9}	29^{+8}_{-8}	30^{+8}_{-8}	36^{+22}_{-22}	34^{+21}_{-21}	32^{+19}_{-19}
2010/11	26^{+10}_{-10}	30^{+11}_{-11}	29^{+11}_{-11}	30^{+11}_{-11}	29^{+10}_{-10}	31^{+10}_{-10}	36^{+32}_{-32}	40^{+47}_{-40}	30^{+29}_{-29}
2010/12	22^{+6}_{-6}	28^{+8}_{-8}	26^{+8}_{-8}	25^{+8}_{-8}	24^{+7}_{-7}	25^{+7}_{-7}	40^{+47}_{-40}	34^{+48}_{-34}	32^{+47}_{-32}
2010/13	25^{+11}_{-11}	28^{+12}_{-12}	26^{+11}_{-11}	25^{+12}_{-12}	23^{+10}_{-10}	27^{+11}_{-11}	34^{+19}_{-19}	25^{+14}_{-14}	26^{+16}_{-16}
2011/2	24^{+9}_{-9}	26^{+10}_{-10}	26^{+11}_{-11}	27^{+12}_{-12}	24^{+8}_{-8}	26^{+9}_{-9}	38^{+17}_{-17}	28^{+16}_{-16}	25^{+18}_{-18}
2011/3	32^{+48}_{-32}	33^{+59}_{-33}	29^{+31}_{-29}	29^{+22}_{-22}	27^{+23}_{-23}	30^{+23}_{-23}	42^{+35}_{-35}	35^{+34}_{-34}	30^{+34}_{-30}
2011/4	36^{+9}_{-9}	36^{+9}_{-9}	36^{+9}_{-9}	41^{+11}_{-11}	37^{+10}_{-10}	40^{+10}_{-10}	43^{+14}_{-14}	41^{+12}_{-12}	34^{+11}_{-11}
2011/5	33^{+11}_{-11}	32^{+11}_{-11}	31^{+11}_{-11}	35^{+13}_{-13}	32^{+12}_{-12}	36^{+13}_{-13}	37^{+8}_{-8}	38^{+8}_{-8}	31^{+12}_{-12}
2011/6	28^{+11}_{-11}	25^{+10}_{-10}	24^{+10}_{-10}	26^{+10}_{-10}	25^{+10}_{-10}	28^{+11}_{-11}	27^{+8}_{-8}	29^{+8}_{-8}	28^{+23}_{-23}

Table 4.3.: Monthly average of ADC Variance in $(\text{ADC Counts})^2$ for each telescope camera of Coihueco and HEAT from 2010/06 until 2011/06. The uncertainty asymmetry arises from the exclusion of negative values, because the ADC Variance is defined as a positive value.

Fig. 4.14 and fig. 4.15 show the 95 %, 99 % and 99.9 % quantiles for two representative telescopes. The other HEAT and Coihueco telescopes can be found in appendix C.2 on p. 101. For all pixels in all considered telescopes the 95 % quantile is below 160 $(\text{ADC Counts})^2$ and the average is about 50 $(\text{ADC Counts})^2$.

At a quantile of 99 % a difference between Coihueco and HEAT is evolving. For Coihueco the quantile is just slightly increasing for the most pixels with a discrimination level of up to about 240 $(\text{ADC Counts})^2$ for single pixels. But for HEAT the 99 % quantile is at about 400 $(\text{ADC Counts})^2$ for most pixels and up to 1500 $(\text{ADC Counts})^2$ for single pixels. Additionally, the 99.9 % quantile of HEAT is around 3400 $(\text{ADC Counts})^2$. While at Coihueco still only single pixels has a higher ADC Variance than 500 $(\text{ADC Counts})^2$.

Firstly, this means that the higher uncertainty on the average ADC Variance on HEAT is not generated by single faulty pixels generating noise. However, it is systematic to all HEAT pixels to show at about one of thousand times a high ADC variance. Therefore, the current regular FD detector simulation cannot fully simulate the behaviour of the HEAT electronics. Since the simulation is not yet fitted to this differences, another approach of the HEAT detector simulation has to be used. This approach is described in the next chapter.

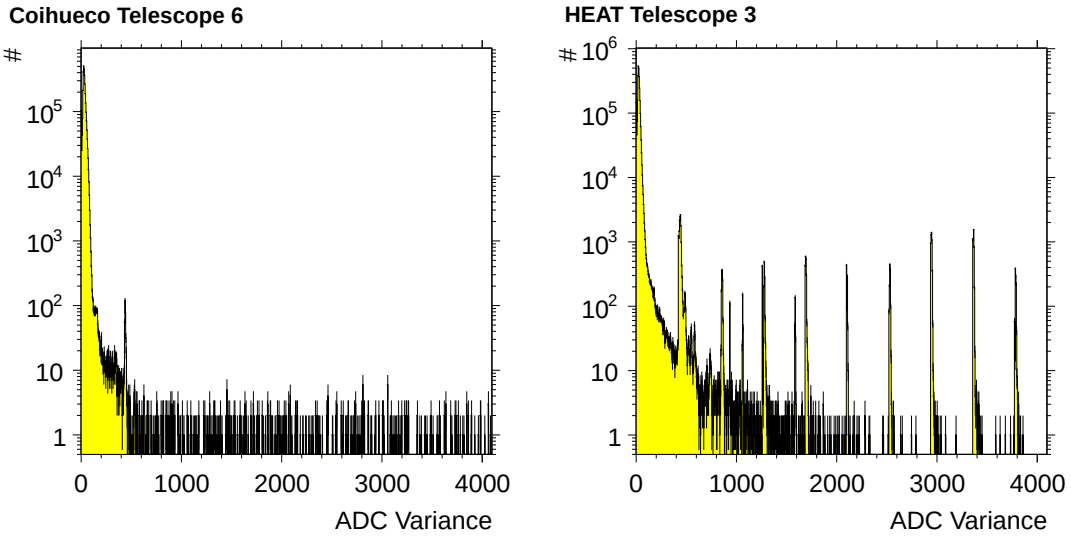

Figure 4.13.: Distribution of integrated ADC Variances in units of (ADC Counts)^2 of one HEAT and one Coihueco telescope from 2010/06 until 2011/06. Main difference between both are the distinctive local maxima in the HEAT distribution, which lead to an increased uncertainty on the monthly ADC Variances' average.

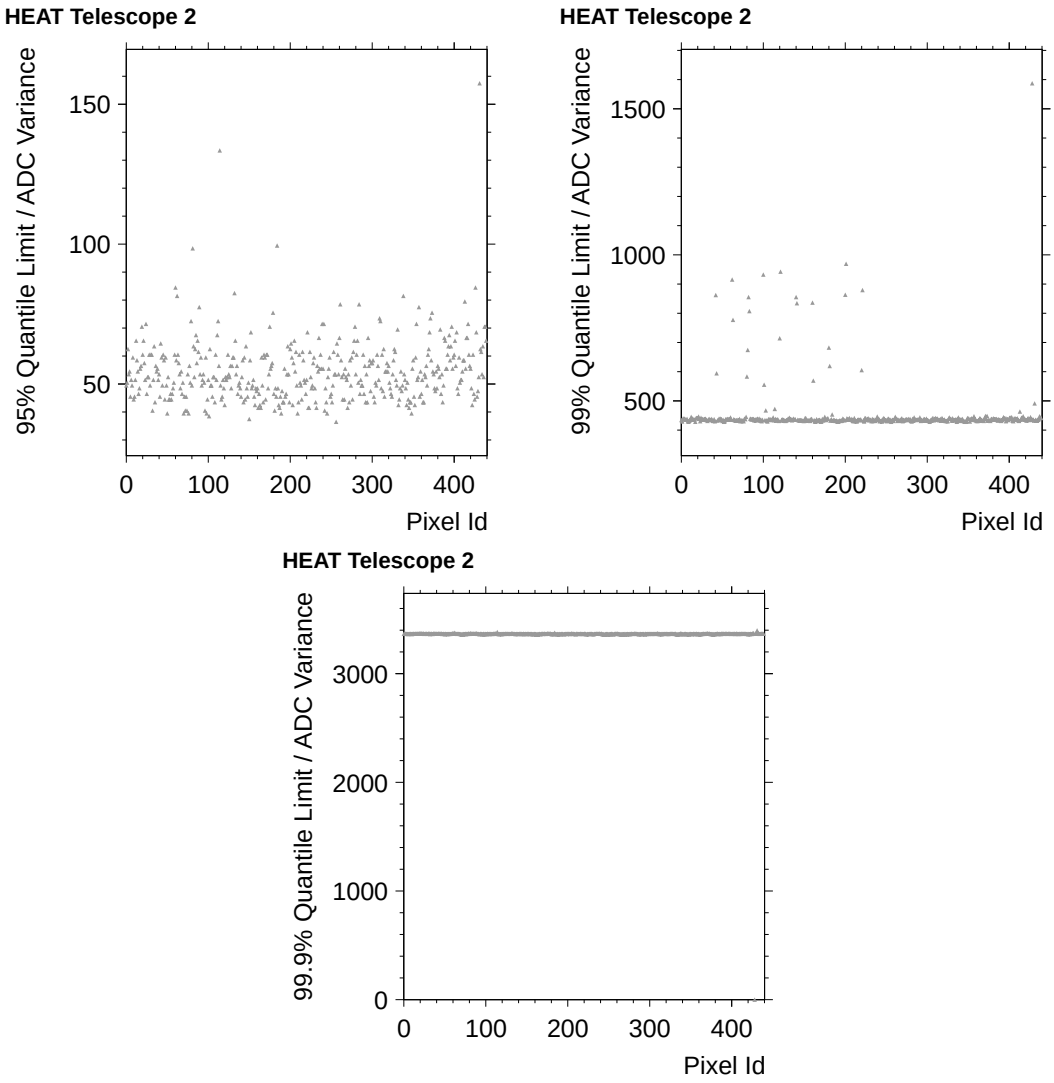

Figure 4.14.: 95 %, 99 % and 99.9 % quantile ADC Variance threshold in units of $(\mathrm{ADC\,Counts})^2$ for each pixel of HEAT telescope 2 from 2010/06 until 2011/06.

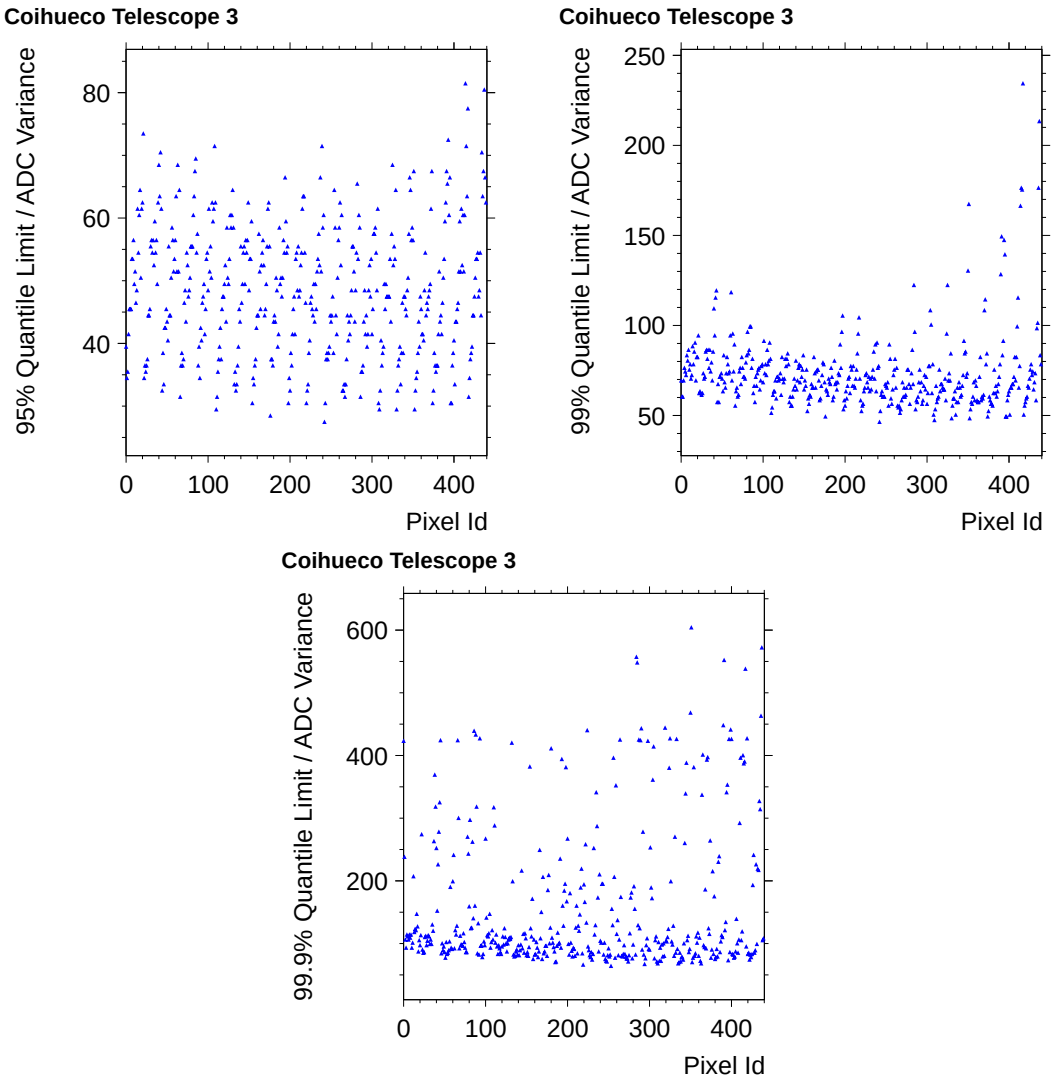

Figure 4.15.: 95 %, 99 % and 99.9 % quantile ADC Variance threshold in units of $(\mathrm{ADC\,Counts})^2$ for each pixel of Coihueco telescope 3 from 2010/06 until 2011/06.

5. Shower and Detector Simulation for HEAT

In general, the aim of simulations is to determine detector resolution and reconstruction bias, so that the measured data can be corrected for these effects. It also enables an optimization of the event selection. The simulation of the fluorescence detector of the Pierre Auger Observatory is performed in three steps – which can be done altogether in one run. The first step is to simulate the shower in the atmosphere. The next step is to simulate the detector response to the simulated shower. Finally, the simulated shower is reconstructed in the same way as a real shower. The detector simulation and shower reconstruction is performed with the Auger $\overline{\text{Off}}\underline{\text{line}}$ [45] software package.

5.1. Shower Library

The used shower simulations were done by Nils Scharf [65] by using the extensive air shower simulation package CONEX [36]. CONEX uses a hybrid strategy for simulation. This means that for high energy interactions Monte Carlo simulations are used, and for the resulting secondary particles cascade equations are numerically solved. This approach reduces the needed CPU time for primary energies of about 10^{18} eV significantly to about 60 s (depends on the used hadronic interaction model and primary) per shower on a modern Intel XEON CPU. For comparison, a full featured Monte Carlo simulation at the same energy with CORSIKA [66] takes some days per shower. To reduce the computational time to some hours, CORSIKA uses the method of *thin sampling* [67]. If the shower development is advanced enough and many secondary particles exist, thin sampling randomly selects particles after interactions to be representative and discards the others. More detailed information is available in [67]. With an increasing level of thin sampling, the statistical fluctuations of the simulated showers increases, too.

Therefore, CONEX has the advantage of easily increasing the statistics of the simulation, which allows a fast determination of systematic detector effects for different shower parameters like zenith angle, energy, kind of primary and hadronic interaction model. The output is produced as a ROOT [68] file.

CONEX can use several models for the simulation of the hadronic interactions. In this work the EPOS [37], Sibyll 2.1 [35, 69] and QGSJet II-03 [70, 71] models are used. For each hadronic interaction model, the simulations are performed with proton and iron primaries. Protons are chosen because they are the lightest and simplest stable atomic ions. Iron nuclei have the highest binding energy and are therefore very stable. According to the design energy range of HEAT, the showers are simulated from $10^{17.0}$ eV to $10^{18.5}$ eV. The simulation is performed in energy bins with a width of 0.25 in $\log_{10}(E/\text{eV})$ with bin centers at 10^{17}, $10^{17.25}$, $10^{17.5}$, $10^{17.75}$, 10^{18}, $10^{18.25}$ and $18^{18.5}$ eV. For each energy bin ten thousand showers per interaction model and primary were simulated with a flat angular distribution of the arrival direction of the cosmic rays.

5.2. Time Dependent Detector Simulation

In the Auger detector simulation the detector response to the simulated showers is created. For the fluorescence detector this means the simulation starts with the simulation of fluorescence and Cherenkov light in the atmosphere based on the simulated longitudinal shower profile. The produced light is then ray traced through the atmosphere and the telescopes' optics. Afterwards, the response of the PMTs to the ray traced light flux is simulated. The PMT signal is then passed to a simulation of the trigger logic. If the simulated trigger logic accepts the event, it is stored to disk. The simulation of the fluorescence detector is described in more detail in [72].

For the final data analysis only FD hybrid data will be used, which means that only FD events for which also a station of the surface detector has triggered are considered. So it is necessary to also simulate the surface detector. But due to the fact that only the timing information of the surface detector is used in hybrid reconstruction (cf. sec. 3.3), it is not necessary to perform a full featured simulation of the SD[1]. For this purpose the Offline module `SdSimpleSimKG` [73] exists, which simulates the lateral shower signal based on the longitudinal CONEX shower profile. The full module chain for the detector simulation is shown in appendix A.2 (p. 94).

The standard detector simulation assumes a static, always perfectly working detector. But, as shown in sec. 4.4, essential parameters of the detector vary with time. Therefore, Offline contains the possibility to use the collected monitoring data to simulate the time dependent detector. This dynamic simulation is called RealMC. The process scheme is shown in fig. 5.1. Because the surface detector is just simulated to be used for timing, the data from SD monitoring is not used – and can not be used with `SdSimpleSimKG`. This means that the SD is assumed to be in ideal condition. So the usable monitoring data is reduced to those obtained from atmospheric and fluorescence detector monitoring. However, while the absolute calibration of HEAT is still work in progress, the collected atmospheric monitoring data cannot be processed because their analysis relies on the absolute calibration, too. Therefore, only the information from FD electronics monitoring is considered in RealMC.

The detector simulation is done for the same time range as data is considered for the following analysis, which is from 2010/06 until 2011/06. To gain as much showers as possible from the MC, only times with an – according to the monitoring – active detector are used in simulation, otherwise showers simulated at times of a deactivated detector would be rejected by the simulation. To gain more statistics in simulation, the detector simulation is performed five times with the same CONEX showers but using different seeds for the random number generators in Offline, which amongst others lead to a different positioning of the shower in the array. The shower cores are uniformly distributed in the field of view of HEAT and Coihueco (in technical terms "eye centric" between the third and fourth telescope of Coihueco).

With the output of the detector simulation, the Auger hybrid reconstruction modified for the use with HEAT is done (cf. sec. 4.2).

[1] This is not possible with CONEX showers because the lateral particle distribution is missing.

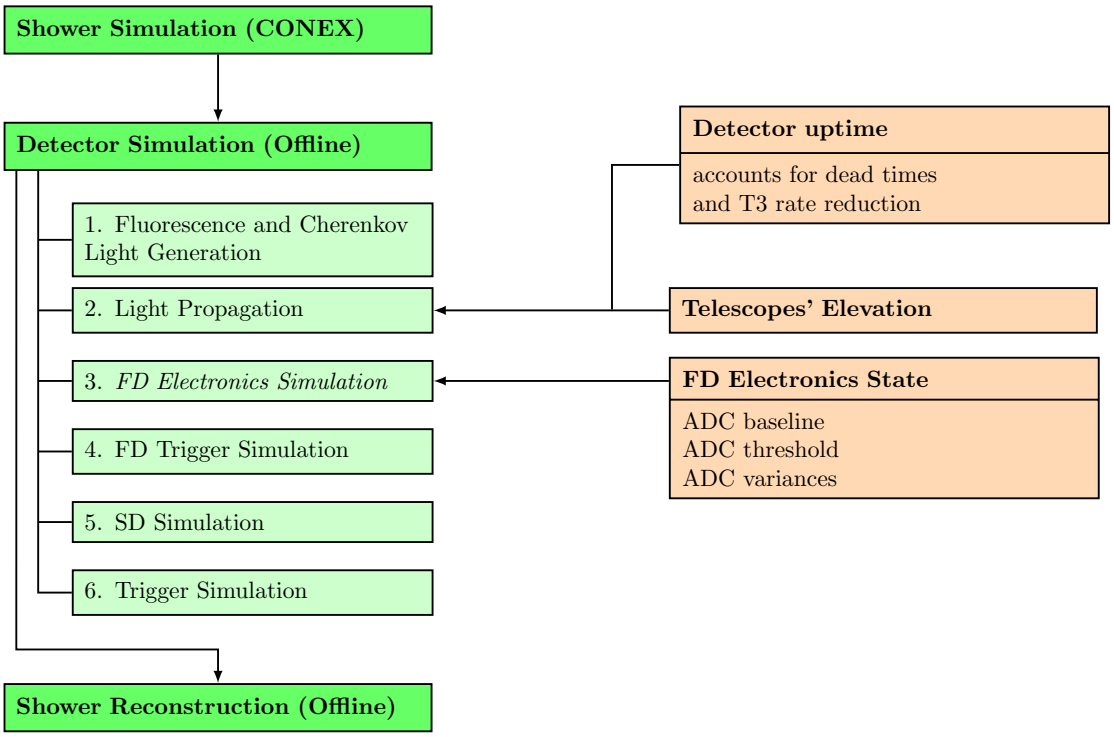

Figure 5.1.: Auger static and RealMC simulation sequence. On the left the standard Auger simulation sequence consisting of shower simulation, detector simulation and finally shower reconstruction is shown. The detector simulation is splitted up into the different subtasks. On the right the additional input used for RealMC is shown. The arrows between the right and left side mark where the information is used in the detector simulation.

5.3. Comparison Between Dynamic and Static MC

Before determining the detector resolution and bias, the effect of the RealMC, which uses the FD electronics monitoring and uptime data but does not include the information from atmospheric monitoring, compared to the regular static Monte Carlo is checked. Therefore, this section shows a comparison between the dynamic RealMC and the static detector simulation by using the observables energy and $X_{\max}$.

5.3.1. Air Shower Simulation

For a comparison it is not a viable option to just redo the simulation of the detector response without including the monitoring data because the simulation is very time consuming. Therefore, it is necessary to use a representative set of air showers. This is achieved by using the geometrical reconstruction of observed showers. For this purpose the geometrical and timing information from a subset of reconstructed CoHe showers[2] is used, because those are supposed to have a reasonable data quality, are distributed in the geometrical range of the detector and hence should lead to a high success rate in simulation.

The necessary shower parameters are extracted by a small `C++` program written by myself, which extracts observed

- time stamp,
- energy,
- $X_{\max}$,
- zenith angle,
- azimuth angle,
- core position and
- event ID.

These quantities are extracted into a ROOT-file for later use in the $\overline{\text{Off}}\underline{\text{line}}$ and as a steering card for 5172 CONEX showers. The shower simulation is performed with the hadronic interaction model EPOS [37] for proton primaries. Only this interaction model is chosen to reduce the needed CPU time. Also the chosen model is not supposed to have an impact on the results, because the final simulation output is not compared to real data but to the same shower just run through different kinds of detector simulations.

5.3.2. Detector Simulation and Shower Reconstruction

The performed detector simulation differs from a standard Auger simulation by splitting the detector simulation into two parts: the light simulation and the electronics simulation. A common light simulation (light generation in the atmosphere and light propagation up to the single camera pixels) for RealMC and standard MC is done and the results are stored. Based on the stored results from the common light simulation, the standard MC electronics simulation as well as the RealMC

[2] Those passing the cuts described in cf. sec. 6.1

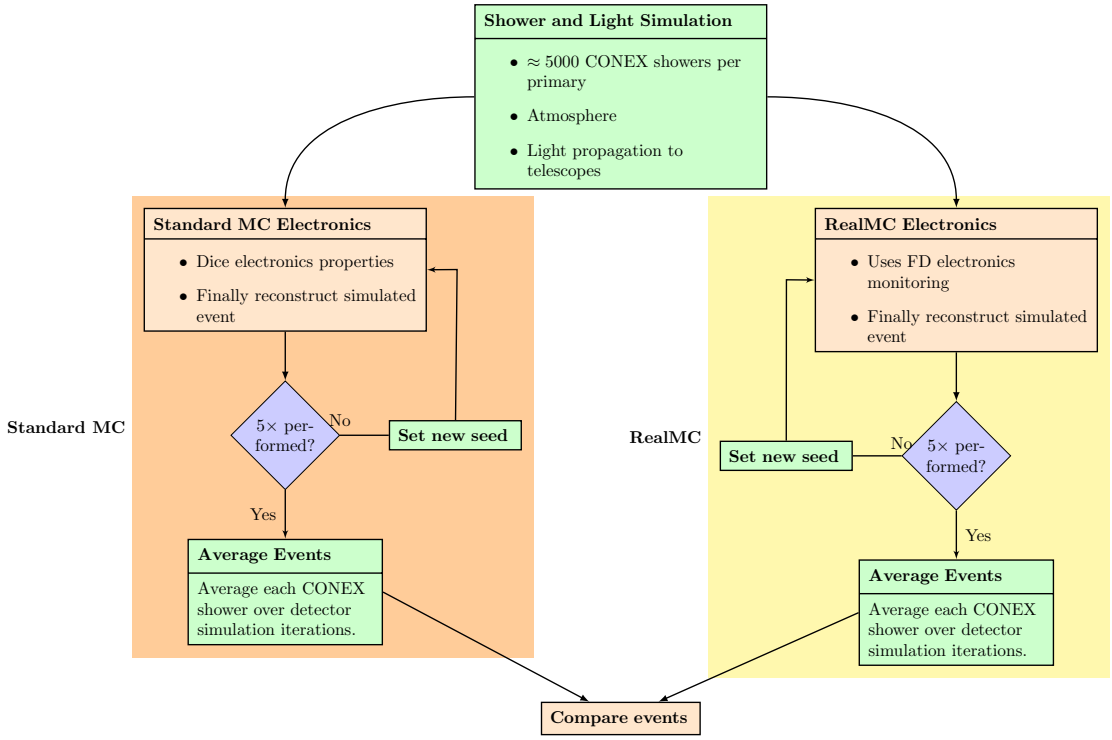

Figure 5.2.: Workflow for comparison between static and RealMC. The light generation and propagation for each shower is performed once and then used for standard MC as well as RealMC. The only difference between both detector simulation branches is the use of monitoring data.

electronics simulation are done. This assures that differences between the static and dynamic Monte Carlo arise only from different electronics simulations. Afterwards, the standard HEAT data reconstruction is done. For each kind of detector electronics simulation two runs with different random number generator seeds are done. Finally, the simulations are compared event wise. The whole workflow is shown in fig. 5.2.

To initialize the internal Offline data structures with the previously exported shower parameters, a new Offline module, the `EventGeneratorAC`, was written by myself. The values initialized by this module are the event ID, the time stamp and the core position. The event ID and the timestamp allow to match showers for comparison. Zenith angle and primary energy are properties of each CONEX shower.

5.3.3. Analysis

Besides well reconstructed events, even poorly reconstructed events, e.g. showers with a too short observed track, survive the simulation and reconstruction chain. Therefore, it is necessary to apply soft cuts, which are sufficiently soft such that good events are passing with high efficiency. These are

- event has to be a hybrid event,
- relative energy error below 100 %,
- Cherenkov fraction below 100 %,
- zenith angle between 0° and 90° (no up going events),

- the Gaisser-Hillas fit on the energy deposit profile should be better than the fit of a line.

Finally, each event simulated in the time dependent detector simulation is compared to its counterpart from the time independent simulation. Associated events are matched by unique timestamps and the event ID. The property $\Delta Y/Y_{\text{time indep.}}$ with the difference $\Delta Y = Y_{\text{time indep.}} - Y_{\text{time dep.}}$ between both simulation methods is used for the comparison of the observed quantity Y. As in the mass composition analysis the energy and the $X_{\max}$ are important observables, these are the used observables for the simulation comparison, too. The results of the comparison are shown in fig. 5.3.

To interpret the derived mean (eqn. 5.2 on p. 48) and RMS (eqn. 5.3 on p. 48) of the distributions from the comparison, the same comparison is performed between the two simulations done with the static electronics simulation as well as between the two simulations done with the dynamic electronics simulation, too. The derived values for mean and RMS are shown in tab. 5.1 and the figures 5.4 and 5.5. For the comparison between equal kinds of electronics simulations it is evident that the mean for both quantities is compatible with zero within at least 1.3σ. The RMS values also fit well within overlapping 2σ intervals.

The mean relative energy difference for the comparison between the dynamic and static electronics simulation is only in 3σ compatible with zero. This is similar for the mean of the relative $X_{\max}$ difference (within 2σ compatible with zero). The absolute values of both means are higher than for those derived from the comparison between equal simulation kinds. The RMS of the energy and $X_{\max}$ relative differences between the dynamic and static electronics simulation are similar to those derived from the comparison between equal simulation kinds.

Finally, small differences between the reconstructed energy of about 0.5 % and 0.17 % for the reconstructed $X_{\max}$ are mentionable between the dynamic and static electronics simulations. For example these differences are very small compared to the energy resolution of about 10 % of the detector (see following sections).

	$\Delta E/E \cdot 10^2$		$\Delta X_{max}/X_{max} \cdot 10^2$	
	Mean	**RMS**	**Mean**	**RMS**
static vs. static	-0.2 ± 0.2	8.3 ± 0.2	-0.04 ± 0.07	2.92 ± 0.05
dynamic vs. dynamic	-0.4 ± 0.3	7.9 ± 0.2	-0.03 ± 0.09	2.72 ± 0.06
dynamic vs. static	-0.6 ± 0.2	7.9 ± 0.2	-0.17 ± 0.08	2.80 ± 0.06

Table 5.1.: Results from the comparison of the different kinds of electronics simulations.

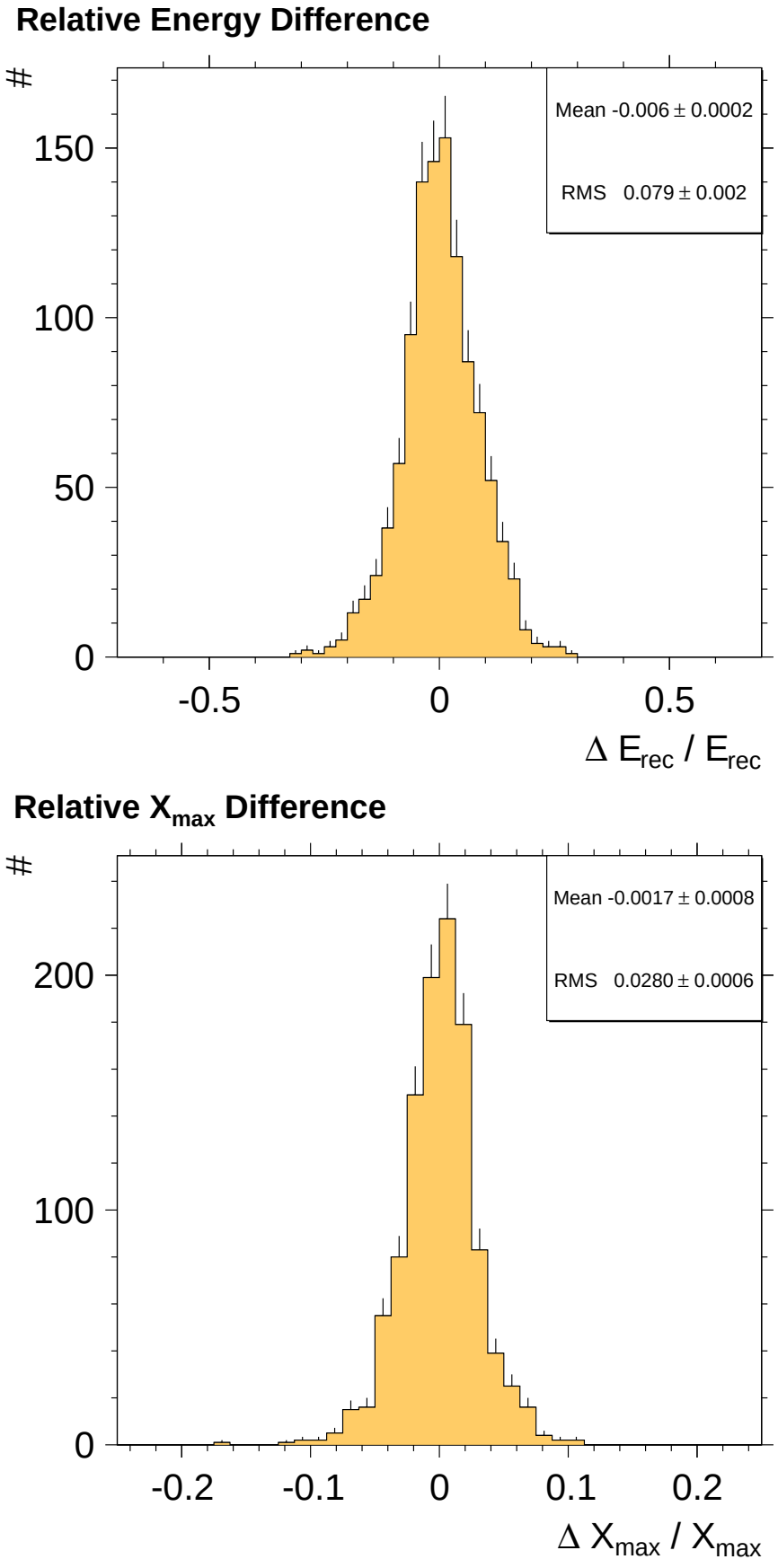

Figure 5.3.: Relative difference between the reconstructed quantities of a dynamic and static simulation of the detector. It is $\Delta Y = (Y_{\text{time indep.}} - Y_{\text{time dep.}})$ with Y denoting the shown quantity.

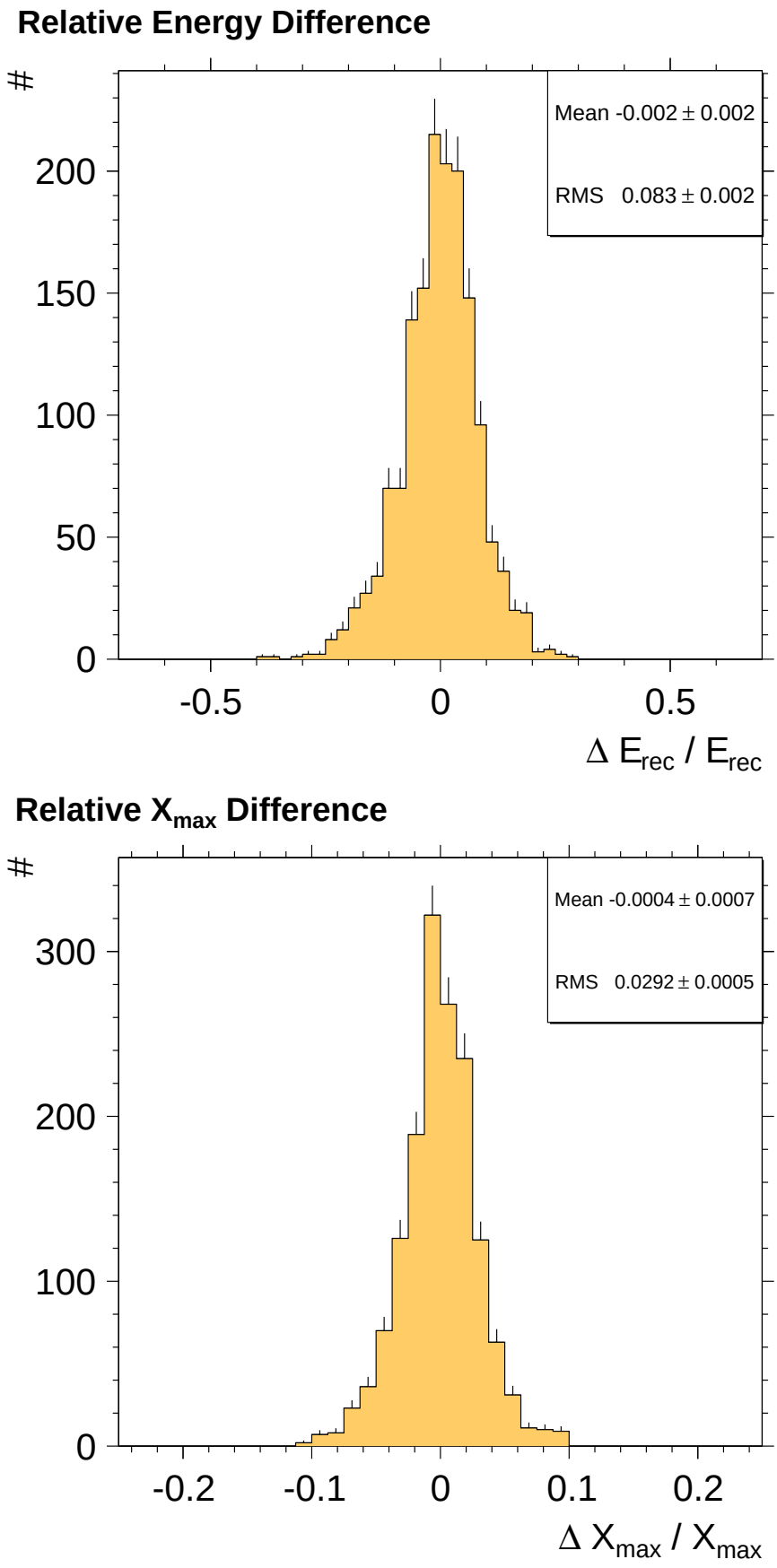

Figure 5.4.: Distributions of energy and $X_{\max}$ differences between two static Monte Carlo runs with different random number generator seeds.

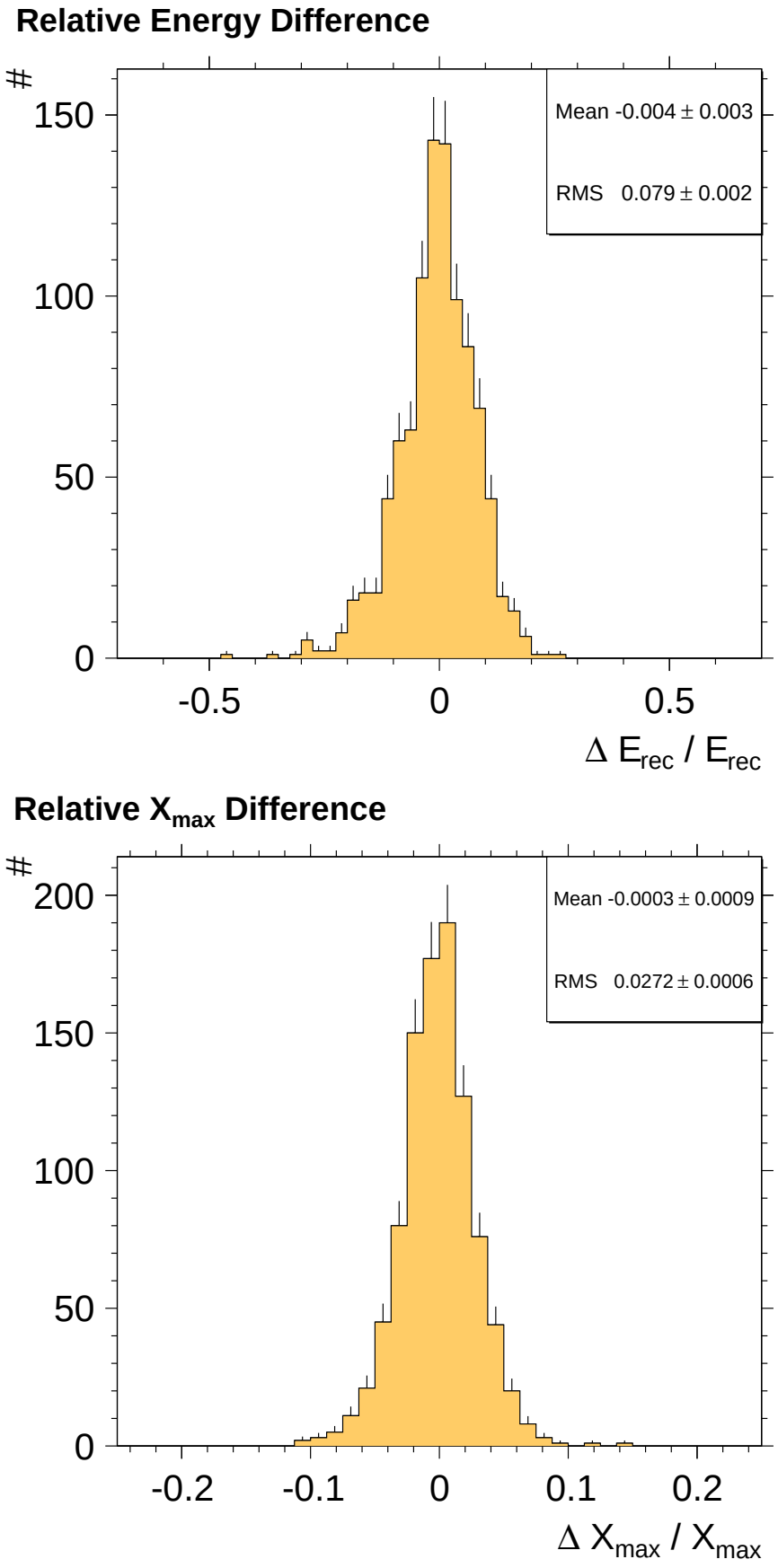

Figure 5.5.: Distributions of energy and $X_{\max}$ differences between two dynamic Monte Carlo runs with different random number generator seeds.

5.4. Detector Response

In this section two effects, the detector resolution and the reconstruction bias, are determined from Monte Carlo simulations in the energy range of HEAT from $10^{17}\,\mathrm{eV}$ to $10^{18.5}\,\mathrm{eV}$. The detector resolution states how good a quantity can be measured with the detector. The reconstruction bias indicates how much a reconstructed property is systematically shifted. These properties can be obtained from a simulation of the detector where the exact and the reconstructed values are known.

5.4.1. Definition of Investigated Effects

In the following $\mathbf{Y}$ is a vector with N components Y_i representing all N measurements of the quantity Y. $\mathbf{Y}_{\mathrm{MC}}$ names the true values and $\mathbf{Y}_{\mathrm{rec}}$ the values reconstructed from the observation of $\mathbf{Y}_{\mathrm{MC}}$. For mass composition studies with fluorescence detectors, one is interested in the quantities energy E, depth of the shower maximum $X_{\max}$ and $\mathrm{RMS}(X_{\max})$.

The reconstruction bias can be defined as the difference between the true and the reconstructed value

$$\mathrm{BIAS}(Y) = \langle \mathbf{Y}_{\mathrm{rec}} - \mathbf{Y}_{\mathrm{MC}} \rangle \quad , \tag{5.1}$$

where $\langle \mathbf{Y} \rangle$ denotes the unbiased sample mean over

$$\langle \mathbf{Y} \rangle = \frac{1}{N} \sum_{i=1}^{N} y_i \quad . \tag{5.2}$$

The detector resolution can be estimated from the RMS of the distribution of $\mathbf{Y}_{\mathrm{rec}} - \mathbf{Y}_{\mathrm{MC}}$. The RMS is defined as

$$\mathrm{RMS}(Y) = \sigma(Y) = \sqrt{\frac{1}{N-1} \sum_{i=1}^{N} (y_i - \langle \mathbf{Y} \rangle)^2} \quad , \tag{5.3}$$

which in fact is the unbiased squared sample mean variance. The variance of the RMS is (cf. [74])

$$V\,(\mathrm{RMS}) = \sqrt{\frac{1}{N} \left(m_4 - \frac{N-3}{N-1} \sigma^4\,(Y) \right)} \quad , \tag{5.4}$$

with $\sigma\,(Y)$ the estimator of the true $\mathrm{RMS}(Y)$. Actually $\sigma(Y)$ should be the true value of $\mathrm{RMS}(Y)$, however, the true value is not known. Additionally, $m_4(Y)$ is the 4th central moment

$$m_4\,(Y) = \frac{1}{N} \sum_{i=1}^{N} \left(y_i - \langle \mathbf{Y} \rangle \right)^4 \quad . \tag{5.5}$$

5.4.2. Event Statistics of RealMC

To obtain the detector resolution and reconstruction bias for the events used in the analysis, it is necessary to apply the same cuts (described in sec. 6.1) to the simulated events as to the data. The number of events before and after applying

Primary	Criteria	EPOS	QGSJetII	Sibyll 2.1	Sum
Proton	w/o cuts	488,000	448,000	450,000	1,386,000
	FD triggered	93,805	85,260	87,174	266,239
	with cuts	32,874	28,911	29,916	91,701
Iron	w/o cuts	445,000	447,000	446,000	1,338,000
	FD triggered	72,483	77,181	77669	227,333
	with cuts	26,956	28,753	28,949	84,658

Table 5.2.: Number of simulated events, number of events with FD trigger and number of events after applying cuts (cf. sec. 6.1).

these cuts to the simulation output is shown in tab. 5.2. The differences between the total count of used showers for the detector simulation arises from detector simulations which keep terminating due to problems in the simulation. After three retries, the problematic shower files have been dropped. This problem just occurred for a few shower files containing showers with primary energies of about 10^{18} eV. Each of the misbehaving shower files contains 1000 CONEX extensive air shower simulations. It is not expected that these missing showers induce a bias to the analysis because the physical properties of the showers in each shower file are uniformly distributed.

Tab. 5.3 shows the number of showers after applying cuts, partitioned into hadronic interaction model, primary and energy bin. Especially the low number of showers surviving the cuts at the lowest energy bin is noticeable. This does not cohere with the aforementioned problem of unsuccessful detector simulations. However, it is caused by the decreasing hybrid trigger efficiency of the SD with decreasing energy of the primary (cf. 6.1).

5.4.3. Detector Resolution

The interesting observables for a mass composition analysis with a fluorescence detector are the energy E, $\langle X_{\max} \rangle$, and the RMS($X_{\max}$) (cf. sec. 2.3.2). The numerical results of the determined detector resolutions are given in sec. E.2 p. 118.

Energy bin / eV	Sibyll		QGSJetII		EPOS	
	Proton	Iron	Proton	Iron	Proton	Iron
$10^{17.0}$	740	280	705	292	681	208
$10^{17.25}$	2534	1229	2694	1714	2623	986
$10^{17.5}$	1238	937	1299	744	1050	795
$10^{17.75}$	3511	3209	3279	2932	3009	2959
$10^{18.0}$	6252	5809	5541	6065	10508	5588
$10^{18.25}$	7433	7955	7208	8035	7321	7918
$10^{18.5}$	8208	9530	8185	8971	7682	8502

Table 5.3.: Number of simulated events per primary and energy bin after applying cuts.

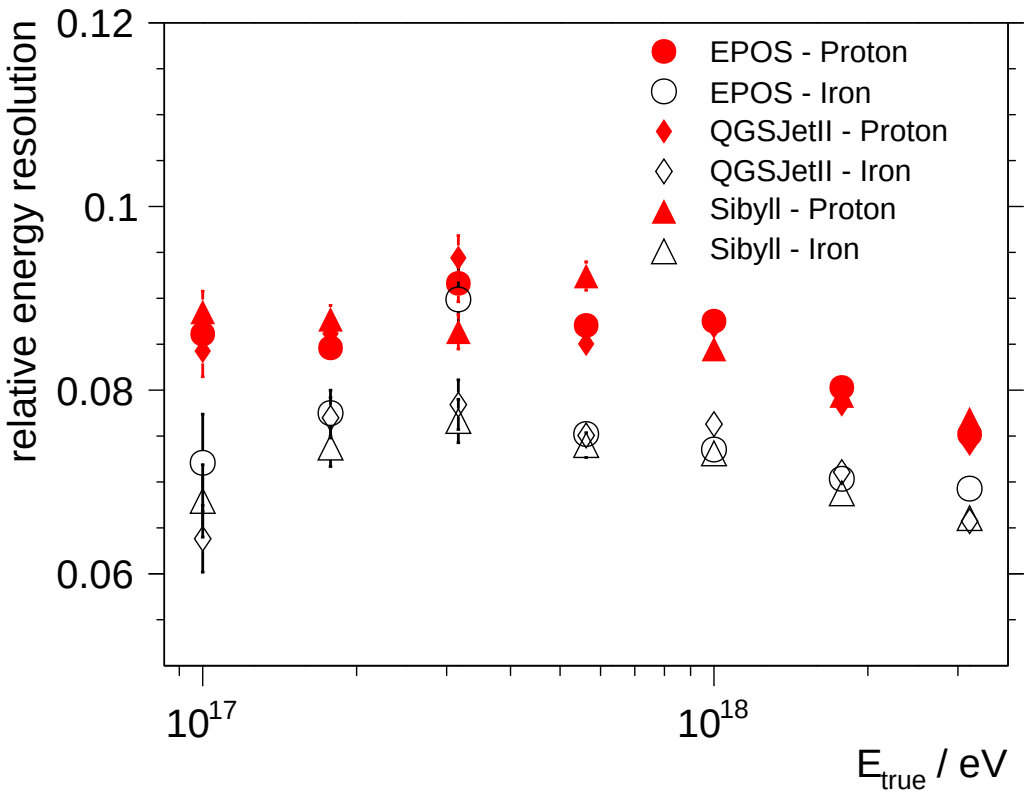

Figure 5.6.: Energy resolution of the detector as a function of energy. ♦ denotes QGSJetII, • denotes EPOS and ▲ denotes Sibyll simulations. Red, filled markers denote proton primaries, and black, open markers denote iron primaries.

Energy Resolution The determined energy resolution is shown in fig. 5.6. The overall energy resolution is better than 10 %. Over the whole energy range from 10^{17} eV up to $10^{18.5}$ eV the energy resolution is better for iron primaries than for proton primaries. The differences between the primaries are about 0.02. The used hadronic interaction models agree well for each primary (at least within overlapping 2σ).

$\langle X_{max} \rangle$ Resolution The evolution of the detector resolution of $X_{\max}$ is shown in fig. 5.7a. For all used primaries and hadronic interaction models the derived detector resolution of the $X_{\max}$ is better than $30\,\mathrm{g\,cm^{-2}}$. With increasing energy the $X_{\max}$ resolution gets better from about $29\,\mathrm{gm\,cm^{-2}}$ at 10^{17} eV to about $20\,\mathrm{g\,cm^{-2}}$ at $10^{18.5}$ eV. Putting the focus on the highest energy bin, one sees that the combined HEAT-Coihueco $X_{\max}$ resolution is compatible with the one earlier derived and published for the regular FD[75] of about $25\,\mathrm{g\,cm^{-2}}$.

RMS(X_{max}) Resolution The resolution of the RMS($X_{\max}$) as a function of energy is shown in fig. 5.7b. To determine the statistical uncertainty of RMS($X_{\max}$), the variation of the value between subsamples containing ten events is determined. Like the $\langle X_{\max} \rangle$ resolution, the RMS($X_{\max}$) resolution gets better with increasing energy. The resolution is between $1.3\,\mathrm{g\,cm^{-2}}$ at 10^{17} eV and $0.5\,\mathrm{g\,cm^{-2}}$ at $10^{18.5}$ eV.

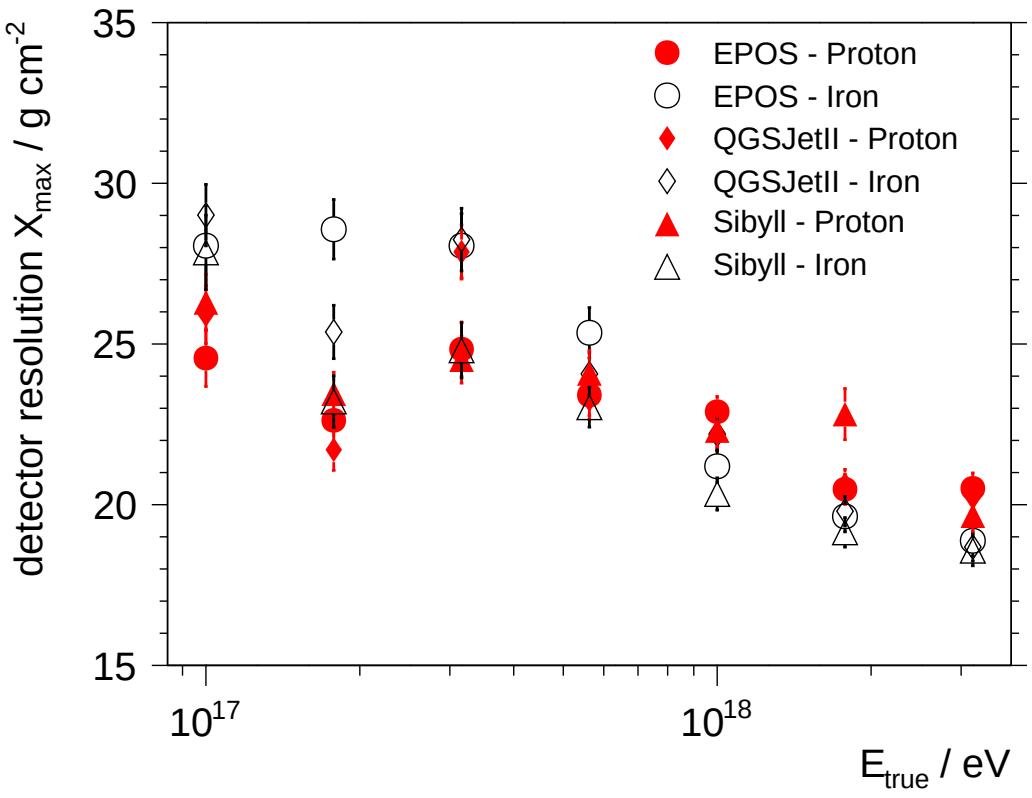

(a) $X_{\max}$ resolution of HEAT and Coihueco.

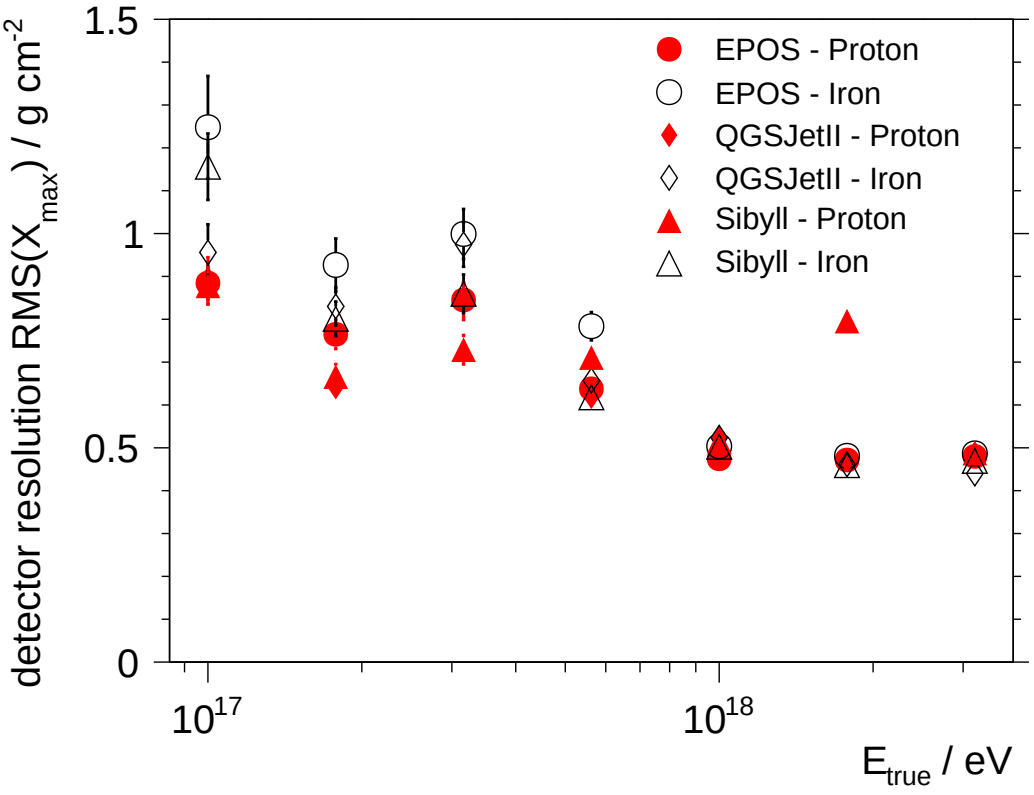

(b) RMS($X_{\max}$) resolution of HEAT and Coihueco.

Figure 5.7.: $X_{\max}$ and RMS($X_{\max}$) resolution of the detector as a function of energy. ♦ denotes QGSJetII, • denotes EPOS and ▲ denotes Sibyll simulations. Red, filled markers denote proton primaries, and black, open markers denote iron primaries.

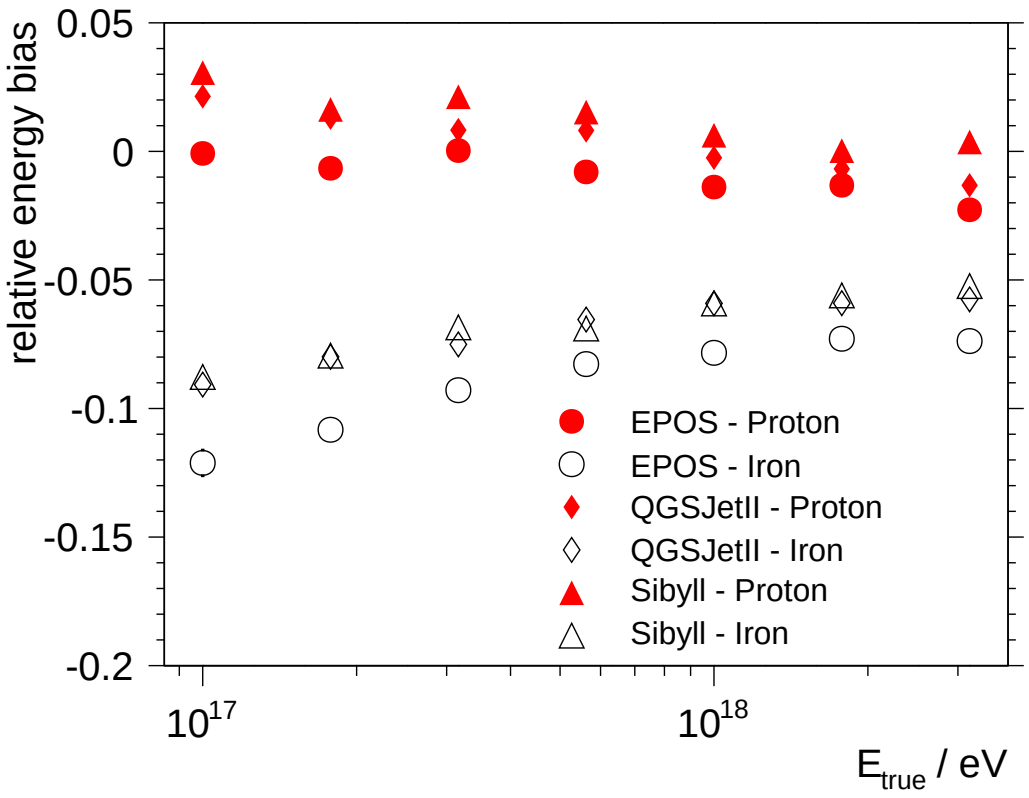

Figure 5.8.: Energy reconstruction bias as a function of energy. ♦ denotes QGSJetII, • denotes EPOS and ▲ denotes Sibyll simulations. Red, filled markers denote proton primaries, and black, open markers denote iron primaries.

5.4.4. Reconstruction Bias

Besides the detector resolution, also the reconstruction bias of both primaries is of great interest. The numerical values for the reconstruction bias separated by energy, primary and hadronic interaction model are given in the appendix E.3 p. 119.

Energy Reconstruction Bias As explained in sec. 3.3 the FD measures the calorimetric energy. However, the calorimetric energy differs from the primaries energy because not every part of the shower development is visible to the FD. As stated before in sec. 2.3.2, the hadronic interactions in a shower are subject to statistical fluctuations, which decrease with increasing primary mass. Depending on the statistical fluctuations in the early shower development and considering the high fraction of energy each secondary particle has at this stage, the amount of energy transferred to particles *invisible* to the detector like neutrinos and muons is strongly influenced by these statistical fluctuations in the first few interactions. Therefore, it can be expected that the calorimetric measurement is affected, too.

Fig. 5.8 shows the energy bias determined from Monte Carlo simulations. A strong primary dependence on the kind of primary is evident. For proton primaries the energy bias is nearly constant (between ± 0.02) over the whole energy range. The determined energy bias for the iron primaries gets better with increasing energy. However, in the considered energy range it does never match the energy bias determined for protons. The energy bias determined for iron primaries with

the EPOS hadronic interaction model show the worst value at all energies (about 0.02 worse than the other models). For the proton primaries the EPOS model has the lowest energy bias, too.

$\langle X_{max} \rangle$ Reconstruction Bias In fig. 5.9a the $X_{\max}$ bias is shown. The $X_{\max}$ bias evolves from about $5\,\mathrm{g\,cm^{-2}}$ for iron primaries and $-5\,\mathrm{g\,cm^{-2}}$ for proton primaries at $10^{17}\,\mathrm{eV}$ to about $-7\,\mathrm{g\,cm^{-2}}$ for both primaries at $10^{18.5}\,\mathrm{eV}$. The reconstruction bias of the $X_{\max}$ is slightly different between showers induced by proton and iron primaries. For proton induced showers the bias value is a few $\mathrm{g\,cm^{-2}}$ smaller. With increasing energy the differences between both primaries gets smaller.

RMS(X_{max}) Reconstruction Bias The RMS($X_{\max}$) (cf. fig. 5.9b) bias is rather constant over the whole considered energy range at about $8\,\mathrm{g\,cm^{-2}}$. As for the $X_{\max}$ bias the deduced proton value is about a few $\mathrm{g\,cm^{-2}}$ smaller and the difference between both primaries reduces with increasing energy.

5.5. Summary

In this chapter the simulations used for the analysis of the depth of the shower maximum has been presented.

It was shown that the energy resolution of the combined HEAT and Coihueco detector configuration is better than 10 % for proton and iron primaries. Besides, it was presented that the $X_{\max}$ resolution is better than $30\,\mathrm{g\,cm^{-2}}$ over the whole energy range and that the RMS resolution is better than $1.5\,\mathrm{g\,cm^{-2}}$.

Furthermore, it was demonstrated that the energy bias is strongly primary dependent (about 0 % for proton primaries and between -10 and -5 % for iron induced showers). It was presented that the $X_{\max}$ bias evolves from $5\,\mathrm{g\,cm^{-2}}$ at $10^{17}\,\mathrm{eV}$ to $-5\,\mathrm{g\,cm^{-2}}$ at $10^{18.5}\,\mathrm{g\,cm^{-2}}$. Besides, it was shown that the RMS($X_{\max}$) bias is rather constant at about $10\,\mathrm{g\,cm^{-2}}$.

In the next chapter the measured events will be corrected for the determined bias.

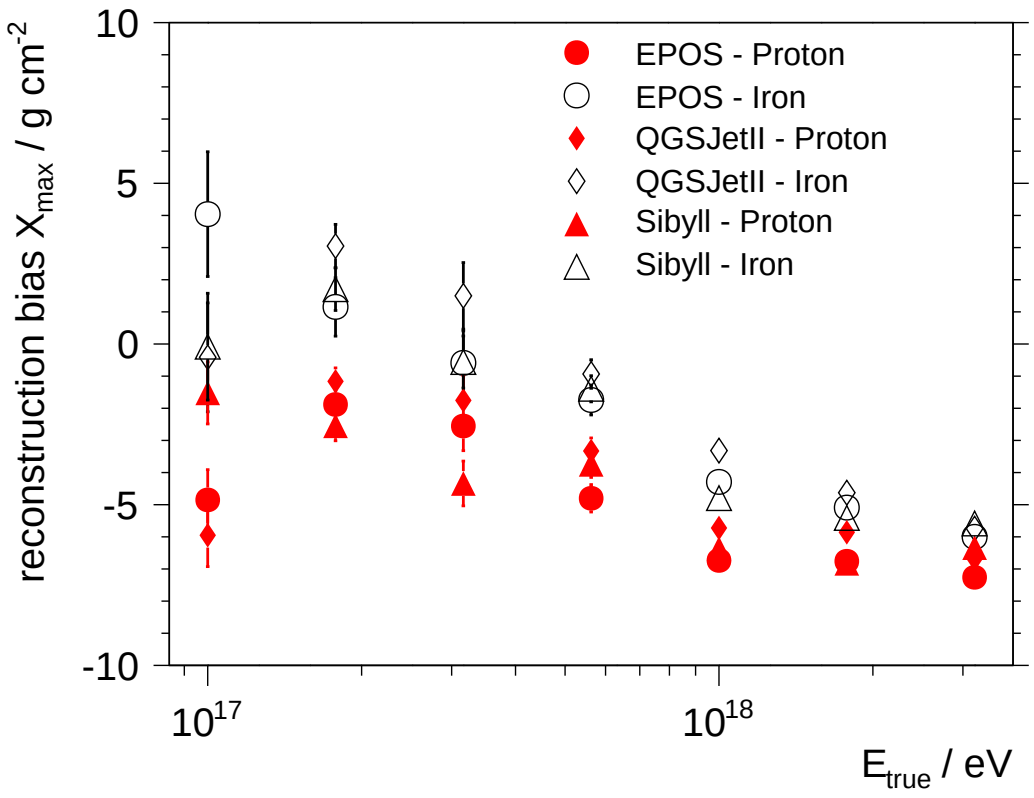

(a) $X_{\max}$ reconstruction bias for HEAT and Coihueco.

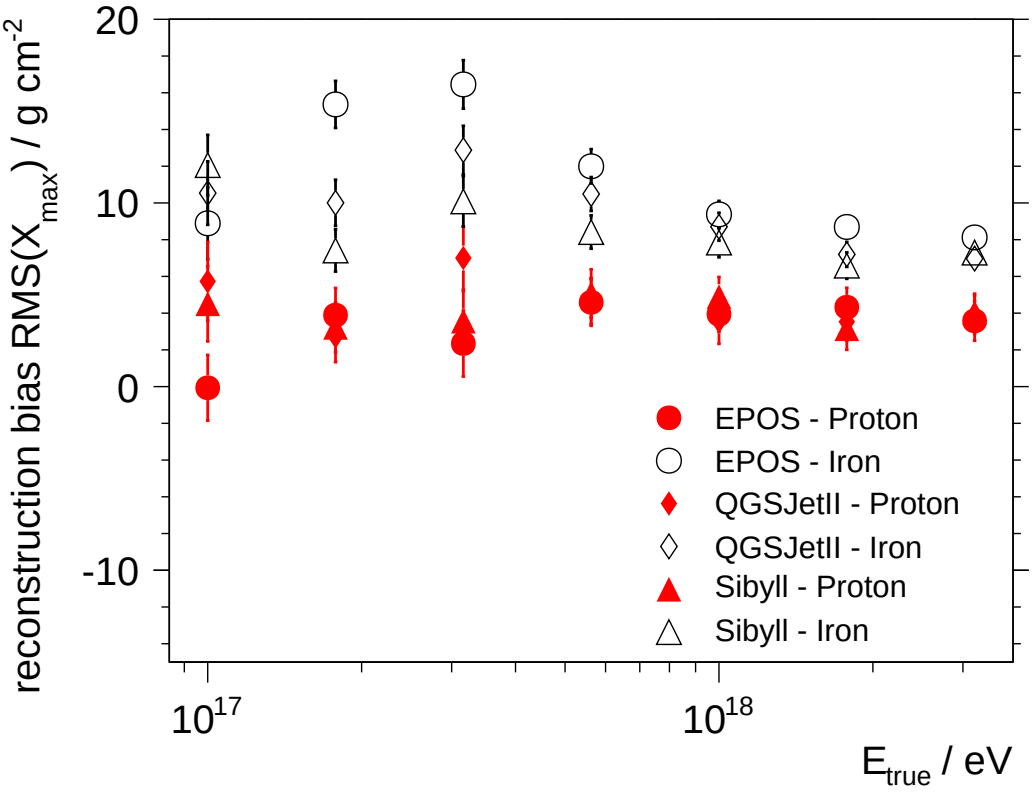

(b) RMS($X_{\max}$) reconstruction bias for HEAT and Coihueco.

Figure 5.9.: $X_{\max}$ and RMS($X_{\max}$) reconstruction bias as a function of energy. ♦ denotes QGSJetII, ● denotes EPOS and ▲ denotes Sibyll simulations. Red, filled markers denote proton primaries, and black, open markers denote iron primaries.

6. Determining the Depth of Shower Maximum

The analysis of the shower maximum is performed on a data sample taken from 2010/06/01 until 2011/05/30 with the Auger fluorescence detector sites HEAT and Coihueco as well as the Auger surface detector. The aim of the analysis is to finally compare the data with Monte Carlo produced showers initiated by proton and iron primaries to deduce the primaries initiating the extensive air showers observable at the ground level.

6.1. Data Selection

To determine the chemical composition of the primaries inducing the observed air showers, it is crucial to reduce the detection bias for different primaries and assure a good shower reconstruction. On the one hand, this is – in contrast to the standard Auger analysis – achieved at the raw data merging state (cf. sec. 4.2.1), because at the moment all necessary information is only available at this stage. On the other hand, event selection criteria are applied on the reconstructed events (cf. sec. 4.2). The cuts presented in this section are based on the suggestions from [56].

For this analysis only events recorded when HEAT was in the upward mode are used, which together with the correction for the T3 rate limiting (cf. sec. 4.2.1) assures a constant field of view. Furthermore, the reconstruction from the virtual combined *CoHe-Eye*[1] is used. For a better geometrical reconstruction, which leads to a better energy and $X_{\max}$ reconstruction (cf. [76]), it is required that only hybrid events are chosen. Additionally, events with saturated or bad pixels are rejected because the effects of pixels out of their operational range is hard to determine. Also reconstruction sanity checks are performed. So it is necessary, that the shower core is located in the SD array, that enough FD camera pixels are triggered for an axis reconstruction and that the reconstructed Cherenkov light fraction is at most 100 %.

In rough terms, the energy and $X_{\max}$ reconstruction is performed by fitting a Gaisser-Hillas function (cf. sec. 3.3 eqn. 3.5) on the energy deposit profile $\mathrm{d}E/\mathrm{d}X$. The $X_{\max}$ and the calorimetric energy of the shower are a result of this fit. The energy of the primary particle is determined after applying an invisible energy correction (cf. sec. 3.3). To gain good fit results, it is crucial to measure the rising and falling edge of the longitudinal profile. Therefore, only events with the $X_{\max}$ in the field of view are accepted. The energy and $X_{\max}$ resolution determined for events with $X_{\max}$ not in field of view is worse [77]. A further criterion concerning the Gaisser-Hillas fit is the requirement of a χ^2/N_{dof} smaller than 1.6. Fig. 6.1 confirms that this criterion is not too harsh. It is noticeable, that the distribution generated from reconstructed events is broader than the MC one, which can be

[1] Definition is given in sec. 4.2.

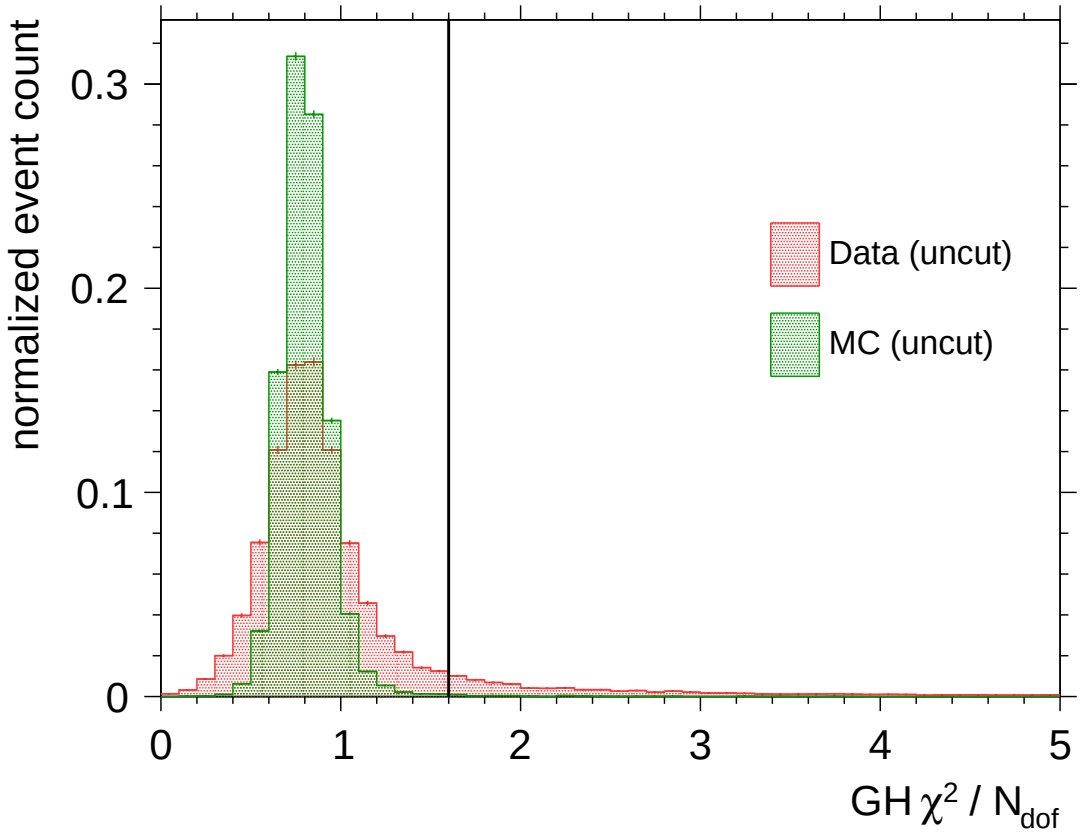

Figure 6.1.: Distribution of the reduced χ^2 of the Gaisser-Hillas fit. The red shaded distribution is derived from data (no cuts applied) and the green shaded distribution is derived from RealMC events (no cuts applied). The vertical black line marks the actually used cut value on this quantity.

qualitatively explained by missing detector effects in the simulation like the real atmospheric condition when the event is simulated. Due to the missing atmospheric monitoring data, atmospheric effects cannot be accounted for here.

The primaries are expected to have a mass between that of proton and iron, hence the $X_{\max}$ resolution and reconstruction bias determined from the simulations of proton and iron primaries are expected to be sufficient. Due to eqn. 2.8 the difference between proton and iron induced showers is about $150\,\mathrm{g\,cm^{-2}}$ [78]. Therefore, only events with a reconstruction uncertainty of at most $40\,\mathrm{g\,cm^{-2}}$ are accepted.

Furthermore, a maximal relative uncertainty on the determined energy of 20 % is required, which indicates reasonable fit results. This cut value is compatible with the detector resolution of about 10 % (cf. sec. 5.4.3). Fig. 6.2 shows that for MC and data most events meet this criterion.

Another cut concerns the minimum viewing angle of a shower. In [75] p. 27 it is shown, that for showers observed at viewing angles smaller than 20° the systematic effects on the reconstructed $X_{\max}$ increase rapidly. Therefore, just events with at least a minimum viewing angle of 20° are accepted.

For mirror-crossing events there exist non-instrumented spatial parts which lead to holes in the longitudinal shower profile. Besides, clouds in the field of view can lead to holes in the longitudinal profile, too. Because of the possible impact on

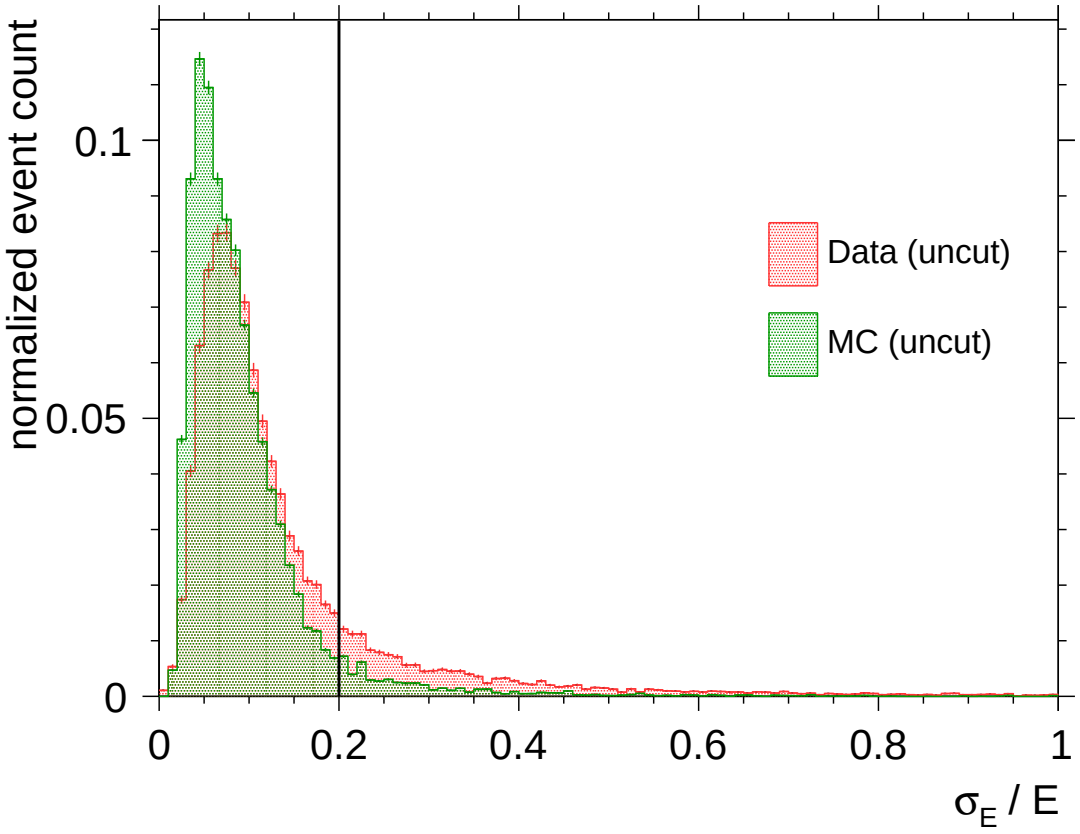

Figure 6.2.: Distribution of the relative energy uncertainty determined by reconstruction and RealMC. The red shaded distribution is derived from data (no cuts applied) and the green shaded distribution is derived from RealMC events (no cuts applied). The vertical black line marks the actually used cut value on this quantity.

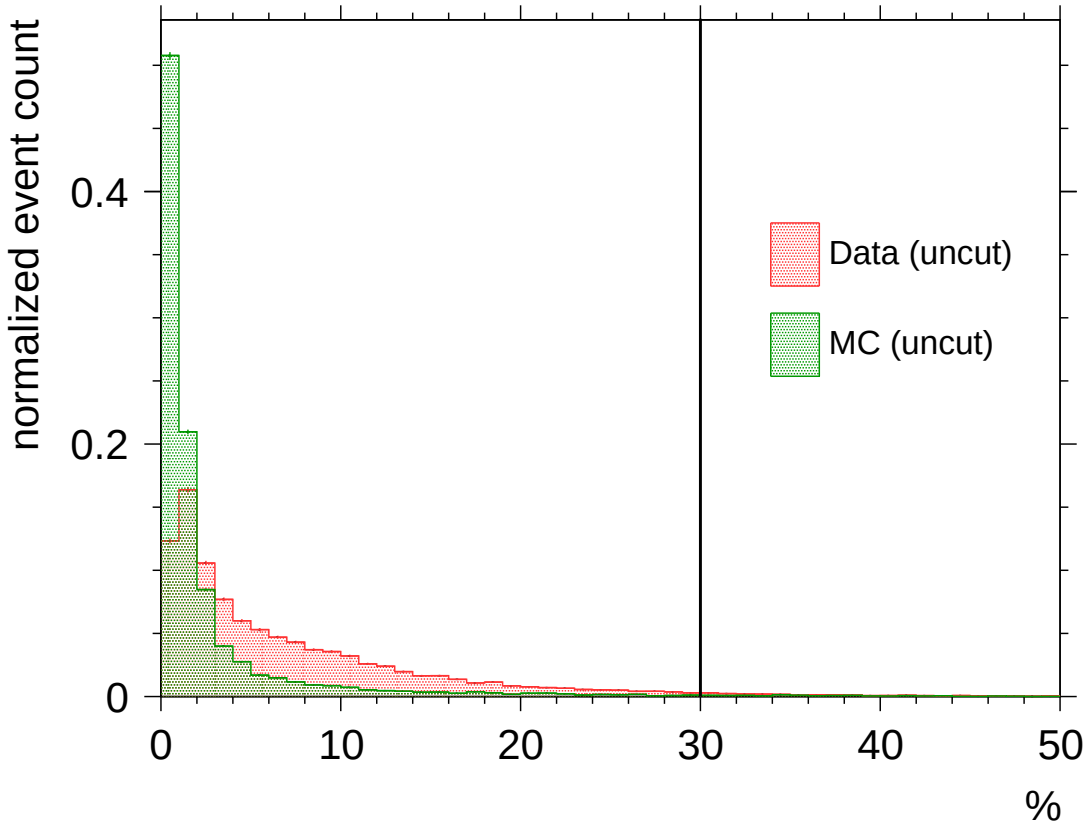

Figure 6.3.: Distribution of the biggest hole size in the shower profile. The red shaded distribution is derived from data (no cuts applied) and the green shaded distribution is derived from RealMC events (no cuts applied). The vertical black line marks the actually used cut value on this quantity.

the reconstruction, events with a gap larger than 30 % are rejected. According to fig. 6.3, this cut just removes single events. As for the other quantities, the distribution generated from observed showers is broader than the MC one, which can be qualitatively explained by missing detector effects in the simulation like the real atmospheric condition when the event is simulated. Due to the missing atmospheric monitoring data, atmospheric effects cannot be accounted for here.

The previously mentioned hybrid selection criteria induces a bias because the trigger probability of the surface detector depends on the shower energy, the primary, the shower's core position and inclination of the shower axis. For events above 10^{18} eV, just like for regular FD events, the trigger probability is close to one if the shower core is inside the array.

At lower energies the SD trigger probability drops rapidly (cf. fig. 6.4) and only in small areas around the SD stations the trigger probability is close to one for all primaries. A possibility to use only showers with a small hybrid trigger bias would be to introduce energy-dependent fiducial volumes for each station. However, a parametrization of the station trigger probability depending on the shower's zenith angle, reconstructed energy and core position was developed in [79]. Since this parametrization only accounts for the characteristics of a single SD station, it is also independent of the FD properties and therefore, can be used for an analysis of HEAT data, too. This parametrization is determined for iron

Cut	**Passed events**		**Cumulated**
	absolute	relative	
All Data	499064	100 %	100 %
HEAT upward orientation	369966	74.13 %	74.13 %
Only virtual CoHe eye	243699	65.87 %	48.83 %
Shower core in SD array	43385	17.80 %	8.69 %
Minimum 5 pixels for shower axis fit	38729	89.27 %	7.76 %
Cherenkov fraction $\leq 100\,\%$	31141	80.41 %	6.24 %
$E_{\mathrm{FD}} \geq 10^{16}\,\mathrm{eV}$	26012	83.53 %	5.21 %
is hybrid event	25889	99.53 %	5.19 %
X_{max} in FoV	17932	69.26 %	3.59 %
$\sigma(X_{\mathrm{max}}) \leq 40\,\mathrm{g\,cm^{-2}}$	12708	70.87 %	2.55 %
$\sigma(E)/E \leq 20\,\%$	12633	99.41 %	2.53 %
GH $\chi^2/N_{\mathrm{dof}} \leq 1.6$	12072	95.56 %	2.42 %
minimum viewing angle $\geq 20°$	9207	76.27 %	1.84 %
max. hole in depth profile $< 30\,\%$	9023	98.00 %	1.81 %
max. FD zenith angle $\leq 60°$	8920	98.86 %	1.79 %
brass hybrid trigger probability	7041	78.93 %	1.41 %
skip saturated pixels	7041	100.00 %	1.41 %
skip bad pixels	7041	100.00 %	1.41 %

Table 6.1.: Cuts applied on reconstructed extensive air shower events including the event selection efficiency.

and proton primary energies from $10^{17}\,\mathrm{eV}$ to $10^{18}\,\mathrm{eV}$ with zenith angles up to 60°. Therefore, events with a zenith angle above 60° are rejected. According to tab. 6.1 the cut on the FD zenith angle reduces the number of events by about 1 %.

The parametrization of the trigger probability of the surface detector is available as a `C++` class in the Offline analysis package. It provides the ability to determine the trigger probability for each triggered SD station. The shower-inducing primary is not known and therefore, the trigger probability is calculated for both available primary parametrizations. To reduce the bias, the calculated probabilities are not allowed to differ by more than 5 % and both must be above 90 %. These values are chosen due to the uncertainties on the parametrization.

Before applying the previously discussed cuts on the data set, there are 243699 events in the virtual eye, which combines the information from HEAT and Coihueco. After applying the cuts 7041 events remain for analysis. In tab. 6.1 the cut efficiencies are shown.

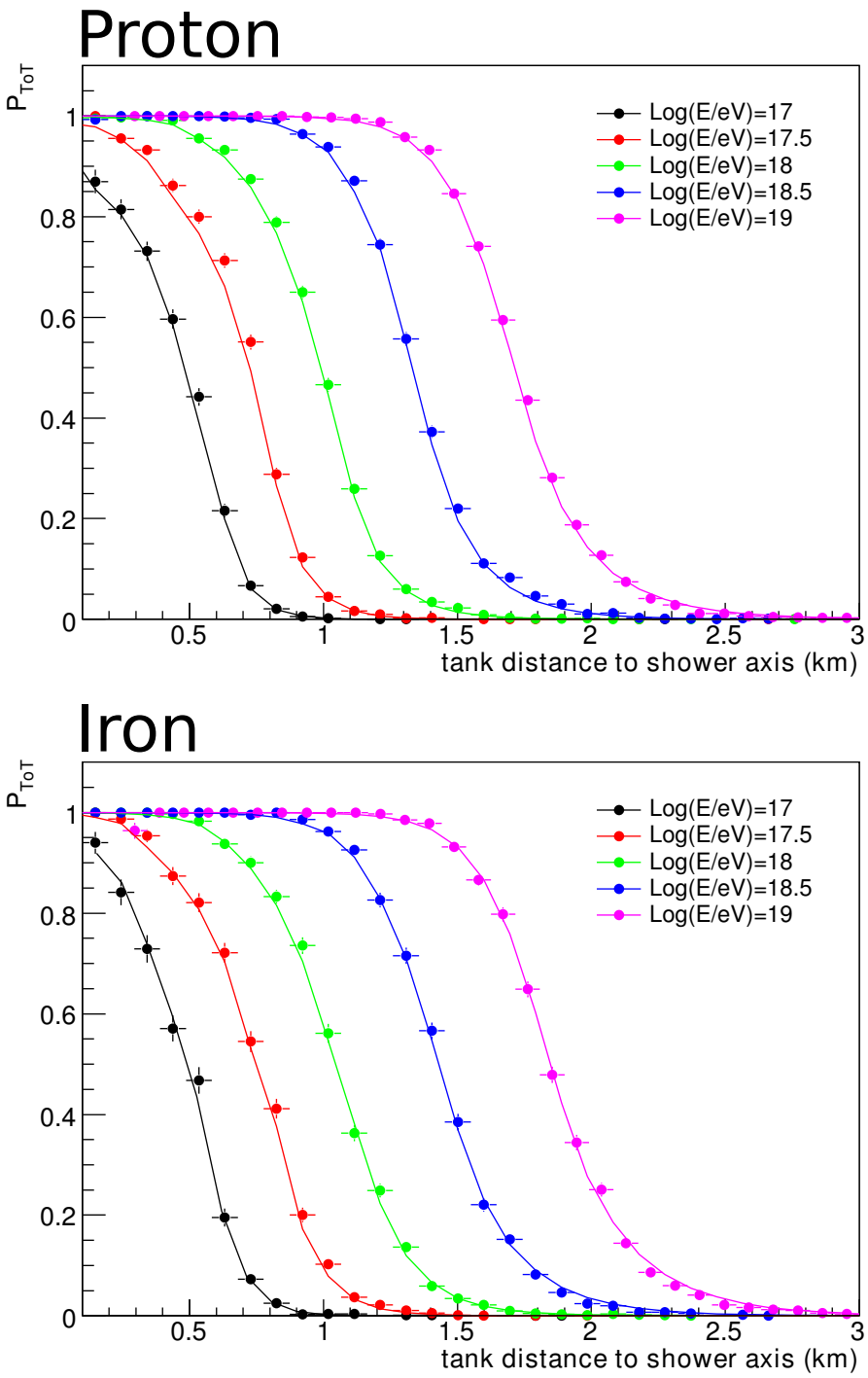

Figure 6.4.: Probability to trigger a surface detector station for proton (top) and iron (bottom) primaries as a function of energy and the distance of the shower core on the bottom to the SD station. The markers represents the probabilities derived from Monte Carlo studies and the lines denote derived parametrization used in this analysis. From [79].

6.2. Data Set

The selected data sample is binned in the energy range from 10^{17} eV to $10^{18.5}$ eV with the same binning used in sec. 5.4.4 (cf. table 6.2). The distribution of the primary mass sensitive parameter $X_{\max}$ per energy bin is shown in fig. 6.5. With increasing energy, the mean $X_{\max}$ (further on denoted by $\langle X_{\max} \rangle$) increases and the fluctuation measured by the RMS tends to decrease.

The sample mean $\langle X_{\max} \rangle$ and the corresponding sample mean uncertainty $\sigma\left(\langle X_{\max} \rangle\right)$ for each energy bin are calculated by using an equally weighted mean over all N measured values $X_{\max,i}$ in this energy bin

$$\langle X_{\max} \rangle = \frac{1}{N} \sum_{i=1}^{N} X_{\max,i} \ , \quad \sigma\left(\langle X_{\max} \rangle\right) = \sqrt{\frac{\sum_{i=1}^{N} \left(X_{\max,i} - \langle X_{\max} \rangle\right)^2}{N(N-1)}} \quad . \tag{6.1}$$

The RMS($X_{\max}$) and its uncertainty are given in eqn. 5.3 and eqn. 5.4 on p. 48.

Fig. 6.6a shows the uncorrected $\langle X_{\max} \rangle$ over energy. Due to the good statistics in all energy bins, besides the highest at $10^{18.5}$ eV, the statistical uncertainties on $\langle X_{\max} \rangle$ are rather small. The data can be described well by

$$Y(\langle E \rangle) = m \cdot \log_{10}(\langle E \rangle \, / \mathrm{eV}) + b \tag{6.2}$$

with Y denoting the fitted quantity, which is the $\langle X_{\max} \rangle$ in this case. By using the χ^2 minimization method, one gets a χ^2/N_{dof} of 2 with a probability $P(\chi^2/N_{\mathrm{dof}}) = 0.1$. The results for the parameters are $m = (49 \pm 2)\,\mathrm{g\,cm^{-2}}$ and $b = (-17 \pm 4) \cdot 10\,\mathrm{g\,cm^{-2}}$.

Fig. 6.6b shows the uncorrected RMS($X_{\max}$) over energy. As one can expect, the statistical uncertainties on the RMS are highest for the lowest and highest bins due to the low statistic in these bins. Besides the highest energy bin at $10^{18.5}$ eV the RMS decreases with increasing energy. The fit of a eqn. 6.2 results in a $\chi^2/N_{\mathrm{dof}} = 0.9$ with $P(\chi^2/N_{\mathrm{dof}}) = 0.5$. This indicates a good fit of the function to the measured data. The fitted parameters are $m = (-6 \pm 2)\,\mathrm{g\,cm^{-2}}$ and $b = (17 \pm 3) \cdot 10\,\mathrm{g\,cm^{-2}}$.

Energy / eV	**Bin Centre / eV**	**# events**	$\langle \mathbf{X_{max}} \rangle$ **/g cm^{-2}**
$10^{16.875} .. 10^{17.125}$	10^{17}	369	655±4
$10^{17.125} .. 10^{17.375}$	$10^{17.25}$	1257	677±2
$10^{17.375} .. 10^{17.625}$	$10^{17.5}$	1880	685±2
$10^{17.625} .. 10^{18.875}$	$10^{17.75}$	1651	695±2
$10^{17.875} .. 10^{18.125}$	10^{18}	910	711±2
$10^{18.125} .. 10^{18.375}$	$10^{18.25}$	445	723±3
$10^{18.375} .. 10^{18.625}$	$10^{18.5}$	175	733±5

Table 6.2.: Mean $X_{\max}$ including statistical uncertainty per energy bin and the number of events per bin. The $X_{\max}$ is not corrected for detector effects. The values are plotted in fig. 6.5

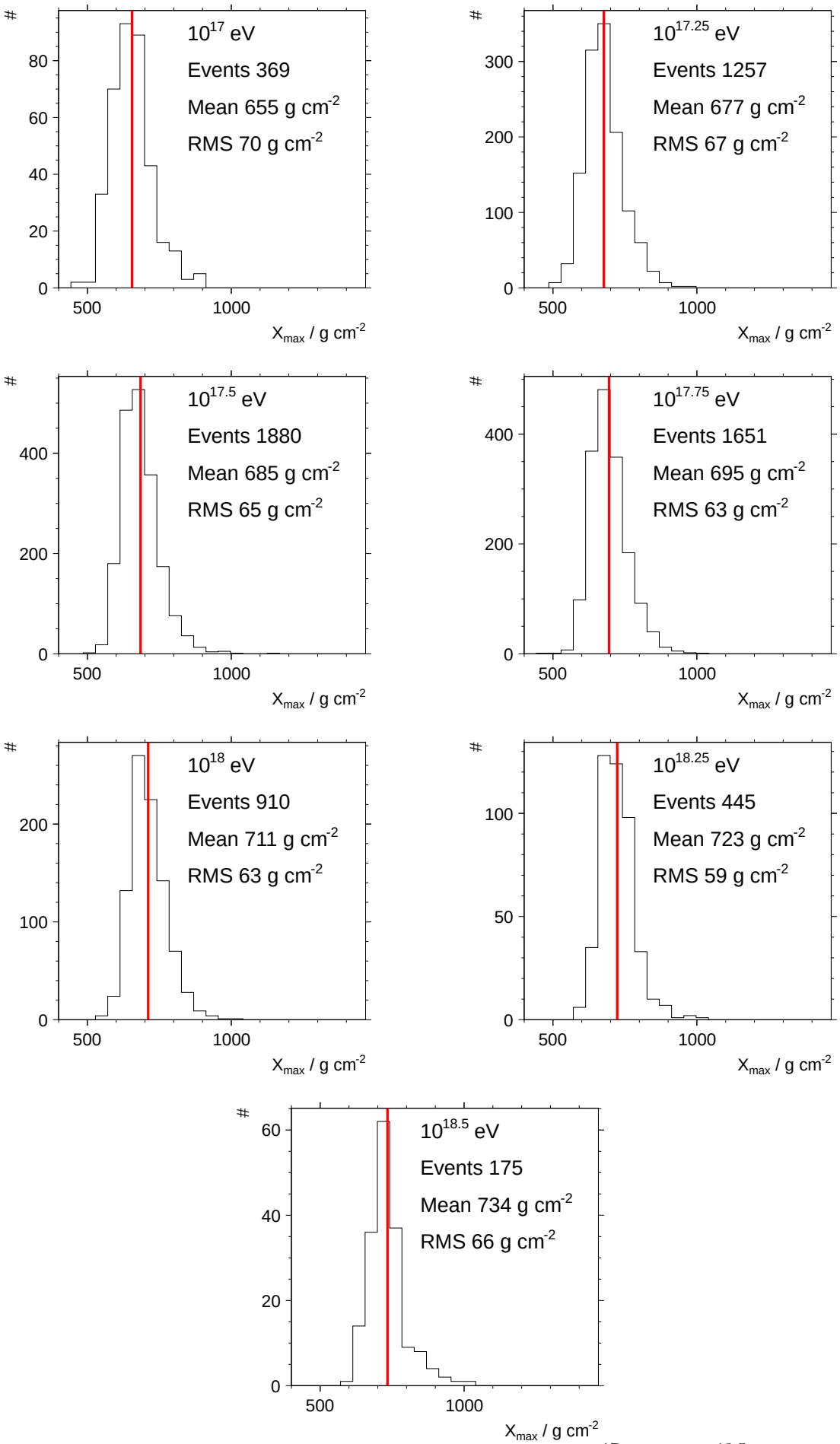

Figure 6.5.: $X_{\max}$ distribution of each energy bin from 10^{17} eV to $10^{18.5}$ eV. The denoted energy is the centre of the bin. The vertical line in the plots denotes the data mean $X_{\max}$ (not the binned mean) of the energy bin.

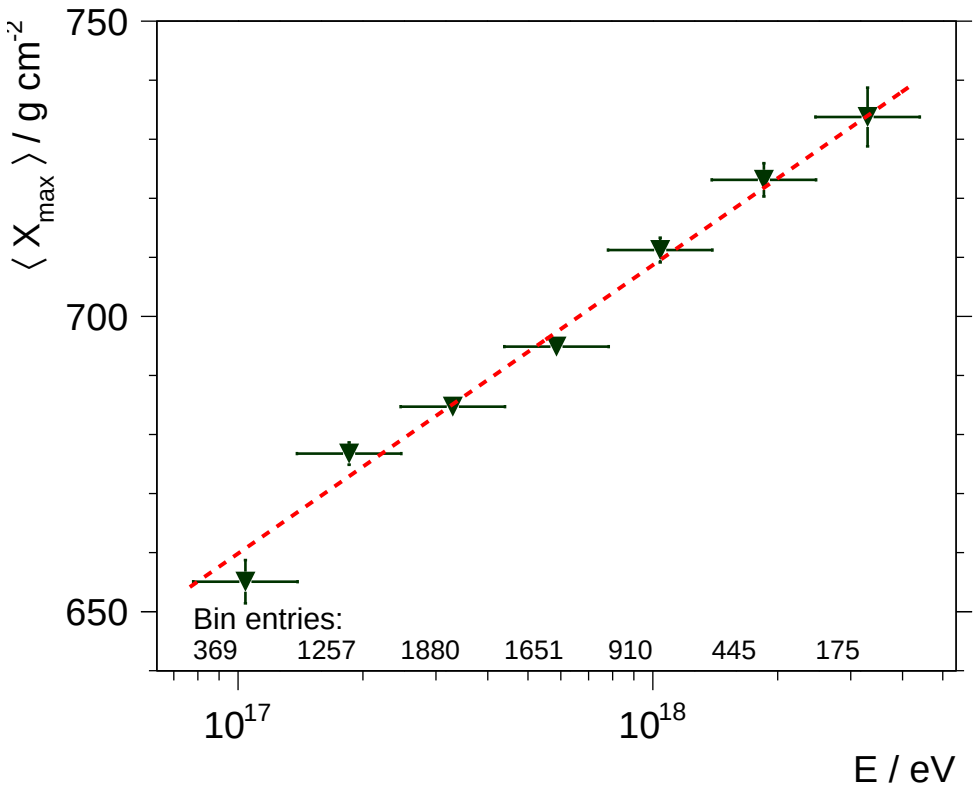

(a) Mean of shower maximum $X_{\max}$ depending on the primary energy

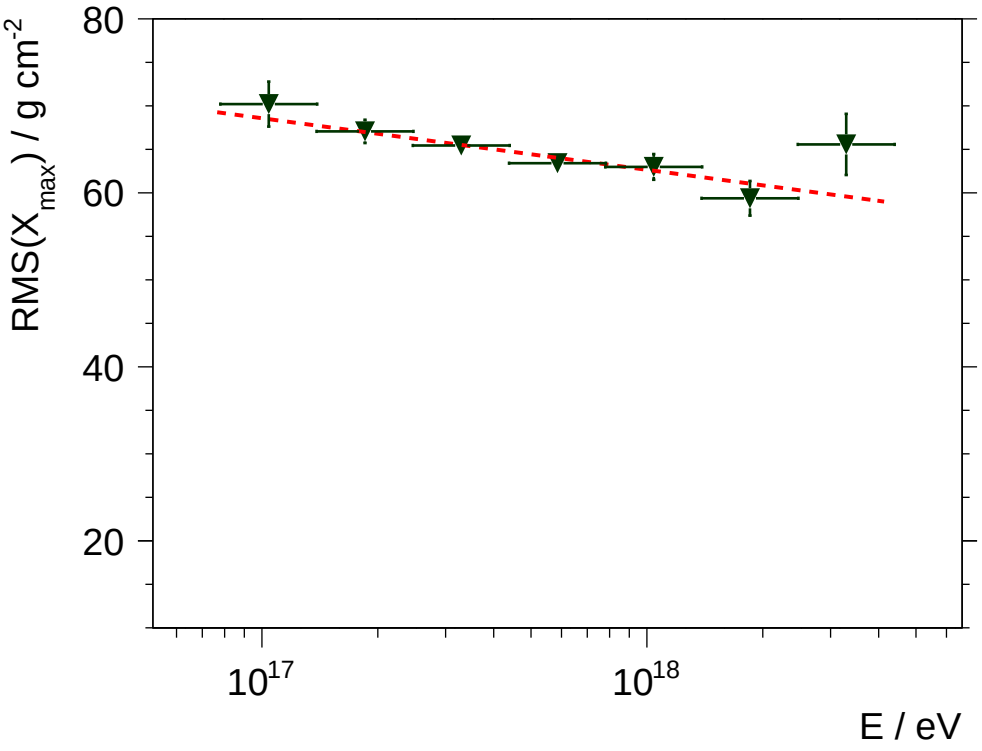

(b) The uncorrected RMS($X_{\max}$) for each energy bin

Figure 6.6.: Mean of shower maximum $X_{\max}$ and RMS($X_{\max}$) depending on the primary energy. Data points show the uncorrected values for each energy bin. The horizontal bars indicates the bin width. Vertical errors denote the statistical uncertainties. The dashed line is the result of a χ^2-fit of eqn. 6.2.

6.3. Averaged Detector Resolution

In sec. 5.4.3 (p. 49) the detector resolution for different primaries and hadronic interaction models is derived by using the Auger RealMC detector simulation with simulated CONEX air showers. However, neither the true composition nor the correct hadronic interaction model is known a priori.

Therefore, the available information about the detector resolution is averaged over the models and afterwards over the primaries. The model- and primary-independent resolution of energy, $X_{\max}$ and $\mathrm{RMS}(X_{\max})$ is calculated by using the mean. To not emphasize a specific model or primary an *equally*-weighted mean is chosen. For the quantity Y, which denotes energy E, $X_{\max}$ and $\mathrm{RMS}(X_{\max})$, the mean was calculated as

$$\langle Y \rangle = \frac{1}{N} \sum_{i=0}^{N} y_i \tag{6.3}$$

with the corresponding uncertainty

$$\sigma\left(\langle Y \rangle\right) = \frac{1}{N} \sqrt{\sum_{i=0}^{N} \sigma_{y,i}^2} \quad . \tag{6.4}$$

The per primary average is calculated from all reconstructed showers passing the quality cuts. The mean resolution over the primaries is calculated as the unweighted mean of the per primary averages. This means that the mean resolution represents the resolution of a 50 % iron and 50 % proton composition.

Figs. 6.7a, 6.7b and 6.8 show the resulting mean resolution for the aforementioned quantities. Additionally, to the model and primary independent mean also the per primary averaged resolution is shown. The mean resolution is assumed to be the best estimator for the real detector resolution. Therefore, in the following sections resolution always refers to the mean resolution if not stated otherwise.

In every energy bin the average energy resolution for protons is on average 0.5 % worse than the mean resolution. The $X_{\max}$ resolution in the energy range from $10^{17.75}\,\mathrm{eV}$ up to $10^{18.5}\,\mathrm{eV}$ of proton induced showers is about $0.3\,\mathrm{g\,cm^{-2}}$ worse than the mean resolution. Between $10^{17}\,\mathrm{eV}$ and $10^{17.75}\,\mathrm{eV}$ the averaged proton resolution is better than the averaged iron resolution. At the lowest energy bin the mean $X_{\max}$ resolution is worst $(27.0 \pm 0.4)\,\mathrm{g\,cm^{-2}}$.

The mean $\mathrm{RMS}(X_{\max})$ resolution gets better with increasing primary energy from $(1.00 \pm 0.03)\,\mathrm{g\,cm^{-2}}$ at $10^{17}\,\mathrm{eV}$ to $(0.475 \pm 0.006)\,\mathrm{g\,cm^{-2}}$ at $10^{18.5}\,\mathrm{eV}$. Below $10^{17.75}\,\mathrm{eV}$ the average resolution for iron primaries is about $0.1\,\mathrm{g\,cm^{-2}}$ worse than the mean resolution.

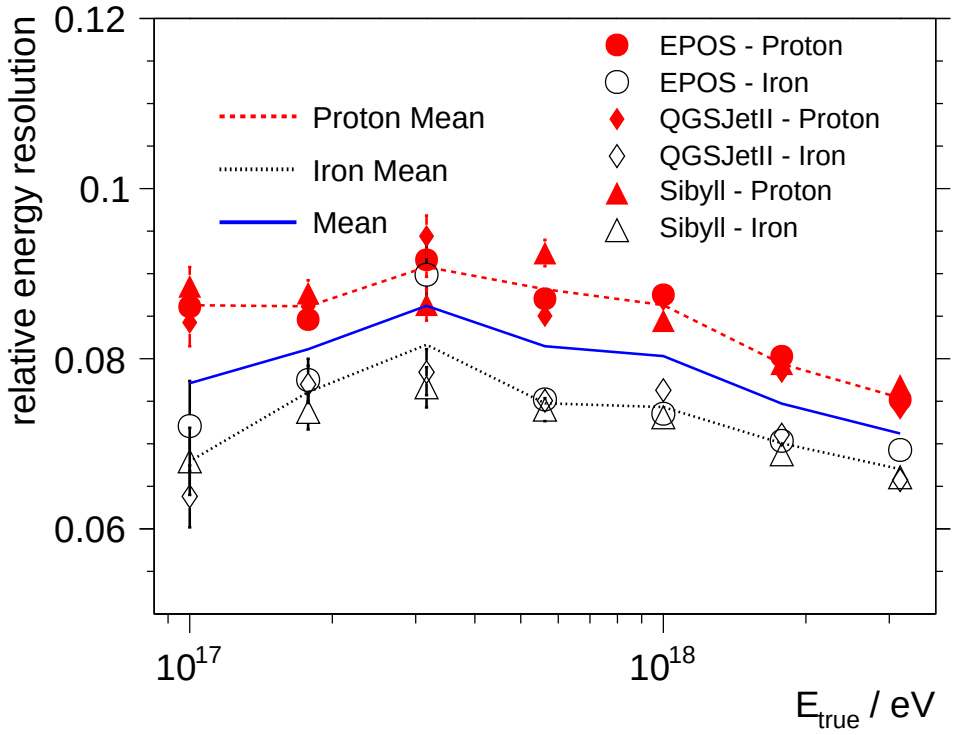

(a) Energy resolution as a function of energy.

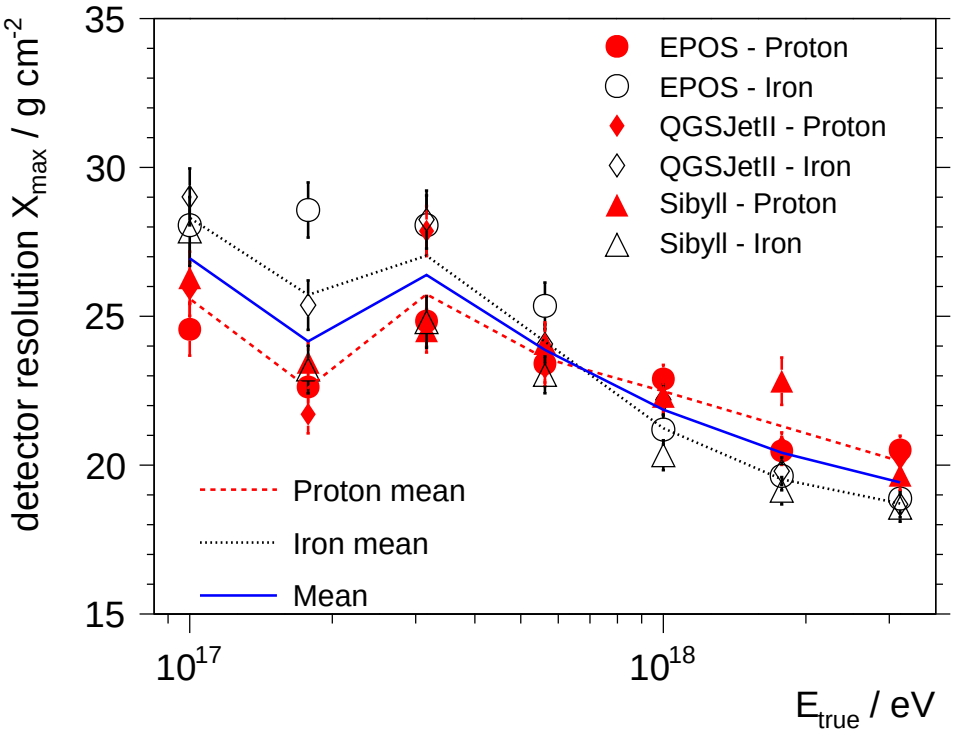

(b) $X_{\max}$ resolution as a function of energy.

Figure 6.7.: Average detector energy (fig. 6.7a) and $X_{\max}$ (fig. 6.7b) resolution as a function of the primary energy, determined from RealMC (cf. sec. 5.4.3). The red points mark the resolution determined from simulations with proton primaries. The corresponding red lines show the averaged proton resolution. The black line and marker have the same meaning but for iron primaries. Additionally, the blue line shows the average over both primaries and hadronic interaction models.

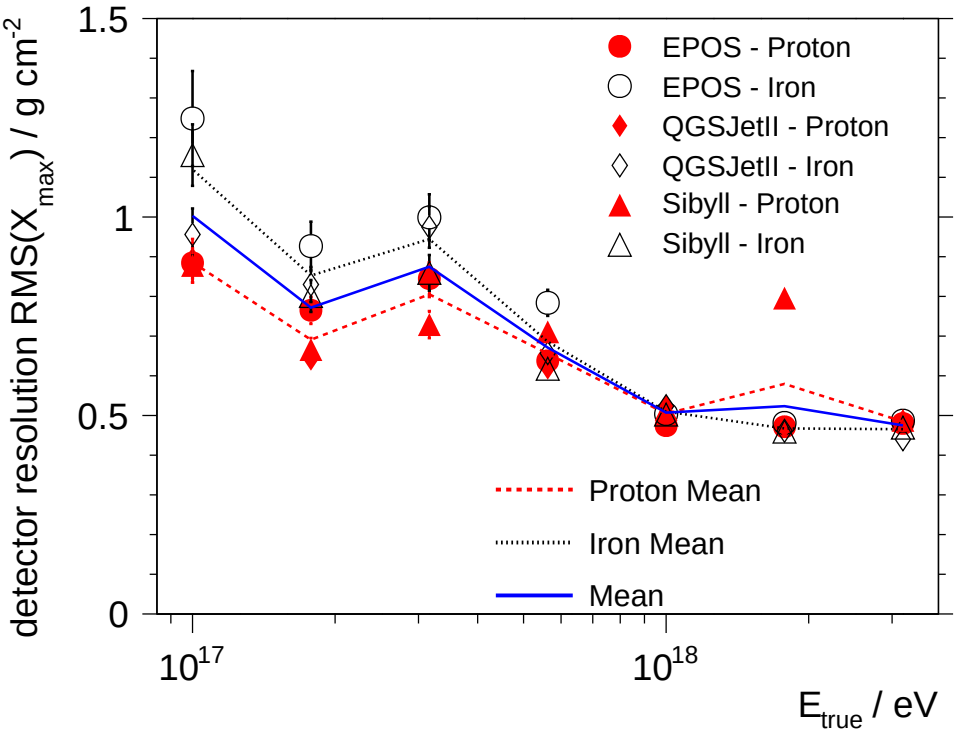

Figure 6.8.: Average detector RMS($X_{\max}$) resolution as a function of the primary energy, determined from RealMC (cf. sec. 5.4.3). The red points mark the resolution determined from simulations with proton primaries. The corresponding red lines show the averaged proton resolution. The black line and marker have the same meaning but for iron primaries. Additionally, the blue line shows the average over both primaries and hadronic interaction models.

6.4. Correction of Detector Bias

To apply a correction for the $\langle X_{\mathrm{max}} \rangle$ and RMS(X_{max}) bias, a correction of the energy has to be applied first, because the corrections are determined for the true energy E_{true} and not for the reconstructed energy E_{rec}. As mentioned in sec. 6.3, it is not clear which interaction model describes the physical processes in an extensive air shower best, or which kind of primary induced it. Therefore, also for the bias correction on energy, $\langle X_{\mathrm{max}} \rangle$ and RMS(X_{max}) in each case the average of the iron and proton primaries appears to be the best estimator for the corrections.

6.4.1. Energy Correction

The energy correction is applied to the selected events and not the energy bins, because the reconstruction bias on $\langle X_{\mathrm{max}} \rangle$ is also determined from binning on E_{true}. Though the bias correction is determined from binned data, the correction between the bins has to be interpolated. Due to a lack of knowing a better interpolation between the bins, a linear interpolation as the simplest possible one is assumed.

The finally applied energy bias correction is shown in fig. 6.10. The applied correction takes a mixed composition of 50 % proton and 50 % iron primaries into consideration. Additionally, the bias average for each primary per energy bin is shown. In general, the mean energy bias shows that by default the energy is reconstructed too low for a mixed composition. The mean bias correction increases with increasing energy from $(-4.1 \pm 0.2)\,\%$ at $10^{17}\,\mathrm{eV}$ to $(-3.60 \pm 0.03)\,\%$ at $10^{18.5}\,\mathrm{eV}$. The average bias for proton induced showers is between $\pm 1\,\%$. For iron primaries, the average energy reconstruction bias is evolves from $-10\,\%$ at $10^{17}\,\mathrm{eV}$ to $-6\,\%$ at $10^{18.5}\,\mathrm{eV}$. This shows, that the energy reconstruction is comparatively better fitted for proton induced showers than for iron induced ones.

The correction is applied as a correction factor a, which is assumed to be without uncertainties

$$E_{\mathrm{true}} = a \cdot E_{\mathrm{rec}} \quad , \qquad \sigma(E_{\mathrm{true}}) = \sigma(E_{\mathrm{rec}}) \qquad . \tag{6.5}$$

Additionally, to estimate the introduced systematic uncertainty on $\langle X_{\mathrm{max}} \rangle$ and the corresponding RMS, the energy bias correction is also performed for iron and proton primaries. The resulting values for $\langle X_{\mathrm{max}} \rangle$ and RMS(X_{max}) after the energy binning are compared. The highest deviation from the overall mean correction is considered as the resulting systematic uncertainty induced by applying the energy correction. The results are shown in tab. 6.3 and the introduced average systematic uncertainty on $\langle X_{\mathrm{max}} \rangle$ is about $(2 \pm 1)\,\mathrm{g\,cm^{-2}}$. The higher systematic uncertainty for the lowest energy bin at $10^{17}\,\mathrm{eV}$ can be expected due to the increasing difference between the reconstructed energy for proton and iron induced showers with decreasing energy. The introduced mean systematic uncertainty on the RMS(X_{max}) is about $(1.0 \pm 0.8)\,\mathrm{g\,cm^{-2}}$.

The X_{max} distribution in each energy bin after applying the energy correction is shown in fig. 6.9.

6.4.2. Corrected Depth Of Shower Maximum $\langle \mathbf{X_{max}} \rangle$

After applying the energy correction and performing the energy binning, the mean X_{max} per bin is corrected for the reconstruction bias described in sec. 5.4.4. As stated before, also here the average bias (over all simulated kinds of primaries and hadronic interaction models) is assumed as the best correction method. The

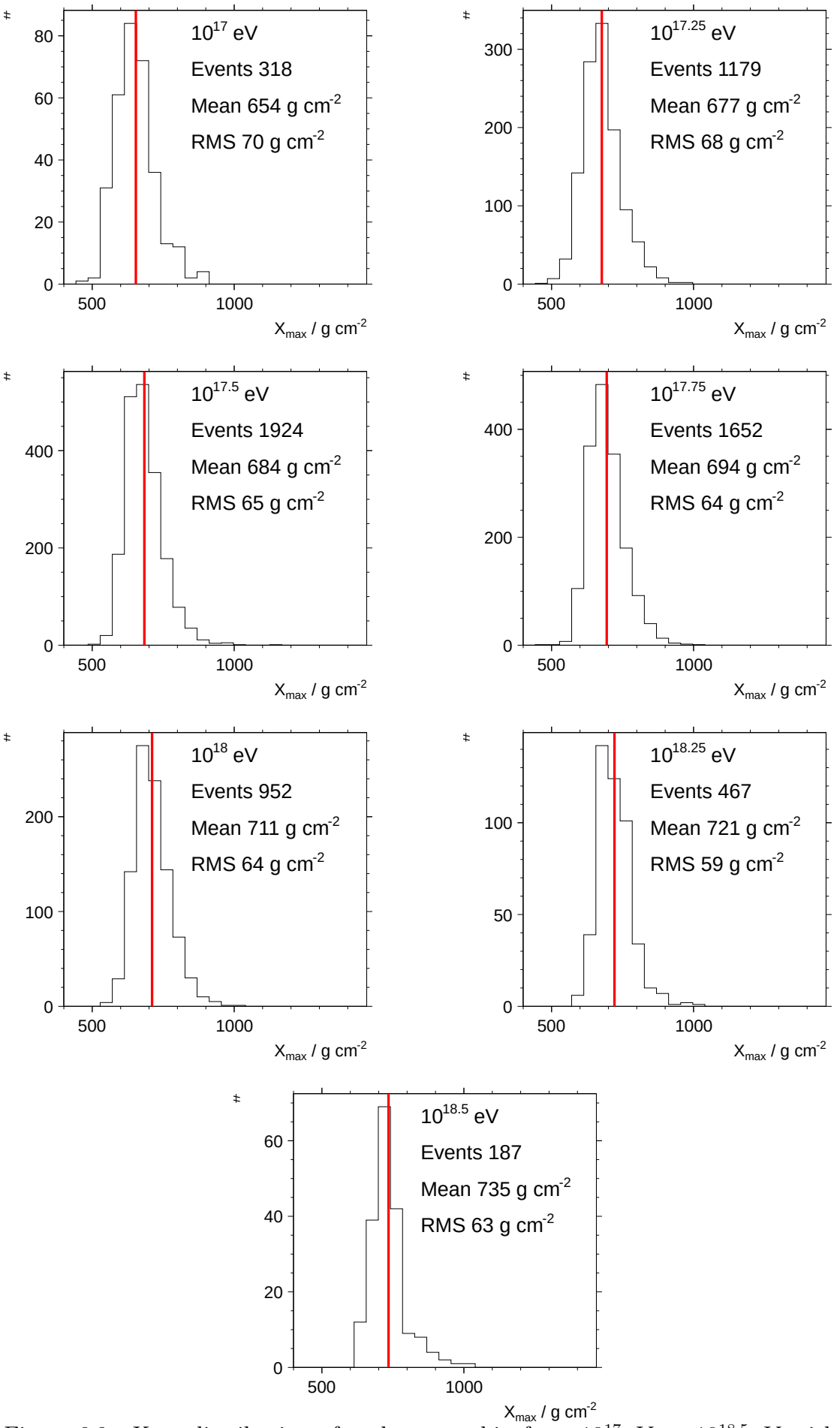

Figure 6.9.: $X_{\max}$ distribution of each energy bin from 10^{17} eV to $10^{18.5}$ eV with applied energy correction. The vertical line in the plots denotes the data mean $X_{\max}$ (not the binned mean) of the energy bin.

E / eV	$\langle \mathbf{X_{max}} \rangle$ **/g cm^{-2}** mean±stat.±syst.	**RMS($\mathbf{X_{max}}$)/g cm^{-2}** mean±stat.±syst.
10^{17}	654± 4 ±4	70.2± 2.8 ±0.3
$10^{17.25}$	677± 2 ±2	67.9± 1.4 ±0.6
$10^{17.5}$	684± 2 ±1	65.1± 1.0 ±0.2
$10^{17.75}$	694± 2 ±1	63.6± 1.1 ±0.7
10^{18}	711± 2 ±2	63.8± 1.5 ±0.9
$10^{18.25}$	721± 3 ±2	59± 2 ±2
$10^{18.5}$	735± 5 ±2	63± 3 ±2

Table 6.3.: For each energy bin (denoted are the bin centres) the $\langle X_{\mathrm{max}} \rangle$ and RMS(X_{max}) (uncorrected for $\langle X_{\mathrm{max}} \rangle$ bias and RMS(X_{max}) bias), their statistical uncertainty and the systematic uncertainty arising from the energy correction are shown.

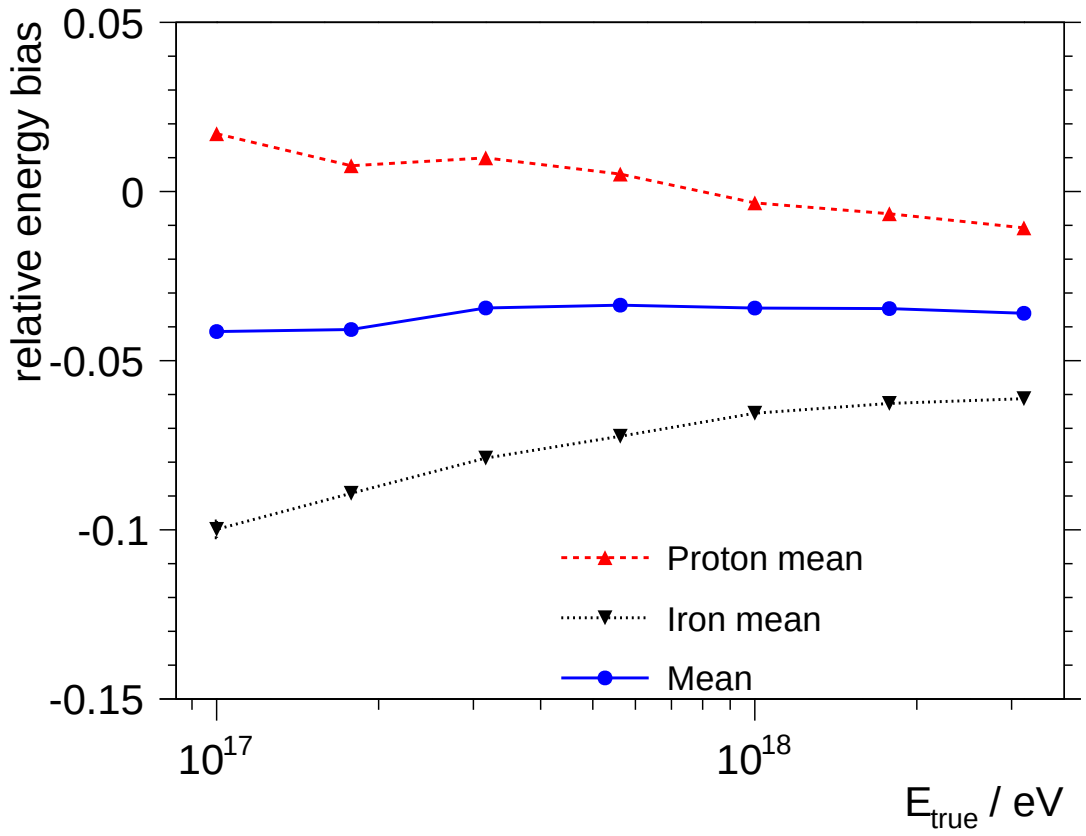

Figure 6.10.: Energy bias correction from RealMC as function of E_{true}. The black ▼ marker denotes the iron mean bias, the red ▲ marker the proton mean bias (the mean over used hadronic interaction models) and the blue • marker the mean over both primaries with the used interaction models. The corresponding lines denote the linear interpolation between the bin centres.

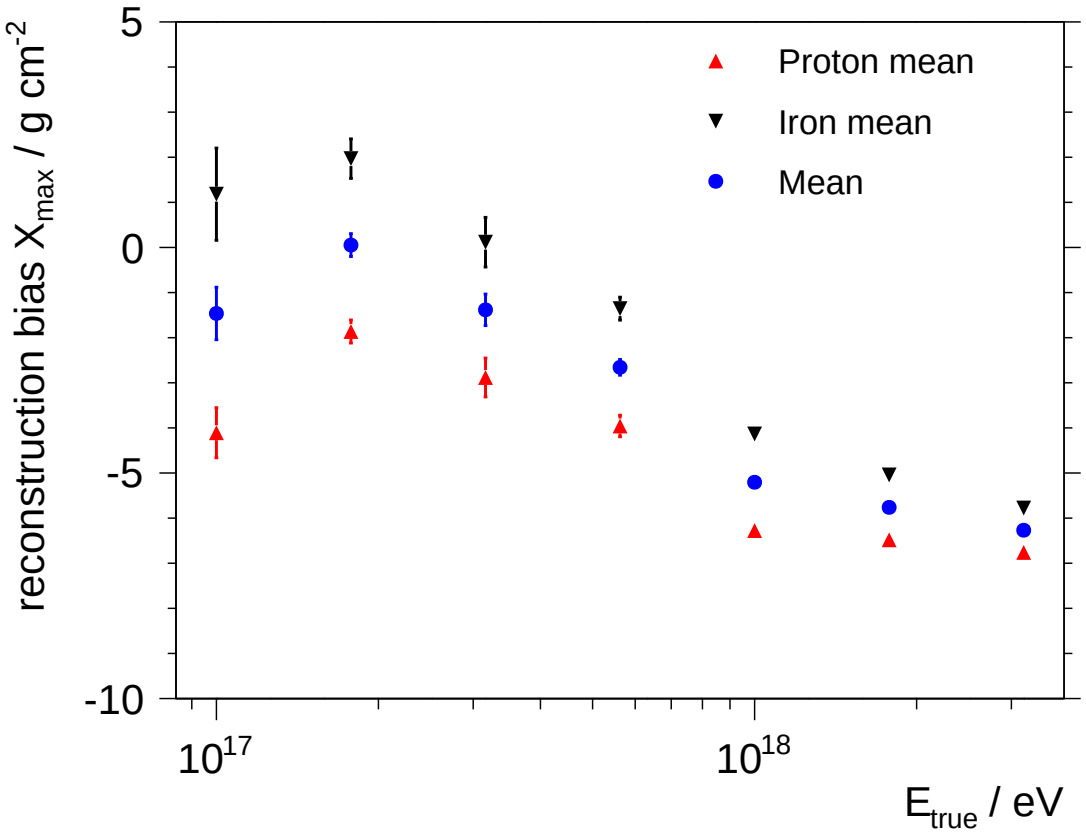

Figure 6.11.: $\langle X_{\mathrm{max}} \rangle$ bias correction as a function of energy determined from RealMC. The black ▼ marker denotes the iron mean bias, the red ▲ marker the proton mean bias (each the mean over used hadronic interaction models) and the blue • marker the mean over both primaries with the used interaction models.

resulting mean bias is shown in fig. 6.11. As one can expect from sec. 5.4.4, the difference between the primaries is rather small for energies above $10^{17.75}$ eV. To lower energies, the deviation between the primary means and the overall mean increases. The differences between the primaries are taken into account as a systematic uncertainty.

The correction is applied by subtracting the bias b_i of the i-th energy bin from the reconstructed $\langle X_{\mathrm{max,rec,i}} \rangle$:

$$\langle X_{\mathrm{max,true,i}} \rangle = \langle X_{\mathrm{max,rec,i}} \rangle - b_i \ , \quad \sigma\left(\langle X_{\mathrm{max,true,i}} \rangle\right) = \sigma\left(\langle X_{\mathrm{max,rec,i}} \rangle\right) \tag{6.6}$$

The systematic uncertainties resulting from the energy and X_{max} bias correction are shown in fig. 6.12. In addition, the combined systematic uncertainty is shown. The energy correction gives a rather constant contribution and is the dominant one besides for the energy range from $10^{17.25}$ eV to $10^{17.75}$ eV. Besides the lowest bin at 10^{17} eV the overall average systematic uncertainty from the corrections is about $\pm 3\,\mathrm{g\,cm^{-2}}$. This effect is smaller than the average detector resolution of about $(23 \pm 3)\,\mathrm{g\,cm^{-2}}$ (cf. fig. 6.7).

The $\langle X_{\mathrm{max}} \rangle$ as a function of energy from the combined HEAT and Coihueco hybrid reconstruction, including the presented corrections, is shown in fig. 6.13. Additionally, the published Auger data from [75] is presented. It is shown that at the highest energy bin ($10^{18.5}$ eV) the statistic compared to the other bins is relatively

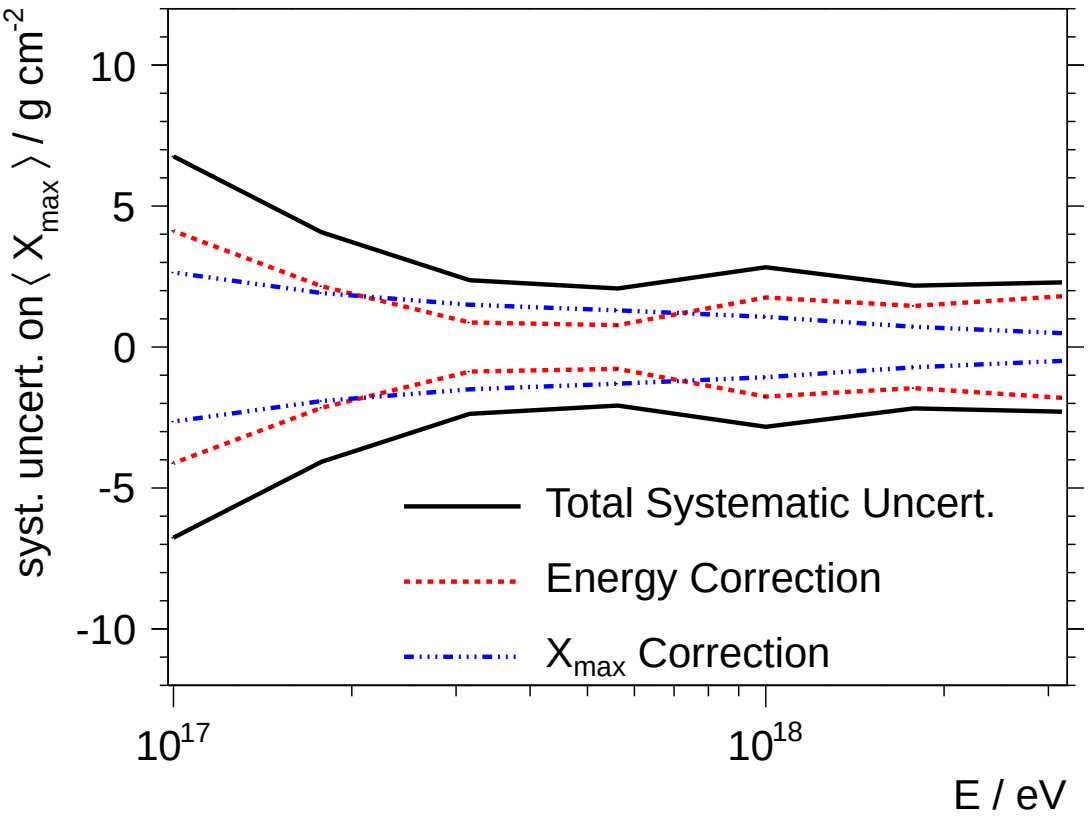

Figure 6.12.: Systematic uncertainty on $\langle X_{\max} \rangle$ from bias corrections evolving with energy. The solid black line is the combined systematic uncertainty from the energy and the $X_{\max}$ correction. The red simple dashed line is the bias introduced by the energy correction. The blue line denotes the uncertainty from the $X_{\max}$ bias correction.

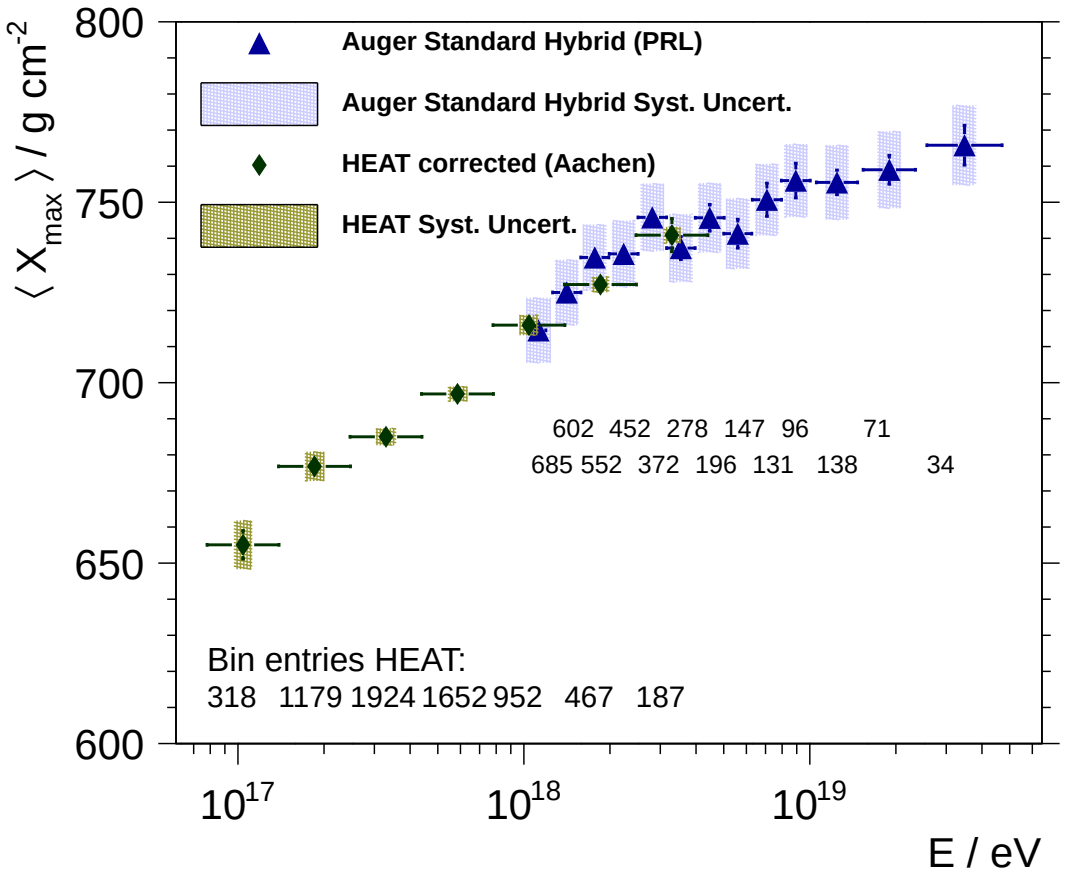

Figure 6.13.: $\langle X_{\mathrm{max}} \rangle$ over energy from HEAT and Coihueco (green ♦ markers) and from [75] (published Auger data; blue ▲ marker). The horizontal bars denote the bin width. Vertical uncertainties are the statistical uncertainties. Shaded areas denote the systematical uncertainties. The numbers in the lower, left corner denote the entries per bin in the HEAT and Coihueco data points. The other numbers display the entries per bin for the published Auger data.

low. In the overlapping energy region of both analyses (from 10^{18} eV to $10^{18.5}$ eV) the data agrees well in their 1–2σ statistical uncertainties. Also the determined detector resolutions of $(23 \pm 3)\,\mathrm{g\,cm^{-2}}$ from this analysis and $(21 \pm 3)\,\mathrm{g\,cm^{-2}}$ from [75] are compatible within 1σ. However, not all systematical effects, like the influence of the weather on the reconstruction, are taken into account. Therefore, the systematical uncertainties of this analysis are under estimated.

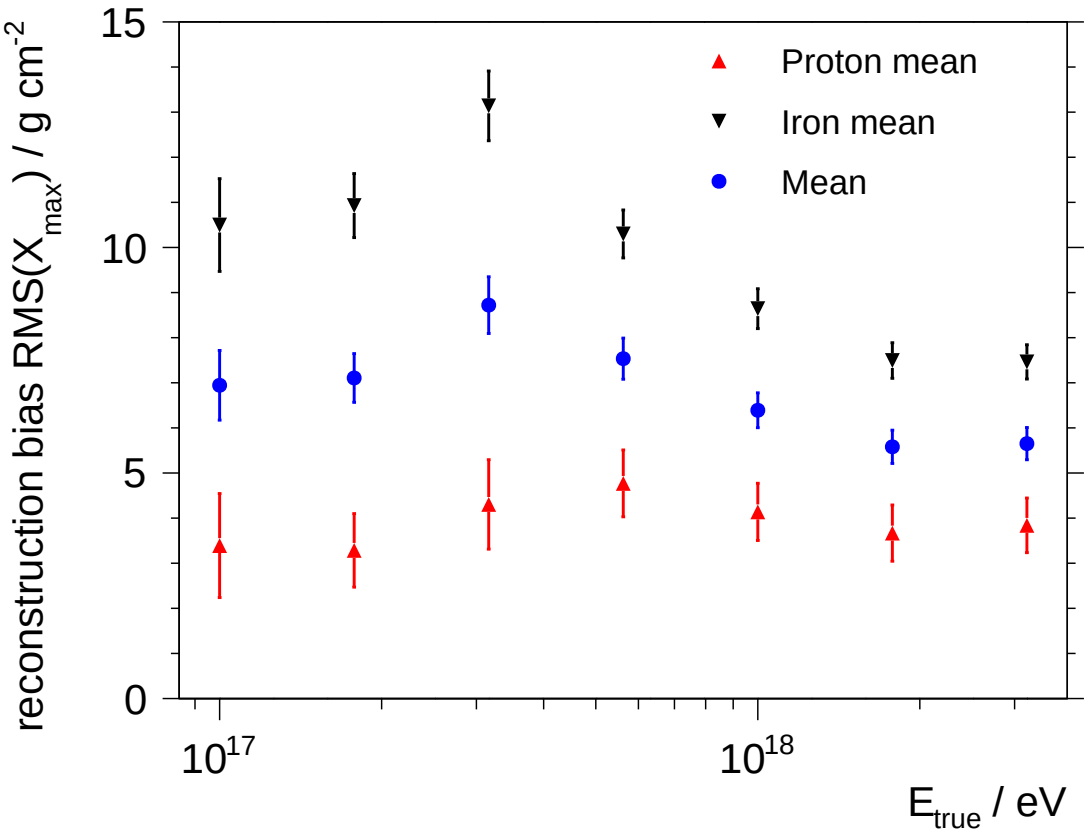

Figure 6.14.: RMS($X_{\max}$) bias correction from RealMC. The black ▼ marker denotes the iron mean bias, the red ▲ marker the proton mean bias (the mean over used hadronic interaction models) and the blue • marker the mean over both primaries with the used interaction models.

6.4.3. Correction of RMS of $X_{\max}$

Besides the $\langle X_{\max} \rangle$, also the RMS($X_{\max}$) is sensitive to the mass composition (cf. sec. 2.3.2). Like for the $\langle X_{\max} \rangle$, a correction of the mean bias of RMS($X_{\max}$) is applied by subtracting the bias from the corresponding data bin. The applied correction is shown in fig. 6.14. The mean RMS correction is rather constant at $7\,\mathrm{g\,cm^{-2}}$. The bias has a maximum of $8.7\,\mathrm{g\,cm^{-2}}$ at $10^{17.5}\,\mathrm{eV}$ and a minimum bias of about $5.6\,\mathrm{g\,cm^{-2}}$ at $10^{18.25}\,\mathrm{eV}$. The iron average bias is between $2\,\mathrm{g\,cm^{-2}}$ and $4\,\mathrm{g\,cm^{-2}}$ higher than the mean bias.

The RMS($X_{\max}$) correction is applied analogous to the correction of the $\langle X_{\max} \rangle$. The systematic uncertainty introduced by choosing the mean bias on the RMS for the correction is determined as the difference between the mean bias and each primaries' bias. The systematic uncertainty resulting from the RMS bias correction and from the energy bias correction is shown in fig. 6.15. The systematic uncertainty is rather constant at about $\pm 5\,\mathrm{g\,cm^{-2}}$ over the whole considered energy range. For energies above $10^{18}\,\mathrm{eV}$ the energy correction dominates. The values of the complete dataset are shown in the appendix in tab. E.1 on p. 117.

The corrected RMS($X_{\max}$) is shown in fig. 6.16. Additionally, the published Auger data from [75] is included in the plot. In the overlapping energy range from $10^{18}\,\mathrm{eV}$ to $10^{18.5}\,\mathrm{eV}$, the HEAT and the standard Auger hybrid measurement agree well within their 1σ statistical uncertainty intervals.

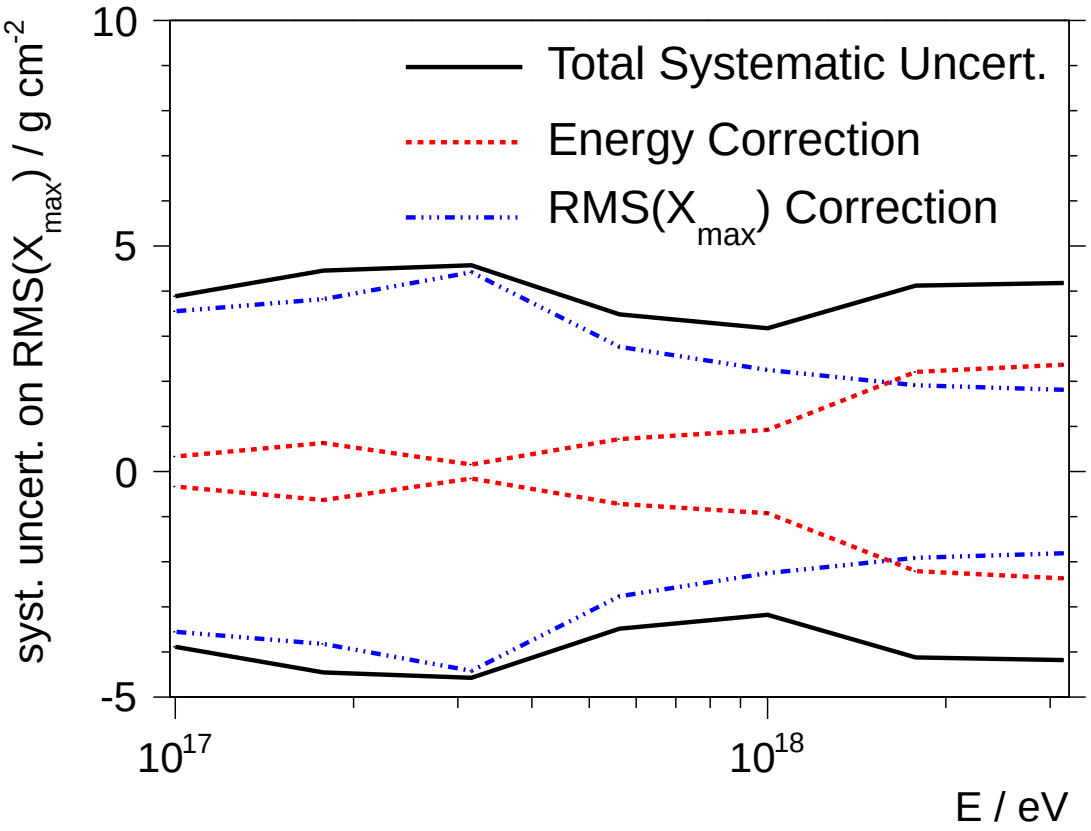

Figure 6.15.: Systematic uncertainty on RMS(X_{max}) from bias corrections evolving with energy. The solid black line is the combined systematic uncertainty from the energy and the RMS(X_{max}) correction. The red simple dashed line is the bias introduced by the energy correction. The blue line denotes the uncertainty from the RMS(X_{max}) bias correction.

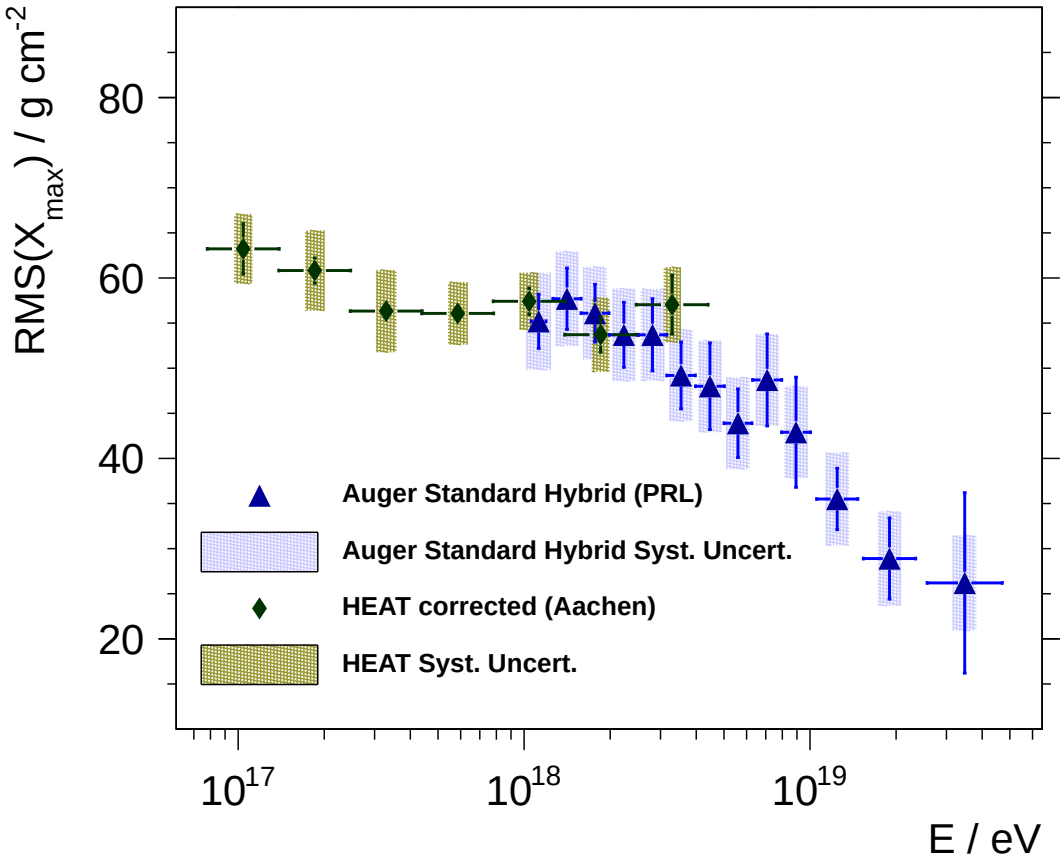

Figure 6.16.: RMS($X_{\max}$) over energy from HEAT and Coihueco (green ♦ markers) and from [75] (published Auger data; blue ▲ marker). The horizontal uncertainties denote the bin width. Vertical uncertainties are the statistical uncertainties. The shaded green area denotes the systematical uncertainties for this analysis. The shaded blue area denotes the systematical uncertainties on the published Auger data.

7. Mass Composition

To get a conclusion about the mass composition of the primaries inducing the observed extensive air showers, it is important to compare the corrected data with the predictions of several hadronic interaction models. For this purpose, three hadronic interaction models (QGSJet01[80, 81], QGSJetII[70, 71] and Sibyll 2.1[35, 69]) for proton, helium, iron and a mixed composition are used. The mixed composition component consists of 50 % proton and 50 % iron induced showers. The necessary information for the comparison is extracted by fitting eqn. 6.2 to 10000 CONEX showers per model and primary, solely simulated for this purpose. An example is given in fig. 7.1. The CONEX data and the detailed fit results are shown in the appendix D (p. 109).

7.1. Comparison of $\langle X_{\mathrm{max}} \rangle$ with Hadronic Interaction Models

The $\langle X_{\mathrm{max}} \rangle$ as a function of energy including the previously introduced correction is shown in fig. 7.2. Additionally, the predictions from different hadronic interaction models are shown.

Comparing the bias-corrected $\langle X_{\mathrm{max}} \rangle$ distribution to the predictions of the used hadronic interaction models, the measured $\langle X_{\mathrm{max}} \rangle$ distribution indicates a composition lighter than iron. A qualitatively good agreement is achieved with simulated showers induced by helium primaries. Furthermore eqn. 6.2 is fitted to the data to determine the slope m. At first glance, the fit result seems to well describe the data. The fit results in a $\chi^2/N_{\mathrm{dof}} = 2.5$ with a probability $P(\chi^2|N_{\mathrm{dof}}) = 0.04$. The slope is determined to $(53 \pm 2)\,\mathrm{g\,cm^{-2}}$ and the offset to $(-24 \pm 4) \cdot 10\,\mathrm{g\,cm^{-2}}$.

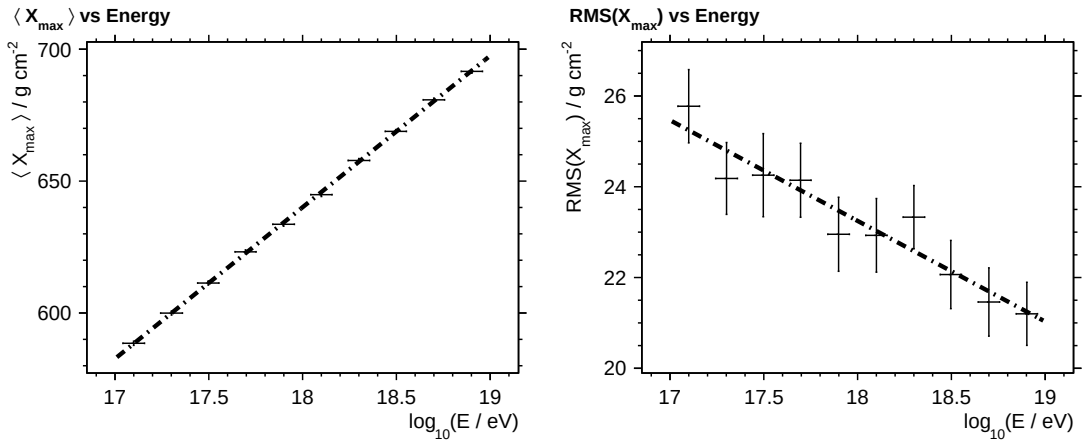

Figure 7.1.: Fit of eqn. 6.2 on $\langle X_{\mathrm{max}} \rangle$ and RMS(X_{max}) distribution generated with CONEX from Sibyll 2.1 hadronic interaction model for iron primaries.

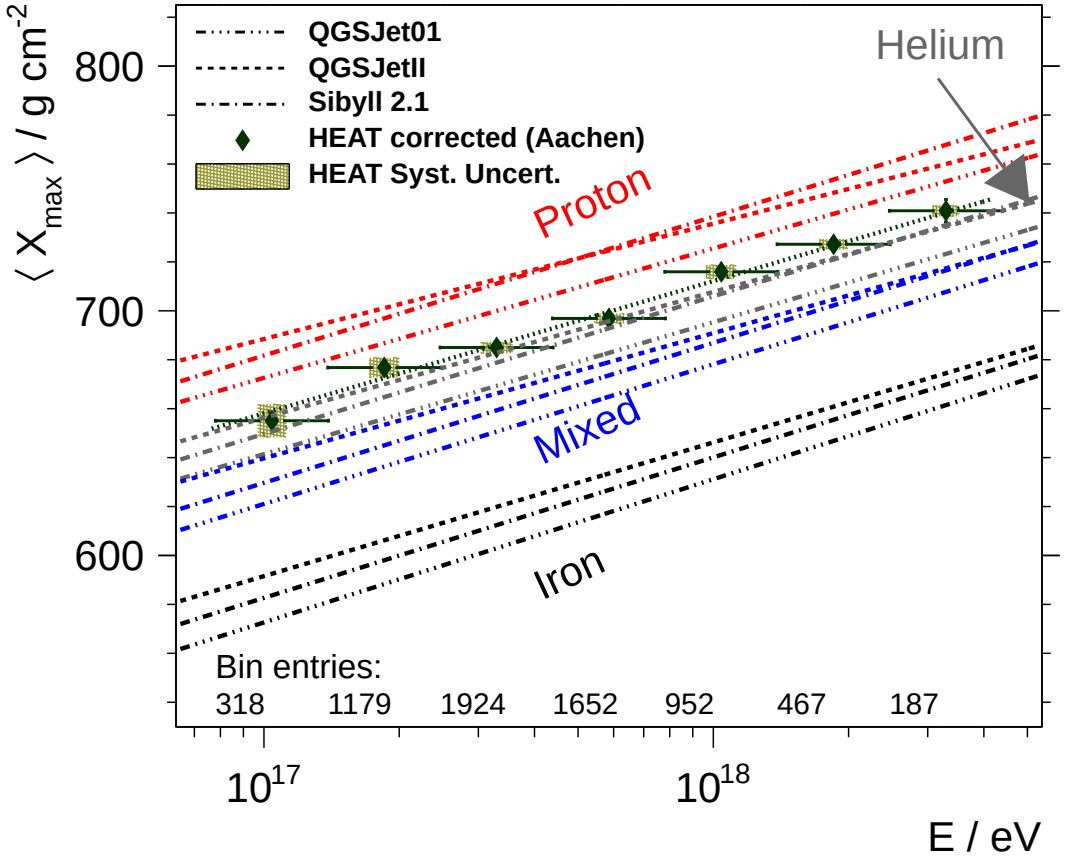

Figure 7.2.: $\langle X_{\max} \rangle$ over energy from combined HEAT and Coihueco reconstruction with applied corrections for energy and $\langle X_{\max} \rangle$ bias determined from RealMC. The horizontal bars denote the bin size. Vertical uncertainties denote the statistical uncertainty on the $\langle X_{\max} \rangle$. The shaded area denotes the systematical uncertainties. The dotted line through the data is the result of a χ^2-fit of eqn. 6.2 on the data. Additionally, the lower, black lines denote the model predictions for iron primaries and the upper, red lines those for protons. The grey lines in between denote the prediction for helium primaries. The blue lines display the predictions for a composition consisting of 50 % iron and 50 % proton primaries.

E / eV	$\langle \ln \mathbf{A} \rangle$
	value $\pm$ stat. syst.
10^{17}	$1.5 \pm 0.1\ ^{+0.3}_{-0.3}$
$10^{17.25}$	$1.21 \pm 0.07\ ^{+0.15}_{-0.15}$
$10^{17.5}$	$1.18 \pm 0.06\ ^{+0.09}_{-0.09}$
$10^{17.75}$	$1.00 \pm 0.07\ ^{+0.09}_{-0.09}$
10^{18}	$0.74 \pm 0.09\ ^{+0.12}_{-0.12}$
$10^{18.25}$	$0.9 \pm 0.1\ ^{+0.1}_{-0.1}$
$10^{18.5}$	$0.7 \pm 0.2\ ^{+0.1}_{-0.1}$

Table 7.1.: Numerical results for the transformation eqn. 7.1 from $\langle X_{\mathrm{max}} \rangle$ to $\langle \ln A \rangle$.

7.2. Average Logarithmic Atomic Mass Number

According to [10], the average atomic mass number A of the shower inducing primary can be obtained from the measured $\langle X_{\mathrm{max}} \rangle$ and shower simulations for proton and iron primaries by applying

$$\langle \ln A \rangle = \frac{\langle X_{\mathrm{max}}^{\mathrm{meas}} \rangle - \langle X_{\mathrm{max}}^{\mathrm{p}} \rangle}{\langle X_{\mathrm{max}}^{\mathrm{Fe}} \rangle - \langle X_{\mathrm{max}}^{\mathrm{p}} \rangle} \ln(A_{\mathrm{Fe}}) \tag{7.1}$$

to the measured $\langle X_{\mathrm{max}} \rangle$ per energy bin. The result of the transformation including the statistical uncertainties from Gaussian error propagation is shown in fig. 7.3. Like for the applied reconstruction bias corrections on energy, $\langle X_{\mathrm{max}} \rangle$ and $\mathrm{RMS}(X_{\mathrm{max}})$, for each primary the average value of the models is used for the transformation from the measured $\langle X_{\mathrm{max}} \rangle$ to $\langle \ln A \rangle$. The arising systematic uncertainty is determined by redoing the transformation for each model and determining the maximal deviation. Additionally, the systematic uncertainties arising from the systematic uncertainties on $\langle X_{\mathrm{max}} \rangle$ are shown. The numerical results are given in tab. 7.1.

The transformation is based on the models' predictions and the $\langle X_{\mathrm{max}} \rangle$, hence it is not unexpected, that the $\langle \ln A \rangle$ indicates a composition dominated by helium or proton primaries like fig. 7.2 suggests, too.

The determined $\langle \ln A \rangle$ in all energy bins is dominated by the systematical uncertainty rather than the statistical uncertainty. At $10^{17.75}\,\mathrm{eV}$ the systematical uncertainties are largest. As one can expect from the previously shown $\langle X_{\mathrm{max}} \rangle$ distributions, the statistical uncertainty is largest on the highest energy bin.

Starting from a composition lighter than helium at $10^{18.5}\,\mathrm{eV}$, the $\langle \ln A \rangle$ hints on an increasingly heavier composition towards lower energies. At $10^{17}\,\mathrm{eV}$ the $\langle \ln A \rangle$ is compatible with helium within 1σ and hints on an even heavier composition.

7.3. Comparison of $\mathrm{RMS}(\mathbf{X_{max}})$ with Hadronic Interaction Models

In addition to the $\langle X_{\mathrm{max}} \rangle$ and the derived $\langle \ln A \rangle$, also the $\mathrm{RMS}(X_{\mathrm{max}})$ is sensitive to the mass composition (cf. 2.3.2). The comparison of the corrected Coihueco and HEAT $\mathrm{RMS}(X_{\mathrm{max}})$ is shown in fig. 7.4. The models' predictions for a mixed composition are very close to and even partially overlapping with those for a pure proton composition.

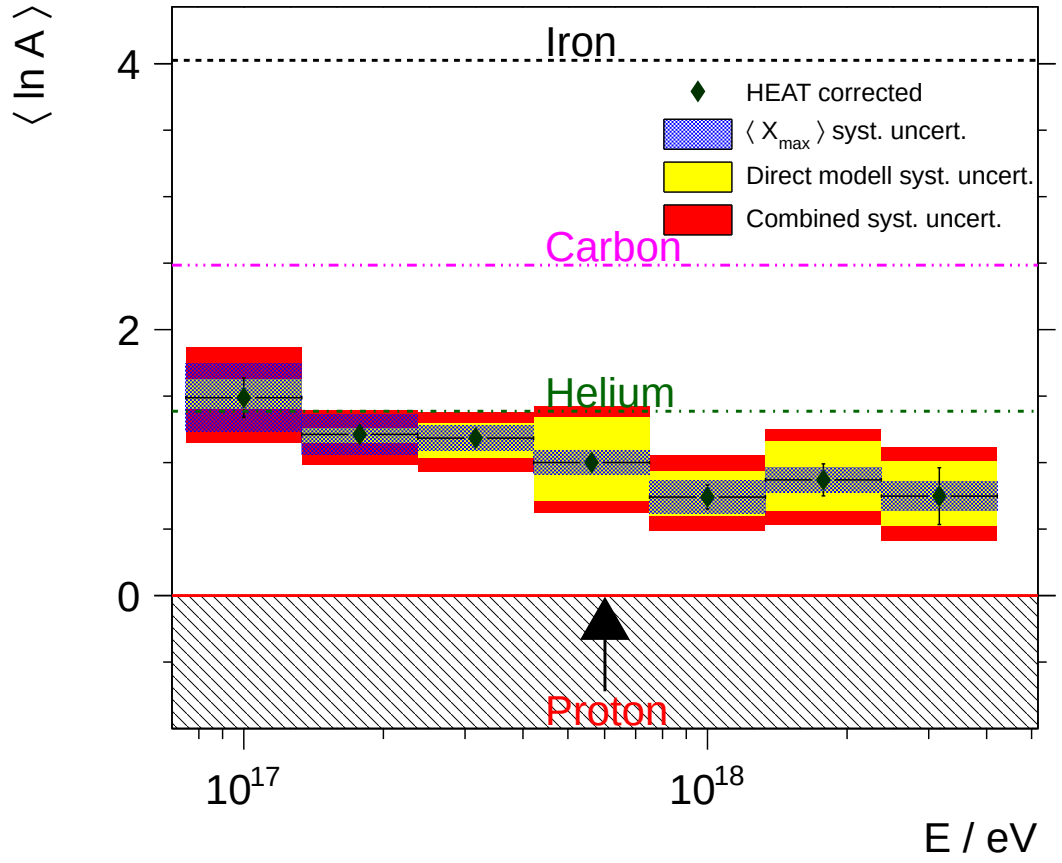

Figure 7.3.: Average logarithmic atomic mass number derived from $X_{\max}$ measurements (eqn. 7.1) as a function of energy. The blue shaded area shows the effect of the systematical uncertainty on the $\langle X_{\max} \rangle$ measurement. The yellow area denotes the systematical uncertainty arising from the differences between the hadronic interaction models. The red area shows the combined systematical uncertainty. Additionally, the expected values for a proton, helium, carbon and iron composition are marked.

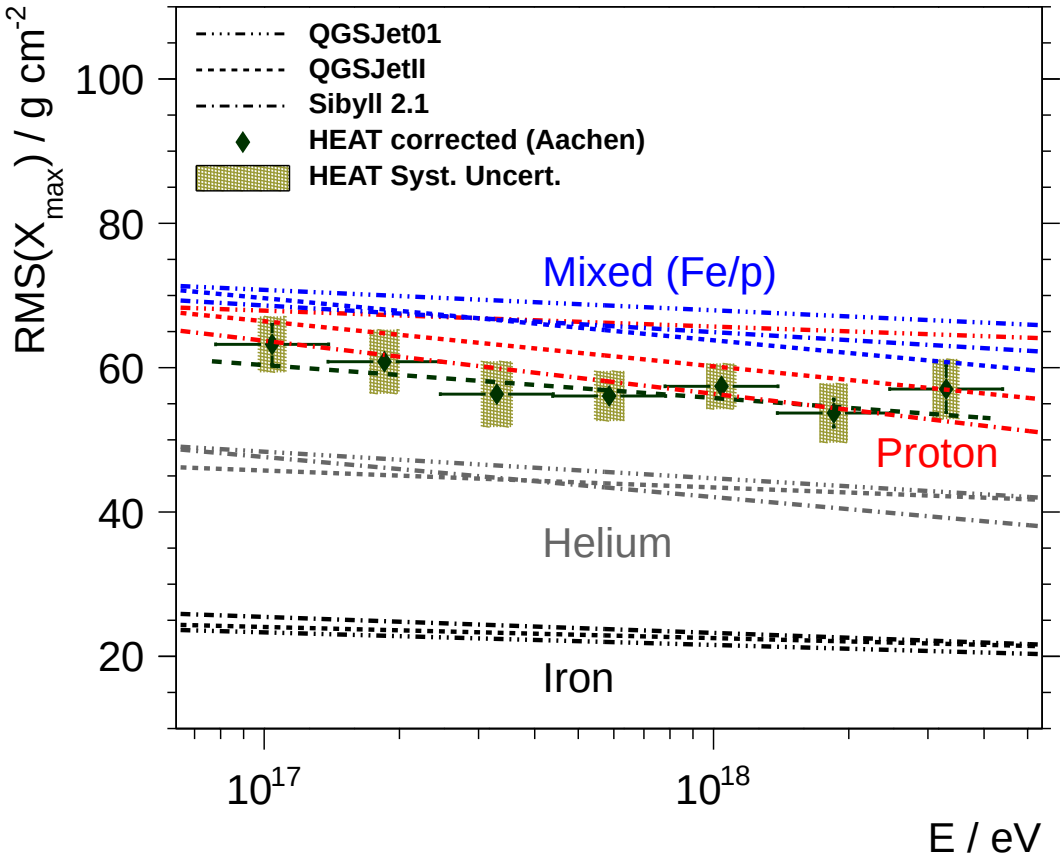

Figure 7.4.: Comparison of RMS(X_{max}) over energy with a composition of 50 % iron and 50 % proton primaries. Corrections for energy and RMS(X_{max}) mean bias from RealMC are applied. The horizontal bars denote the bin size. Vertical uncertainties denote the statistical uncertainty on the RMS(X_{max}) (incl. statistical uncertainty on original RMS($X_{\mathrm{max,rec,i}}$)). The shaded area denotes the systematical uncertainties derived from RealMC. The black long dashed lined through the data indicates the result of the fit of eqn. 6.2 on all energy bins.

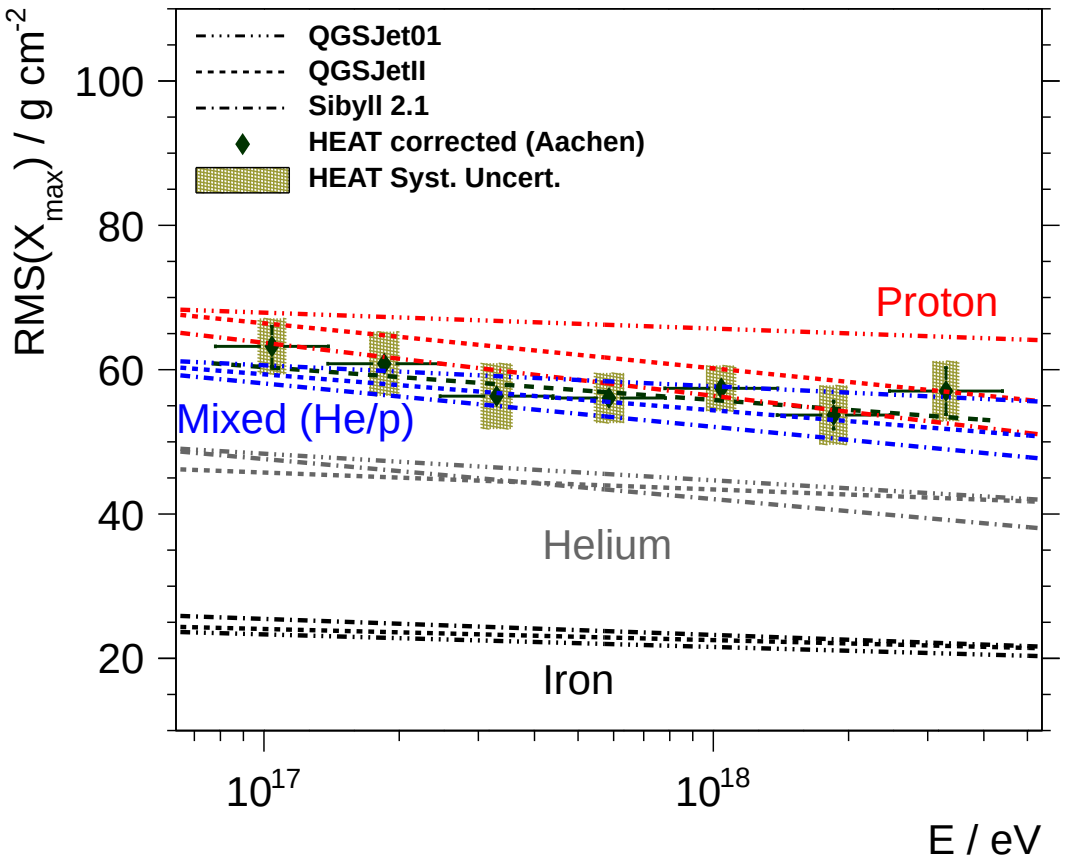

Figure 7.5.: Comparison of RMS(X_{max}) over energy with a composition of 50 % helium and 50 % proton primaries. Corrections for energy and RMS(X_{max}) mean bias from RealMC are applied. The horizontal bars denote the bin size. Vertical uncertainties denote the statistical uncertainty on the RMS(X_{max}) (incl. statistical uncertainty on original RMS($X_{\mathrm{max,rec,i}}$)). The shaded area denotes the systematical uncertainties derived from RealMC. The black long dashed lined through the data indicates the result of the fit of eqn. 6.2 on all energy bins.

At all energy bins, the data agrees with a proton-dominated composition at least within 3σ (statistically uncertainties). Due to the larger statistical uncertainty, the lowest energy bin at 10^{17} eV and the highest energy bin at $10^{18.5}$ eV show a good agreement with a mixed composition, too. A proton-dominated composition is included in the systematical uncertainties of all energy bins. Besides the observables $\langle X_{\mathrm{max}} \rangle$ and $\langle \ln A \rangle$, the RMS(X_{max}) does not show a compatibility with the helium induced EAS. But a comparison with a composition of 50 % helium and 50 % proton induced showers in fig. 7.5 shows a qualitatively good agreement (all data points agree within 1σ with the Monte Carlo predictions).

To recognize whether the RMS decreases or increases with increasing energy, eqn. 6.2 is fitted to the data. It results in a $\chi^2/N_{\mathrm{dof}} = 1.7$ with $P(\chi^2|N_{\mathrm{dof}}) = 0.14$. This good fit results can be expected due to the large uncertainties and can be visually confirmed. The slope is determined to $(-5 \pm 2)\,\mathrm{g\,cm^{-2}}$ and the offset is determined to $(14 \pm 3) \cdot 10\,\mathrm{g\,cm^{-2}}$. A comparison with the values determined from fits on the predictions of hadronic interaction models (presented in appendix D p. 109) shows a better agreement of the fitted slope with a proton dominated or mixed composition.

7.4. Astrophysical Interpretation

In the studied energy range from 10^{17} eV to 10^{18} eV the literature suggests a transition from cosmic rays originating from the Milky Way to those stemming from extragalactic sources.

A breakdown of the cosmic-ray flux, according to a model proposed by Hillas in 2004 [82], into the contributing primaries and their sources is shown in fig. 7.6. He checked the properties of particles accelerated in supernovae remnants (SNR) [83] and included the fluxes of different primaries, derived from KASCADE measurements, in his model. Beyond the KASCADE data he optimized the fluxes to be compatible with the measured energy spectrum.

According to Hillas' proposal and the KASCADE data, the galactic cosmic-ray spectrum is dominated by iron primaries above 10^{16} eV. At energies above $10^{17.2}$ eV an extragalactic component mainly consisting of proton and helium primaries dominates the cosmic ray flux.

Therefore, in Hillas' model a change in composition from heavier to lighter nuclei is expected to happen at $10^{17.2}$ eV. The presented analysis based on the combined HEAT and Coihueco data hints on a slightly heavier chemical composition in the energy range from $10^{16.88}$ eV to $10^{17.12}$ eV compatible with helium (cf. fig. 7.3) as well as a mixed composition of 50 % helium primaries and 50 % proton primaries (cf. fig. 7.4). With evolving energy, the measurement hints on a mass composition dominated by light nuclei.

Another model is proposed by Wibig and Wolfendale [84] which predicts a transition from a galactic to an extragalactic dominated cosmic ray flux in the energy range from 10^{18} eV to 10^{19} eV. As a consequence, the fraction of iron primaries is between 50 % and 80 % for energies between 10^{17} eV and 10^{18} eV. Beyond this energy range the fraction of iron primaries drops. This is not compatible with the presented measurement.

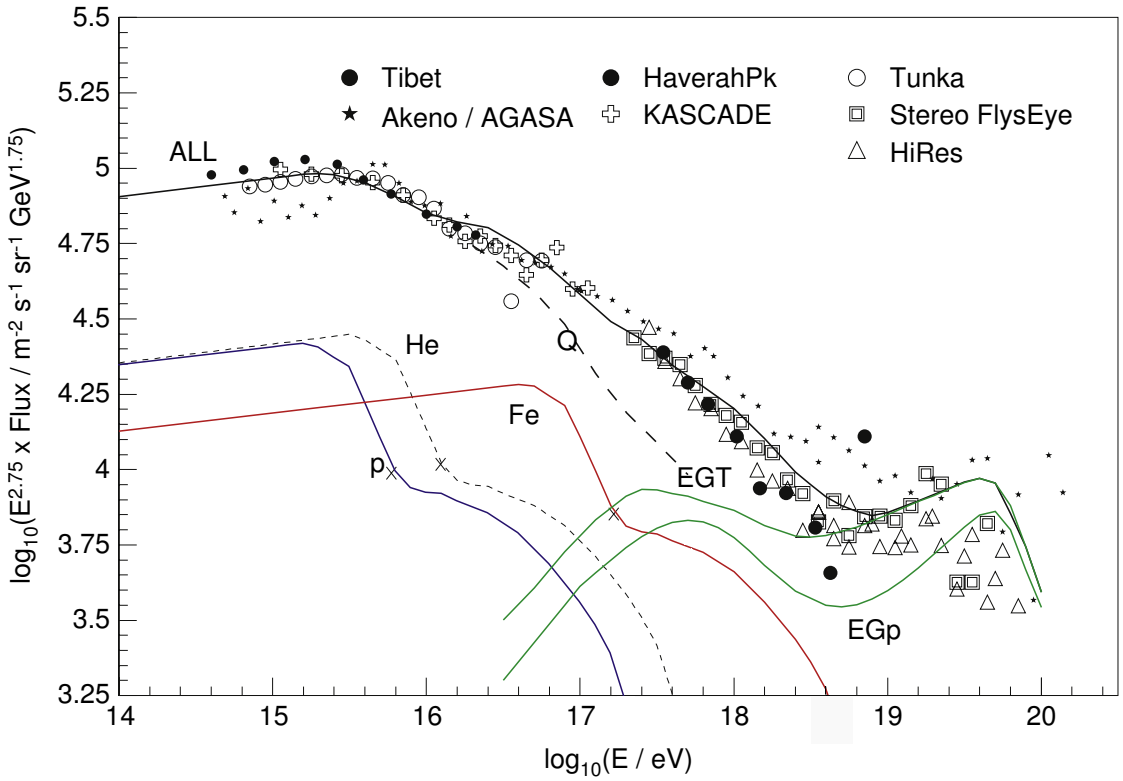

Figure 7.6.: Breakdown of the cosmic-ray energy spectrum from 10^{14} eV up to 10^{20} eV according to Hillas' model of the origin of ultra high energy cosmic-rays [82]. The galactic components (p, He and Fe) until the "x" marked points are shaped based on KASCADE data. Beyond the point they are optimized to fit the total observed flux. "All" denotes the total flux of all components. The dashed line denoted by "Q" is the sum of all fluxes without the extended tail of the galactic flux. "EGp" is the flux of extragalactic protons and "EGT" the total extragalactic flux. Modified plot from [8, 82].

8. Summary and Outlook

The analysis presented here is based on data taken with the low energy enhancement HEAT of the Pierre Auger Observatory. It extends the existing analysis of the cosmic ray mass composition above $10^{18}\,\mathrm{eV}$ down to $10^{17}\,\mathrm{eV}$. In the overlapping energy range from $10^{18}\,\mathrm{eV}$ to $10^{18.5}\,\mathrm{eV}$ of both analyses the data matches well within 2σ of statistical uncertainties. The analysed data favours a light composition for energies above $10^{17.25}\,\mathrm{eV}$ on. At lower energies a slightly heavier composition is preferred by the data.

As a preparatory work to the mass composition analysis, the uptime of HEAT was analyzed. The uptime fits well to those of the regular fluorescence detector. Besides it was shown that the stochastical reduction of the trigger rate, which was introduced to not saturate the communication system of the Pierre Auger Observatory with the higher trigger rate of HEAT, reduces the effective HEAT uptime by about 20 % as well as the number of recorded events, too.

Furthermore, an overview of the detector monitoring was given. It was shown, that according to the electronics monitoring differences between HEAT and the regular FD exists on the data acquisition level. Therefore, the Auger RealMC detector simulation, which uses the monitoring to describe the detector's dynamic, was used for this analysis. On a sample of about 5000 showers, differences between the dynamic RealMC simulations and the conventional static detector Monte Carlo were derived and presented.

The detector resolution and bias for the reconstructed energy and X_{max} were determined from about three million simulated showers in the energy range from $10^{17}\,\mathrm{eV}$ to $10^{18.5}\,\mathrm{eV}$. The detector simulations were performed with RealMC, for a combined detector geometry of HEAT and the regular fluorescence detector Coihueco. The detector resolution for the shower depth was determined to be about $(23 \pm 3)\,\mathrm{g\,cm^{-2}}$.

Based on the shower and detector simulations, a correction of the invisible energy based on the assumption of a mixed composition was applied. Furthermore, the X_{max} was corrected for the reconstruction bias. The X_{max} reconstruction bias depending on the primary energy was determined from the simulation to be between -6 and $0\,\mathrm{g\,cm^{-2}}$.

Outlook Since the absolute calibration of HEAT is still in progress and expected to be available soon, the detector is currently cross-calibrated with the regular fluorescence detector. Due to this fact, atmospheric monitoring data was not available, too. It is expected, that the final absolute calibration will be of no big effect. However, the consequently available atmospheric monitoring data, which are part of the detector simulation, are expected to have an impact on the determined bias. Furthermore, with the availability of atmospheric monitoring data, the event selection will be improved, too, because it allows to select only events with well-defined atmospheric conditions.

Another open challenge is the stochastic trigger rejection of HEAT events, because the trigger is no longer only driven by physical requirements, e.g. on the shower geometry. It is expected that within the next months (spring 2012), a new solution will be tested and deployed. Hopefully, the number of well reconstructible events will be increased.

A further possible extension is to extend the analysis to wholly include the SD simulation by using extensive air showers simulated with CORSIKA. Another improvement is to determine the bias arising from the telescopes' field of view on the X_{max} measurement and to reduce it.

The final goal is to enhance the applied analysis to smaller energy bins and extend it over the whole energy range of the Pierre Auger Observatory from 10^{17} eV to the highest energies around 10^{20} eV, and to include the shower depth sensitive quantities of the surface detector into the analysis, too.

Bibliography

[1] V. F. Hess, *Über Beobachtungen der durchdringenden Strahlung bei sieben Freiballonfahrten*, Z. Phys., 13 (1912), p. 1084.

[2] C. D. Anderson, *The positive electron*, Phys. Rev., 43 (1933), pp. 491–494, 10.1103/PhysRev.43.491.

[3] C. D. Anderson, *The apparent existence of easily deflectable positives*, Science, 76 (1932), pp. 238–239, http://www.sciencemag.org/content/76/1967/238.full.pdf, 10.1126/science.76.1967.238.

[4] C. M. G. Lattes, H. Muirhead, G. P. S. Occhialini, and C. F. Powell, *Processes Involving Charged Mesons*, Nature, 159 (1947), pp. 694–697, 10.1038/159694a0.

[5] P. Auger *et al.*, *Extensive cosmic ray showers*, Rev.Mod.Phys., 11 (1939), pp. 288–291, 10.1103/RevModPhys.11.288.

[6] J. Linsley, *Evidence for a Primary Cosmic-Ray Particle with Energy 10^{20} eV*, Physical Review Letters, 10 (1963), pp. 146–148, 10.1103/PhysRevLett.10.146.

[7] S. Corbat *et al.*, *Hires, a high resolution fly's eye detector*, Nuclear Physics B - Proceedings Supplements, 28 (1992), pp. 36 – 39, 10.1016/0920-5632(92)90106-3.

[8] J. Blümer, R. Engel, and J. R. Hörandel, *Cosmic rays from the knee to the highest energies*, Progress in Particle and Nuclear Physics, 63 (2009), pp. 293 – 338, 10.1016/j.ppnp.2009.05.002.

[9] W. Bothe and W. Kolhörster, *Das Wesen der Höhenstrahlung*, Zeitschrift für Physik, A Hadrons and Nuclei, 56 (1929), pp. 751–777, 10.1007/BF01340137. 10.1007/BF01340137.

[10] J. R. Hörandel, *On the knee in the energy spectrum of cosmic rays*, Astroparticle Physics, 19 (2003), pp. 193 – 220, 10.1016/S0927-6505(02)00198-6.

[11] J. A. Simpson, *Elemental and isotopic composition of the galactic cosmic rays*, Annual Review of Nuclear and Particle Science, 33 (1983), pp. 323–382, http://www.annualreviews.org/doi/pdf/10.1146/annurev.ns.33.120183.001543, 10.1146/annurev.ns.33.120183.001543.

[12] P. H. Fowler *et al.*, *Ariel 6 measurements of the fluxes of ultraheavy cosmic rays*, Astrophysical Journal, 314 (1987), pp. 739–746, 10.1086/165101.

[13] P. Fowler *et al.*, *High resolution study of nucleonic cosmic rays with $Z \geq 34$*, Nuclear Instruments and Methods, 147 (1977), pp. 195 – 199, 10.1016/0029-554X(77)90479-7.

[14] W. R. Binns *et al.*, *Abundances of ultraheavy elements in the cosmic radiation - Results from HEAO 3*, Astrophysical Journal, 346 (1989), pp. 997–1009, 10.1086/168082.

[15] E. K. Shirk and P. B. Price, *Charge and energy spectra of cosmic rays with Z greater than or approximately equal to 60 - The SKYLAB experiment*, Astrophysical Journal, 220 (1978), pp. 719–733, 10.1086/155955.

[16] D. Lawrence *et al.*, *Large-area scintillating-fiber time-of-flight/hodoscope detectors for particle astrophysics experiments*, Nuclear Instruments and Methods in Physics Research Section A: Accelerators, Spectrometers, Detectors and Associated Equipment, 420 (1999), pp. 402 – 415, 10.1016/S0168-9002(98)01164-4.

[17] B. A. Weaver and A. J. Westphal, *The Extended Analysis of the Trek Detector*, in International Cosmic Ray Conference, vol. 5 of International Cosmic Ray Conference, Aug. 2001, p. 1720.

[18] W. R. Binns *et al.*, *Cosmic-ray abundances of elements with atomic number 26 less than or equal to 40 measured on HEAO 3*, Astrophysical Journal Letters to the Editor, 247 (1981), pp. L115–L118, 10.1086/183602.

[19] J. Donnelly, *New Results on the Relative Abundance of Actinides in the Cosmic Radiation*, in International Cosmic Ray Conference, vol. 3 of International Cosmic Ray Conference, Aug. 1999, p. 109.

[20] K. Lodders, *Solar system abundances and condensation temperatures of the elements*, The Astrophysical Journal, 591 (2003), p. 1220.

[21] K. Greisen, *End to the cosmic-ray spectrum?*, Phys. Rev. Lett., 16 (1966), pp. 748–750, 10.1103/PhysRevLett.16.748.

[22] G. T. Zatsepin and V. A. Kuz'min, *Upper Limit of the Spectrum of Cosmic Rays*, Soviet Journal of Experimental and Theoretical Physics Letters, 4 (1966), p. 78.

[23] J. Abraham *et al.*, Pierre Auger Collaboration, *Observation of the suppression of the flux of cosmic rays above* $4 \times 10^{19} eV$, Phys.Rev.Lett., 101 (2008), p. 061101, `arXiv:astro-ph/0806.4302`, 10.1103/PhysRevLett.101.061101.

[24] R. Abbasi *et al.*, HiRes Collaboration, *First observation of the Greisen-Zatsepin-Kuzmin suppression*, Phys.Rev.Lett., 100 (2008), p. 101101, `arXiv:astro-ph/0703099`, 10.1103/PhysRevLett.100.101101.

[25] B. Peters, *Primary cosmic radiation and extensive air showers*, Il Nuovo Cimento (1955-1965), 22 (1961), pp. 800–819. 10.1007/BF02783106.

[26] R. D. Blandford and J. P. Ostriker, *Particle acceleration by astrophysical shocks*, The Astrophysical Journal Letters, 221 (1978), pp. L29–L32, 10.1086/182658.

[27] V. Berezinsky, M. Kachelriess, and A. Vilenkin, *Ultrahigh-energy cosmic rays without GZK cutoff*, Phys.Rev.Lett., 79 (1997), pp. 4302–4305, `arXiv:astro-ph/9708217`, 10.1103/PhysRevLett.79.4302.

[28] R. Aloisio, V. Berezinsky, and M. Kachelriess, *On the status of superheavy dark matter*, Phys.Rev., D74 (2006), p. 023516, arXiv:astro-ph/0604311, 10.1103/PhysRevD.74.023516.

[29] C. T. Hill, *Monopolonium*, Nucl.Phys., B224 (1983), p. 469, 10.1016/0550-3213(83)90386-3.

[30] P. M. Bauleo and J. R. Martino, *The dawn of the particle astronomy era in ultra-high-energy cosmic rays*, Nature, 458N7240 (2009), pp. 847–851, 10.1038/nature07948.

[31] H. J. Bhabha and W. Heitler, *The passage of fast electrons and the theory of cosmic showers*, Proceedings of the Royal Society of London. Series A - Mathematical and Physical Sciences, 159 (1937), pp. 432–458, 10.1098/rspa.1937.0082.

[32] J. and Matthews, *A heitler model of extensive air showers*, Astroparticle Physics, 22 (2005), pp. 387 – 397, 10.1016/j.astropartphys.2004.09.003.

[33] R. Ulrich, R. Engel, and M. Unger, *Hadronic multiparticle production at ultrahigh energies and extensive air showers*, Phys. Rev. D, 83 (2011), p. 054026, 10.1103/PhysRevD.83.054026.

[34] M. Risse, *Properties of extensive air showers*, Acta Phys. Polon., B35 (2004), pp. 1787–1798, astro-ph/0402300.

[35] J. Engel, T. K. Gaisser, P. Lipari, and T. Stanev, *Nucleus-nucleus collisions and interpretation of cosmic-ray cascades*, Phys. Rev. D, 46 (1992), pp. 5013–5025, 10.1103/PhysRevD.46.5013.

[36] T. Bergmann *et al.*, *One-dimensional hybrid approach to extensive air shower simulation*, Astropart. Phys., 26 (2007), pp. 420–432, astro-ph/0606564, 10.1016/j.astropartphys.2006.08.005.

[37] Klaus and Werner, *The hadronic interaction model epos*, Nuclear Physics B - Proceedings Supplements, 175-176 (2008), pp. 81 – 87, 10.1016/j.nuclphysbps.2007.10.012. ¡ce:title¿Proceedings of the XIV International Symposium on Very High Energy Cosmic Ray Interactions¡/ce:title¿.

[38] Auger Collaboration, *The pierre auger project design report*, (1996).

[39] J. Abraham *et al.*, *Properties and performance of the prototype instrument for the pierre auger observatory*, Nuclear Instruments and Methods in Physics Research Section A: Accelerators, Spectrometers, Detectors and Associated Equipment, 523 (2004), pp. 50 – 95, 10.1016/j.nima.2003.12.012.

[40] J. Abraham *et al.*, *The fluorescence detector of the pierre auger observatory*, Nuclear Instruments and Methods in Physics Research Section A: Accelerators, Spectrometers, Detectors and Associated Equipment, 620 (2010), pp. 227 – 251, 10.1016/j.nima.2010.04.023.

[41] J. A. Abraham *et al.*, The Pierre Auger Collaboration, *Operations of and Future Plans for the Pierre Auger Observatory*, (2009), arXiv:0906.2354.

[42] B. G. Keilhauer, *Investigation of atmospheric effects on the development of extensive air showers and their detection with the Pierre Auger Observatory*, PhD thesis, 2004. Hardcopy at DESY.

[43] J. Abraham *et al.*, Pierre Auger Observatory Collaoration, *Trigger and aperture of the surface detector array of the Pierre Auger Observatory*, Nucl.Instrum.Meth., A613 (2010), pp. 29–39, 10.1016/j.nima.2009.11.018.

[44] F. Arqueros, J. Hörandel, and B. Keilhauer, *Air fluorescence relevant for cosmic-ray detection, Summary of the 5th fluorescence workshop, El Escorial 2007*, Nuclear Instruments and Methods in Physics Research Section A: Accelerators, Spectrometers, Detectors and Associated Equipment, 597 (2008), pp. 1 – 22, 10.1016/j.nima.2008.08.056. Proceedings of the 5th Fluorescence Workshop.

[45] S. Argiro *et al.*, *The Offline framework of the Pierre Auger Observatory*, Nucl. Instr. and Meth., A580 (2007), pp. 1485–1496.

[46] W3.org, *XML 1.0 Specification*, 2008.

[47] D. Kümpel, *Geometry Reconstruction of Fluorescence Detectors Revisited*, Auger Internal Notes, 99 (2007).

[48] P. Younk and B. Fick, *On SDP Reconstruction Accuracy*, Auger Internal Notes, 86 (2006).

[49] $\overline{\text{Off}}\underline{\text{line}}$, *Modules/FdReconstruction/FdSDPFinderOG/FdSDPFinder.cc*, SVN-Trunk rev. 18737.

[50] T. Gaisser and A. Hillas, *Reliability of the method of constant intensity cuts for reconstructing the average development of vertical showers*, Proceedings of the 15th International Cosmic Ray Conference, 8 (1977), p. 353.

[51] R. Engel, Pierre Auger Collaboration, *Some comments on the energy scale of the pierre auger observatory*, AIP Conference Proceedings, 1367 (2011), pp. 50–53, 10.1063/1.3628714.

[52] T. P. et al., *Dependence of the longitudinal shower profile on the characteristics of hadronic multiparticle production*, Proc. 29th Int. Cosmic Ray Conf., 7 (2005), p. 103.

[53] H. M. Barbosa, F. Catalani, J. Chinellato, and C. Dobrigkeit, *Determination of the calorimetric energy in extensive air showers*, Astropart.Phys., 22 (2004), pp. 159–166, `arXiv:astro-ph/0310234`, 10.1016/j.astropartphys.2004.06.007.

[54] The Pierre Auger Collaboration, *The Pierre Auger Observatory V: Enhancements*, (2011), `arXiv:1107.4807`. * Temporary entry *.

[55] J. C. de No, M. Leuthold, and T. Hebbeker, *Monitoring of camera positions for Auger Fluorescence Telescopes*, Auger Internal Notes, 100 (2008).

[56] S. Falk *et al.*, *A First Look at HEAT Data*, Auger Internal Notes, 123 (2010).

[57] A. Tripathi *et al.*, *The Offline SD Calibration and Monitoring Database in the DPA Framework*, Auger Internal Notes, 39 (2004).

[58] J. Bohacova *et al.*, *Fluorescence detector uptime fraction calculation*, Auger Internal Notes, 71 (2007).

[59] M. Kleifges, A. Menshikov, D. Tchermakhovski, and H. Gemmeke, *Statistical current monitor for the cosmic ray experiment pierre auger*, in Nuclear Science Symposium Conference Record, 2002 IEEE, vol. 1, nov. 2002, pp. 62 – 65 vol.1, 10.1109/NSSMIC.2002.1239269.

[60] A. Menshikov, M. Kleifges, and H. Gemmeke, *Fast gain calibration of photomultiplier and electronics*, IEEE Trans.Nucl.Sci., 50 (2003), pp. 1208–1213, 10.1109/TNS.2003.815344.

[61] D. V. Camin, V. Grassi, F. Snchez, and V. Scherini, *Tracking stars with the fluorescence detector of the pierre auger observatory*, Nuclear Instruments and Methods in Physics Research Section A: Accelerators, Spectrometers, Detectors and Associated Equipment, 518 (2004), pp. 177 – 179, 10.1016/j.nima.2003.10.053. ¡ce:title¿Frontier Detectors for Frontier Physics: Proceedin¡/ce:title¿.

[62] C. De Donato *et al.*, *Using star tracks to determine the absolute pointing of the Fluorescence Detector telescopes*, Auger Internal Notes, 008 (2005).

[63] M. Prouza *et al.*, *Star tracking using background data of FD telescopes*, Auger Internal Notes, 041 (2005).

[64] A. Newman *et al.*, *Night sky brightness variations determined from FD background data*, Auger Internal Notes, 90 (2006).

[65] N. Scharf, *The Spectrum of Cosmic Rays detected with the HEAT extension at the Pierre Auger Observatory*, PhD thesis, RWTH Aachen University, 2011.

[66] D. Heck *et al.*, *Corsika: A monte carlo code to simulate extensive air showers*, Wissenschaftliche Berichte FZKA, 6019 (1998), pp. 1–90.

[67] D. Heck and J. Knapp, *Upgrade of the Monte Carlo code CORSIKA to simulate extensive air showers with energies* $\geq 10^{20}\,eV$, Wissenschaftliche Berichte FZKA, (1998).

[68] R. Brun and F. Rademakers, *Root an object oriented data analysis framework*, Nuclear Instruments and Methods in Physics Research Section A: Accelerators, Spectrometers, Detectors and Associated Equipment, 389 (1997), pp. 81 – 86, 10.1016/S0168-9002(97)00048-X. New Computing Techniques in Physics Research V.

[69] R. S. Fletcher, T. K. Gaisser, P. Lipari, and T. Stanev, *sibyll: An event generator for simulation of high energy cosmic ray cascades*, Phys. Rev. D, 50 (1994), pp. 5710–5731, 10.1103/PhysRevD.50.5710.

[70] S. Ostapchenko, *Nonlinear screening effects in high energy hadronic interactions*, Phys. Rev. D, 74 (2006), p. 014026, 10.1103/PhysRevD.74.014026.

[71] S. and Ostapchenko, *On the re-summation of enhanced pomeron diagrams*, Physics Letters B, 636 (2006), pp. 40 – 45, 10.1016/j.physletb.2006.03.026.

[72] L. P. Jr. *et al.*, *Simulation of the fluorescence detector of the pierre auger observatory*, Nuclear Instruments and Methods in Physics Research Section A: Accelerators, Spectrometers, Detectors and Associated Equipment, 545 (2005), pp. 632 – 642, 10.1016/j.nima.2005.01.346.

[73] R. Ulrich *et al.*, *Ultra-fast hybrid simulations with* `SdSimpleSim`, Auger Internal Notes, 61 (2008).

[74] *Mathematical tools or statistics, monte carlo, group theory*, Physics Letters B, 667 (2008), pp. 316 – 339, 10.1016/j.physletb.2008.07.030. Review of Particle Physics.

[75] E. J. Ahn *et al.*, *Measurement of the Depth of Shower Maximum of Cosmic Rays above 1 EeV*, Auger Internal Notes, 78 (2009).

[76] B. Dawson and P. Sommers, The Pierre Auger Collaboration, *The hybrid aperture and precision of the auger observatory*, 714 (2001).

[77] J. Bellido, *Systematic in the Reconstructed X_{max} as a function of the Observed Profile Length*. Talk at the Auger Analysis Meeting, Chicago, September 2006.

[78] J. Matthews, *A Heitler model of extensive air showers*, Astropart.Phys., 22 (2005), pp. 387–397, 10.1016/j.astropartphys.2004.09.003.

[79] M. Settimo *et al.*, *Parameterisation of the "Lateral Trigger Probability" functions at low energies* , Auger Internal Notes, 69 (2007).

[80] N. N. Kalmykov and S. S. Ostapchenko, *The nucleus-nucleus interaction, nuclear fragmentation, and fluctuations of extensive air showers*, Physics of Atomic Nuclei, 56 (1993), pp. 346–353.

[81] N. Kalmykov, S. Ostapchenko, and A. Pavlov, *Quark-gluon string model and EAS simulation problems at ultra-high energies*, Nucl.Phys.Proc.Suppl., 52B (1997), pp. 17–28.

[82] A. Hillas, *Where do 10^{19} eV cosmic rays come from?*, Nuclear Physics B - Proceedings Supplements, 136 (2004), pp. 139 – 146, 10.1016/j.nuclphysbps.2004.10.004. CRIS 2004 Proceedings of the Cosmic Ray International Seminars: GZK and Surroundings.

[83] A. M. Hillas, *Can diffusive shock acceleration in supernova remnants account for high-energy galactic cosmic rays?*, Journal of Physics G: Nuclear and Particle Physics, 31 (2005), p. R95.

[84] T. Wibig and A. W. Wolfendale, *At what particle energy do extragalactic cosmic rays start to predominate?*, Journal of Physics G: Nuclear and Particle Physics, 31 (2005), p. 255.

Appendix A.

Offline Steering Cards

A.1. HEAT Data Reconstruction

ModuleSequence.xml:

```
<sequenceFile>

   <enableTiming/>
   <enableModuleTracing/>
   <moduleControl>

    <loop numTimes="unbounded">
      <module> EventFileReaderOG         </module>
      <try>
              <loop numTimes="1">
                <module> SdCalibratorOG            </module>
                <module> SdSignalRecoveryKLT         </module>
              </loop>
      </try>

      <loop numTimes="1">
        <module> FdCalibratorOG            </module>
        <module> FdEyeMergerKG             </module>
        <module> FdPulseFinderOG           </module>
        <module> FdSDPFinderOG             </module>
        <module> FdAxisFinderOG            </module>
        <module> HybridGeometryFinderOG    </module>
        <module> HybridGeometryFinderWG    </module>
        <module> FdApertureLightKG         </module>
        <module> FdEnergyDepositFinderKG   </module>
      </loop>

      <try>
         <module> SdEventSelectorOG         </module>
         <module> SdPlaneFitOG              </module>
         <module> LDFFinderKG               </module>
         <module> SdEventPosteriorSelectorOG </module>
      </try>

      <module> RecDataWriterNG               </module>
```

```
    </loop>

   </moduleControl>
</sequenceFile>
```

A.2. HEAT Simulation And Reconstruction

ModuleSequence.xml:

```
<sequenceFile>
  <enableTiming/>

  <moduleControl>

    <loop numTimes="NEVENTS" pushEventToStack="yes">
      <try>
        <module> EventFileReaderOG </module>
        <module> MCShowerCheckerOG </module>
      </try>

      <loop numTimes="1" pushEventToStack="yes">
        <module> EventGeneratorOG </module>

        <!-- SD Simulation -->
        <try>
          <module> SdSimpleSimKG </module>
        </try>

        <!-- FD Simulation -->
        <try>
          <module> FdSimEventCheckerOG </module>
          <module> ShowerLightSimulatorKG </module>
          <module> LightAtDiaphragmSimulatorKG </module>
          <module> ShowerPhotonGeneratorOG </module>
          <module> TelescopeSimulatorKG </module>
          <module> FdBackgroundSimulatorOG </module>
          <module> FdElectronicsSimulatorOG </module>
          <module> FdTriggerSimulatorOG </module>

          <!-- Trigger and Event builder -->
          <module> CentralTriggerSimulatorXb </module>
          <module> CentralTriggerEventBuilderOG </module>
          <module> EventBuilderOG </module>

          <!-- export simulation in offline format -->
          <module> EventFileExporterOG </module>

          <!-- run event reconstrution -->
          <try>
            <try>
```

```
            <module> SdCalibratorOG            </module>
            <module> SdSignalRecoveryKLT         </module>
          </try>

          <!-- FD reconstruction -->
          <try>
            <module> FdCalibratorOG            </module>
            <module> FdEyeMergerKG             </module>
            <module> FdPulseFinderOG           </module>
            <module> FdSDPFinderOG             </module>
            <module> FdAxisFinderOG            </module>
            <module> HybridGeometryFinderOG    </module>
            <module> HybridGeometryFinderWG    </module>
            <module> FdApertureLightKG         </module>
            <module> FdEnergyDepositFinderKG   </module>
          </try>

          <!-- SD reconstruction -->
          <try>
            <module> SdEventSelectorOG         </module>
            <module> SdPlaneFitOG              </module>
            <module> LDFFinderKG               </module>
            <module> SdEventPosteriorSelectorOG </module>
          </try>

        </try>
      </try>
      <try>
            <module> RecDataWriterNG              </module>
      </try>
    </loop>
  </loop>
 </moduleControl>
</sequenceFile>
```

Appendix B.

Data Selection

B.1. Cuts Applied To HEAT Data

The following cuts are based on the suggestions from [56].

```
heatOrientationUp

eyeCut 100000 # CoHe only

# # geometry related cuts
minLgEnergyFD 15.0
maxCoreTankDist  1500.  # maximum shower plane distance core-hybrid-tank
nAxisPixels         5   # min number of pixels used in axis fit

# profile related cuts
xMaxInFOV           0.0 # max distance of xMax to borders
xMaxError          40.0 # max error on xMax [g/cm^2]
energyError          .2 # max error on energy (relative)
profileChi2         1.6 # max reduced GH chi2
minViewAngle        20. # minimum viewing angle
maxDepthHole        30. # maximum hole in profile (% of track length)

skipSaturated
!badPixels      1
maxZenithFD     60.

# at least hybrid trigger probability of
#    90% for proton and
#    90% for iron and
# >=  5% difference in trigger probability
brassHybridProb 0.9 0.9 0.05
```

Appendix C.

Fluorescence Detector Monitoring

C.1. ADC Variances Distribution

Distribution of ADC variances in the HEAT and Coihueco telescopes. One can see that for both the most time the ADC variances are below 100. Both show a strong decline to higher variances. On the other hand at HEAT also several local maxima exists up to about a value of 4000.

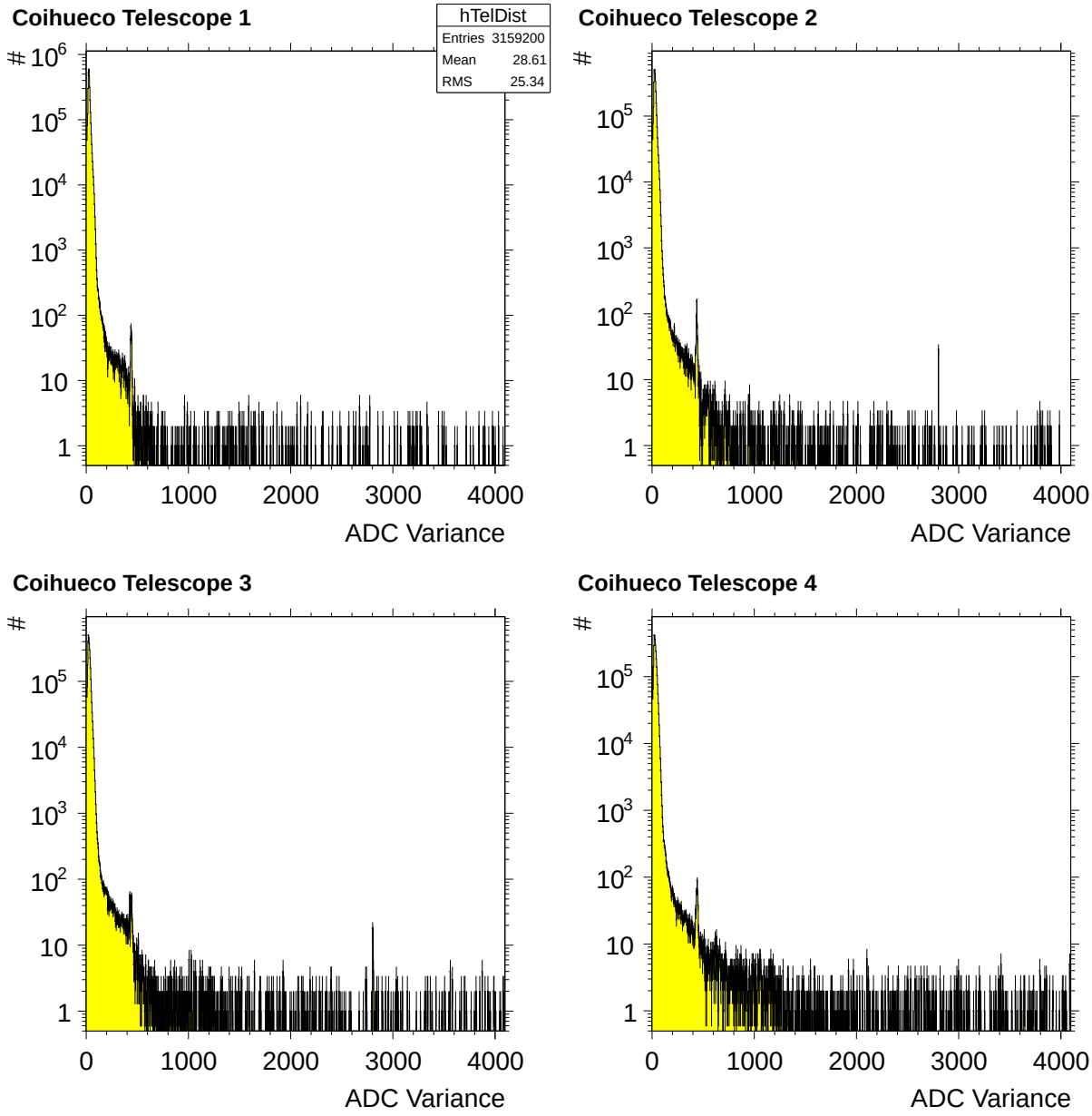

Coihueco Telescope 5

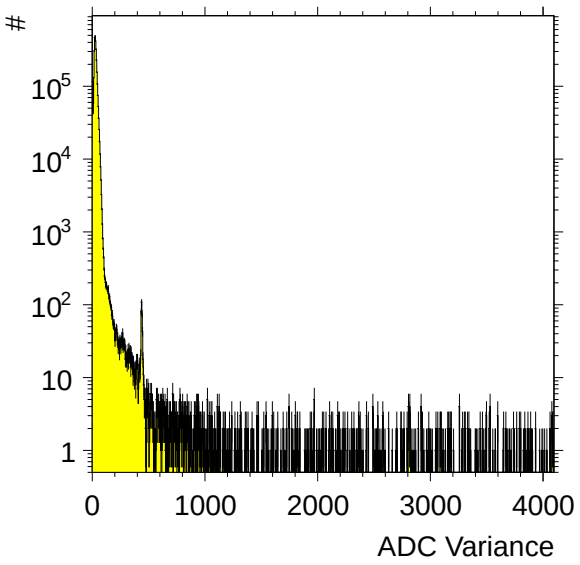

Coihueco Telescope 6

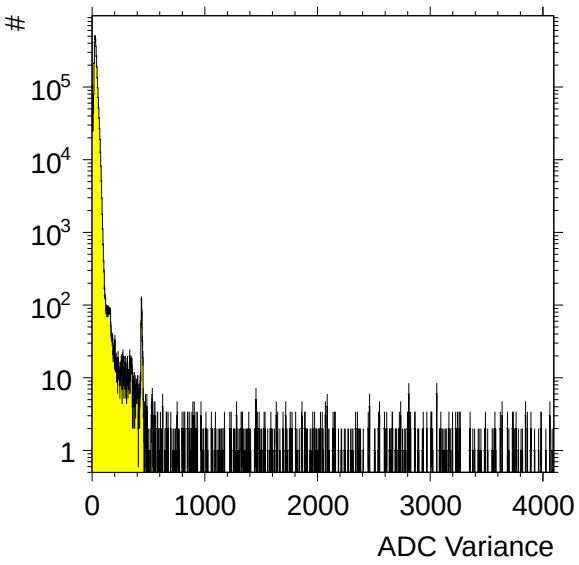

HEAT Telescope 1

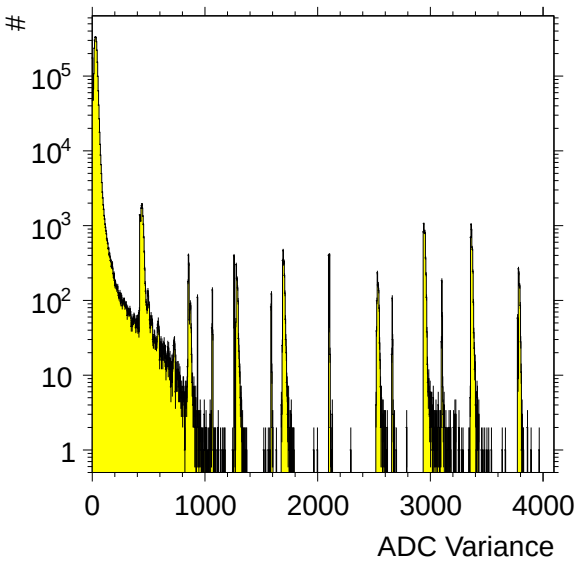

HEAT Telescope 2

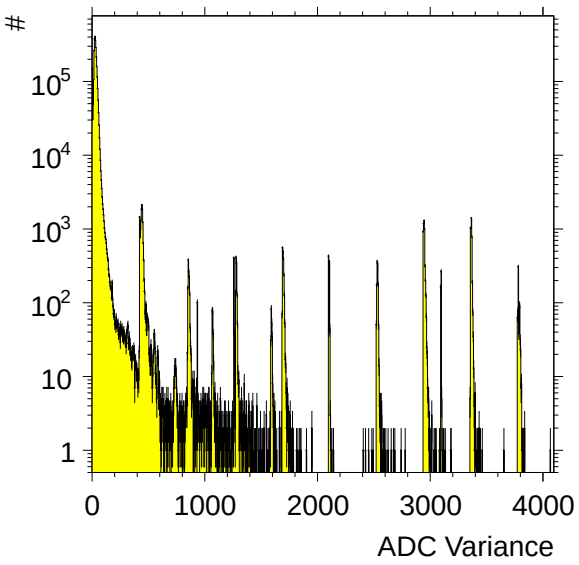

HEAT Telescope 3

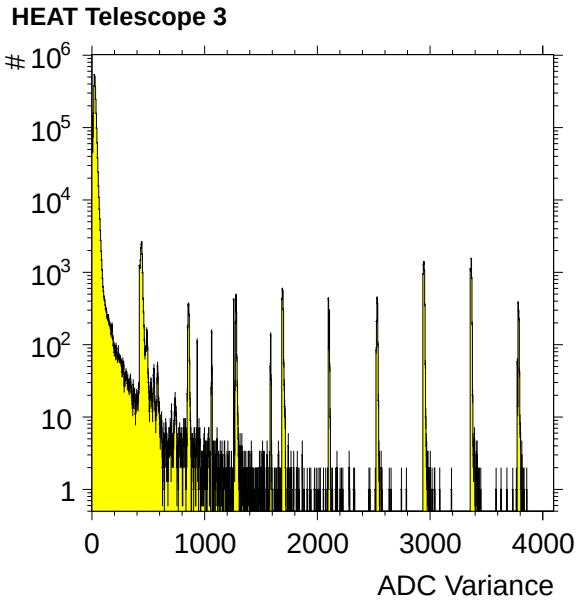

C.2. Limits of ADC Variances Quantiles

On the horizontal axis the pixel id in the telescopes is depicted. The vertical axis shows the highest ADC variances observed in the lower 95 % / 99 % of the monitored time. For Coihueco one can see, that for the 95 % quantile the limits are spread around between 30 and 80 ADC counts, which fits well to the mean ADC variances per month. The limit for the 99 % quantile increases on average by a factor of two. Some pixels show an increase of up to a factor of 5.

For HEAT one can see, that this limit is about the mean for the 95 % quantile and increases on average by a factor of 5 for the 99 % quantile. But there are also pixels in which the increase is about a factor of 20 from the 95 % to 99 % quantile.

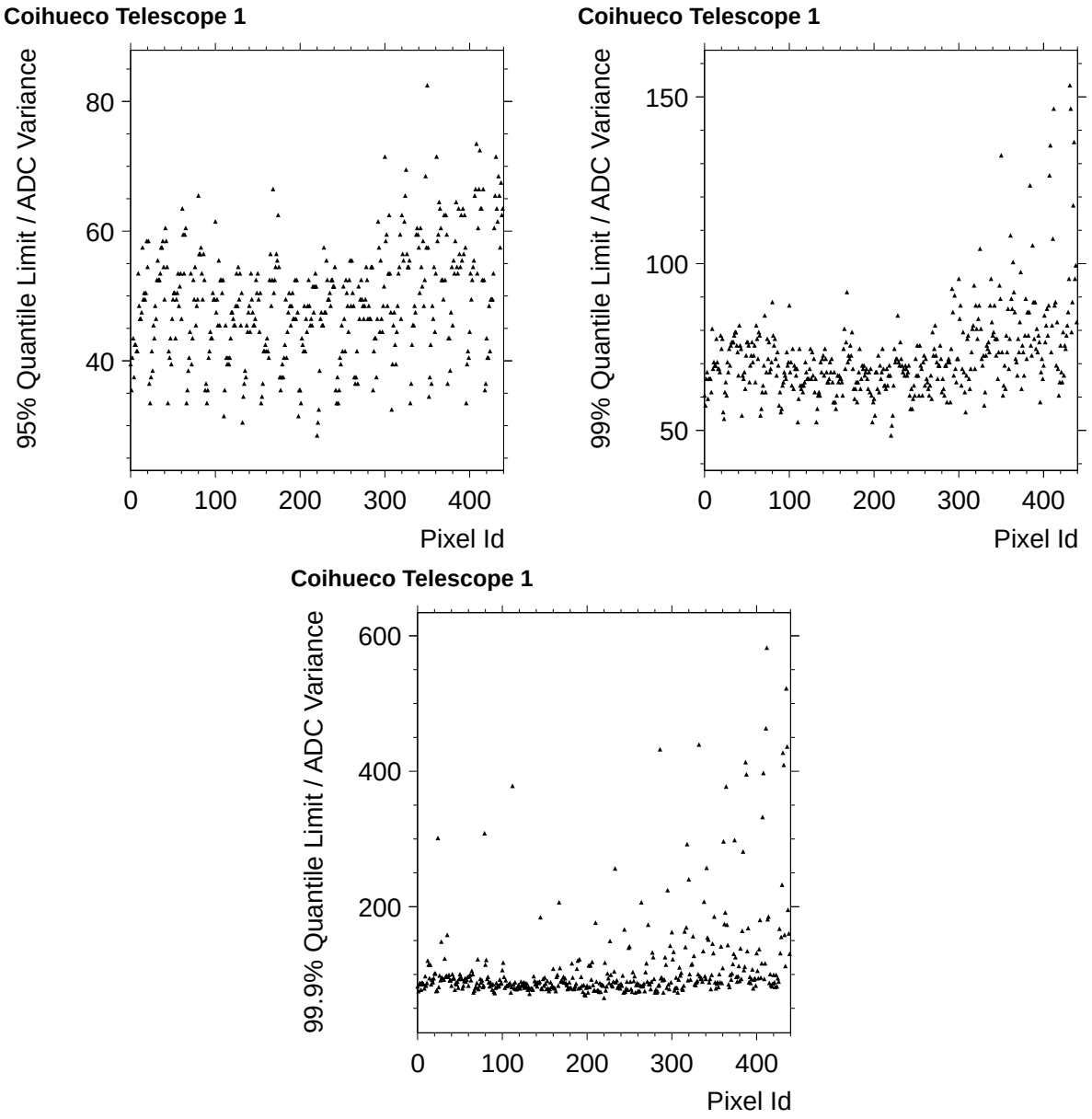

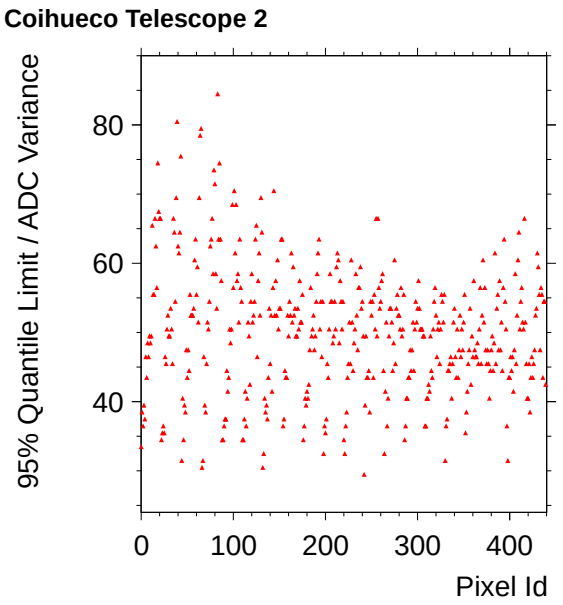
Coihueco Telescope 2
95% Quantile Limit / ADC Variance
80
60
40
0
100
200
300
400
Pixel Id

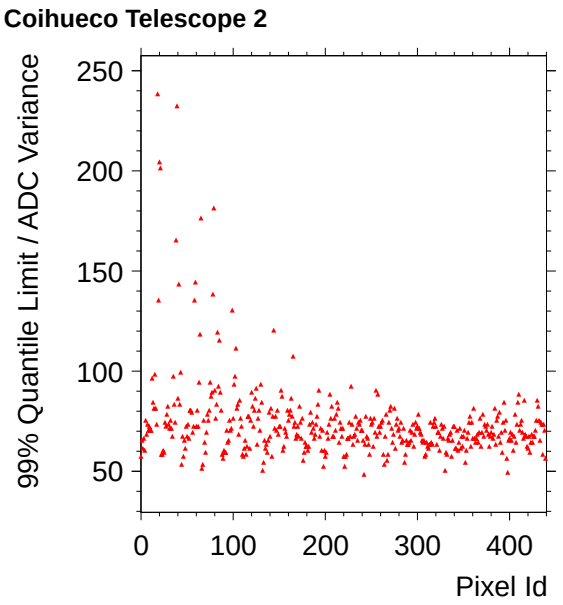
Coihueco Telescope 2
99% Quantile Limit / ADC Variance
250
200
150
100
50
0
100
200
300
400
Pixel Id

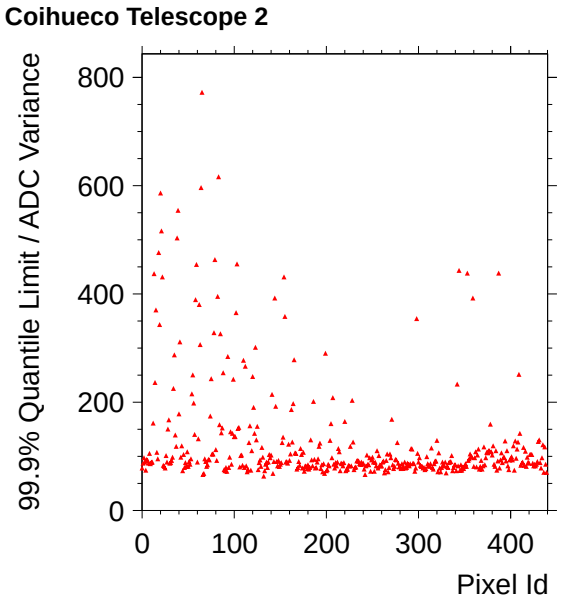
Coihueco Telescope 2
99.9% Quantile Limit / ADC Variance
800
600
400
200
0
0
100
200
300
400
Pixel Id

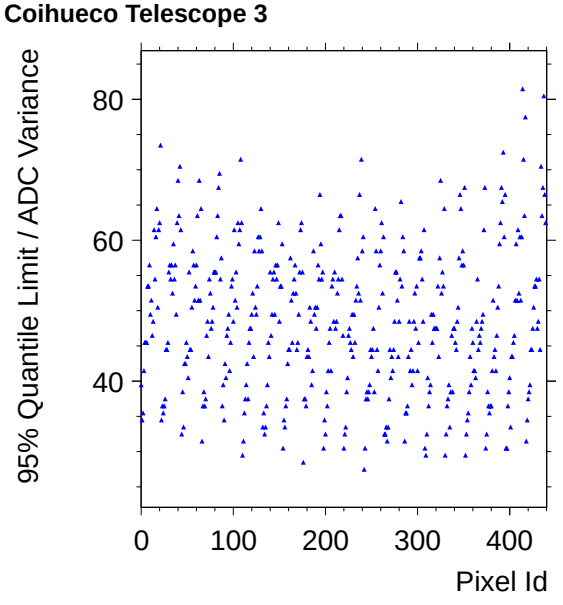
Coihueco Telescope 3
95% Quantile Limit / ADC Variance
80
60
40
0
100
200
300
400
Pixel Id

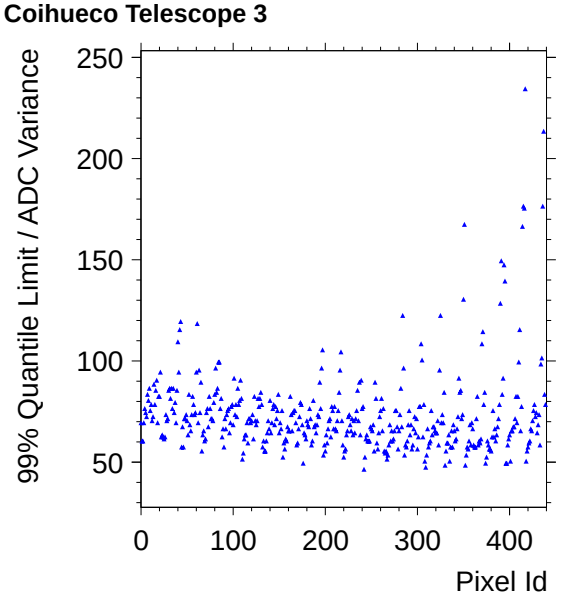
Coihueco Telescope 3
99% Quantile Limit / ADC Variance
250
200
150
100
50
0
100
200
300
400
Pixel Id

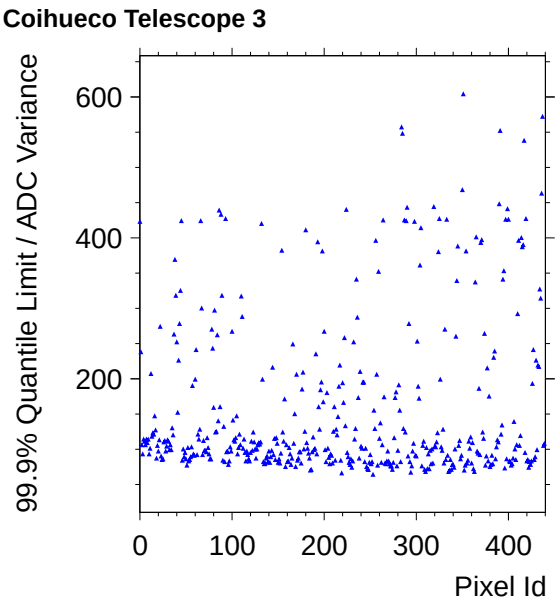
Coihueco Telescope 3
99.9% Quantile Limit / ADC Variance
600
400
200
0
100
200
300
400
Pixel Id

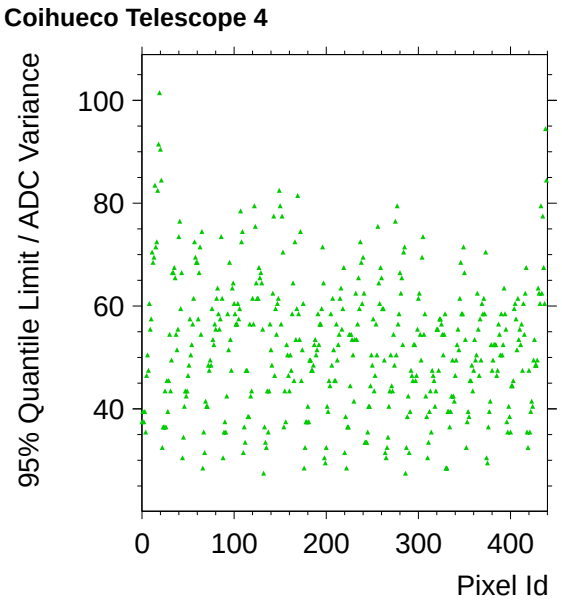
Coihueco Telescope 4
95% Quantile Limit / ADC Variance
100
80
60
40
0
100
200
300
400
Pixel Id

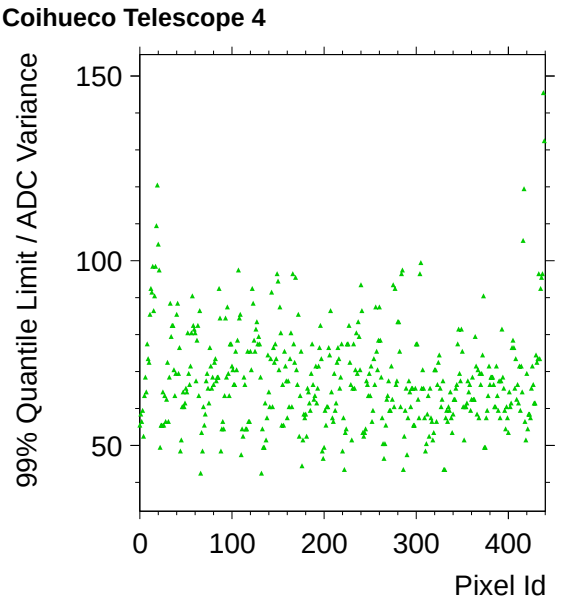
Coihueco Telescope 4
99% Quantile Limit / ADC Variance
150
100
50
0
100
200
300
400
Pixel Id

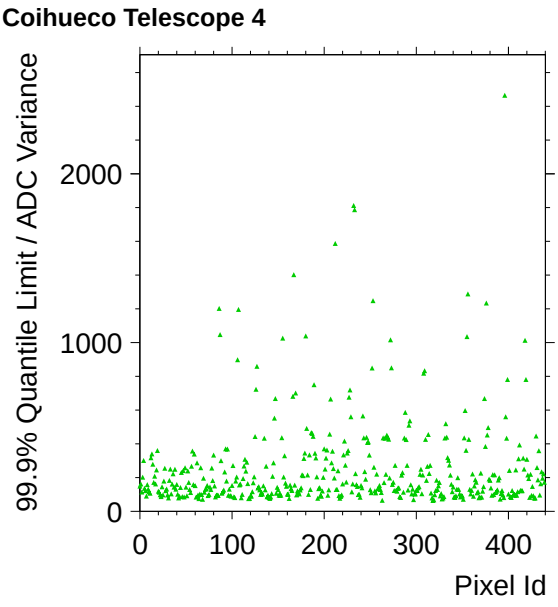
Coihueco Telescope 4
99.9% Quantile Limit / ADC Variance
2000
1000
0
0
100
200
300
400
Pixel Id

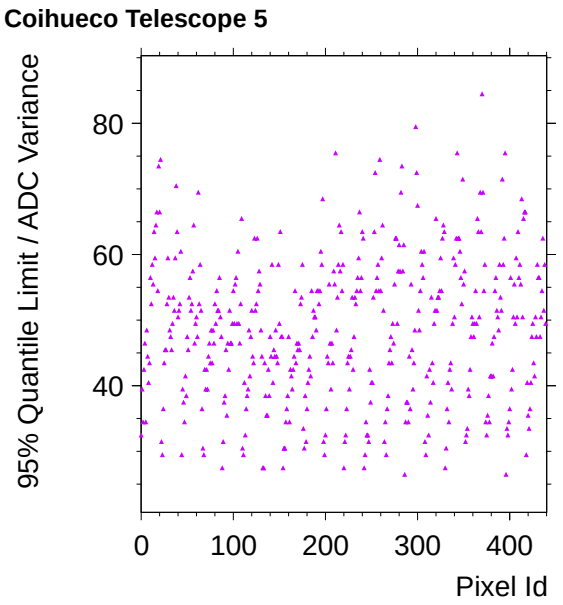
Coihueco Telescope 5
95% Quantile Limit / ADC Variance
80
60
40
0
100
200
300
400
Pixel Id

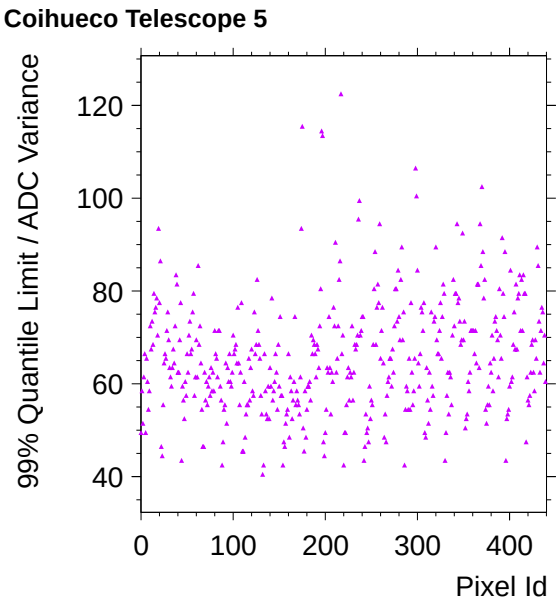
Coihueco Telescope 5
99% Quantile Limit / ADC Variance
120
100
80
60
40
0
100
200
300
400
Pixel Id

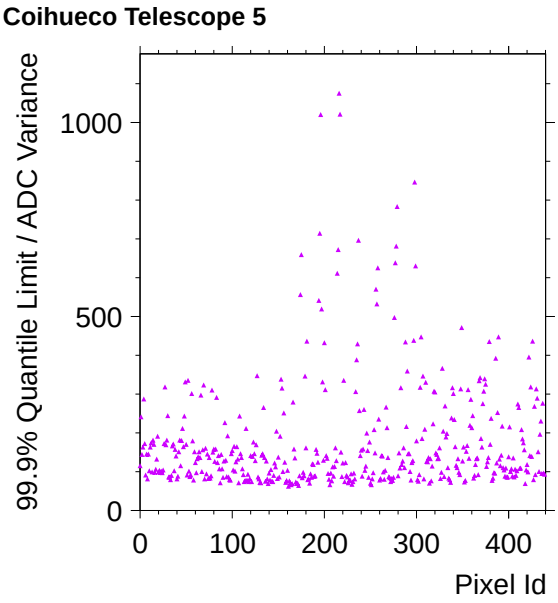
Coihueco Telescope 5
99.9% Quantile Limit / ADC Variance
1000
500
0
0
100
200
300
400
Pixel Id

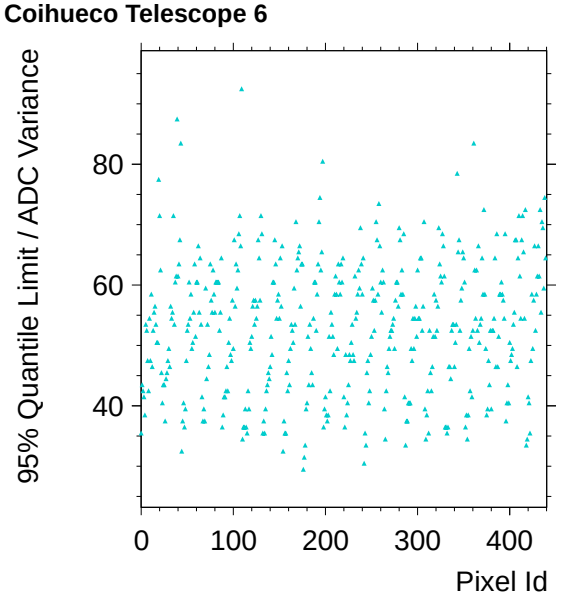
Coihueco Telescope 6
95% Quantile Limit / ADC Variance
80
60
40
0
100
200
300
400
Pixel Id

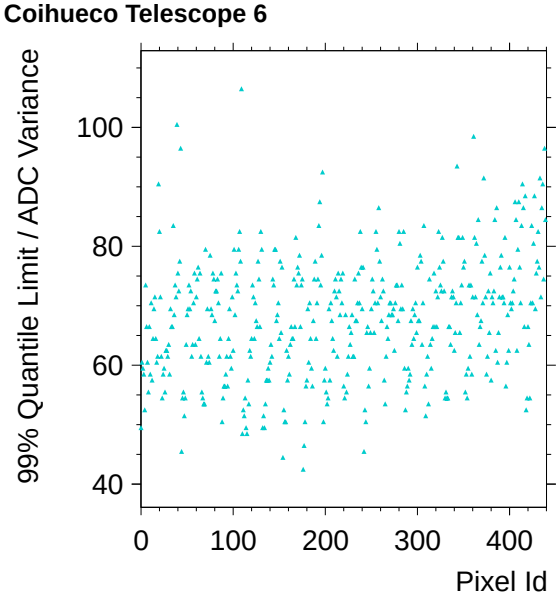
Coihueco Telescope 6
99% Quantile Limit / ADC Variance
100
80
60
40
0
100
200
300
400
Pixel Id

Coihueco Telescope 6

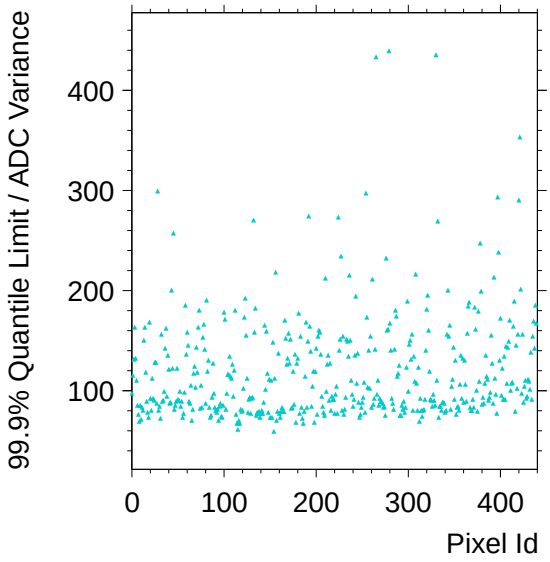

HEAT Telescope 1

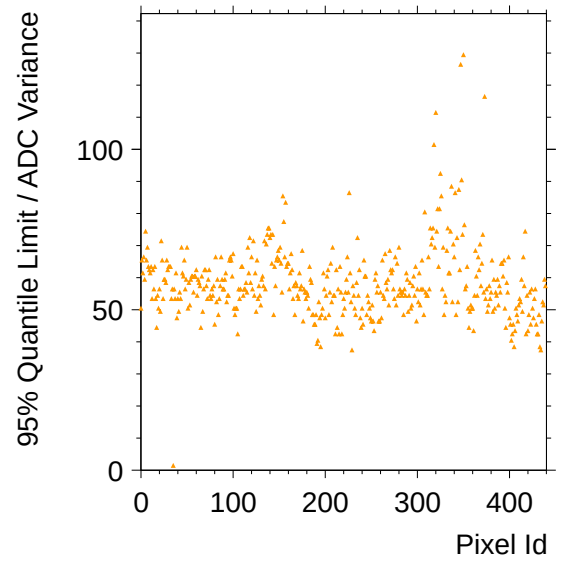

HEAT Telescope 1

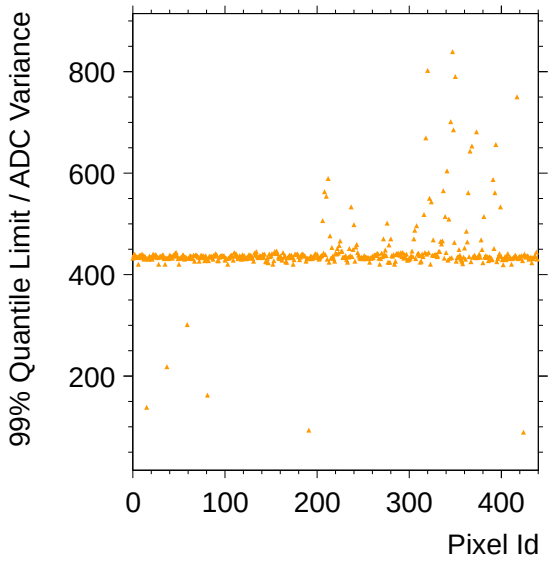

HEAT Telescope 1

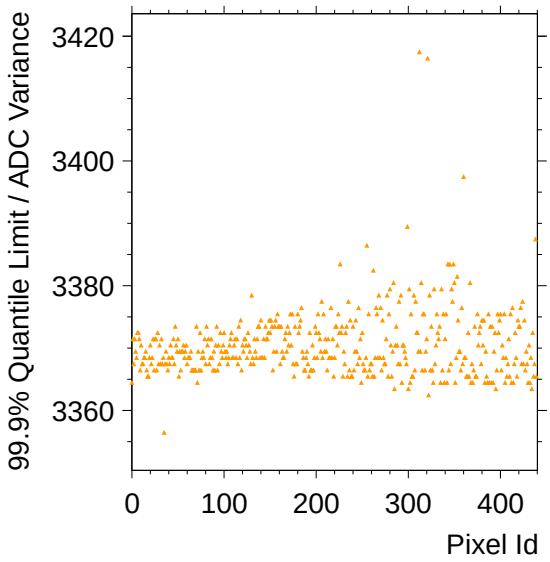

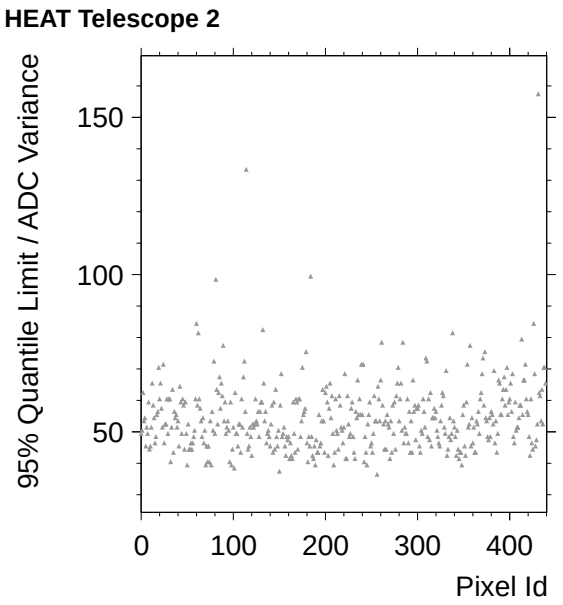
HEAT Telescope 2
95% Quantile Limit / ADC Variance
150
100
50
0
100
200
300
400
Pixel Id

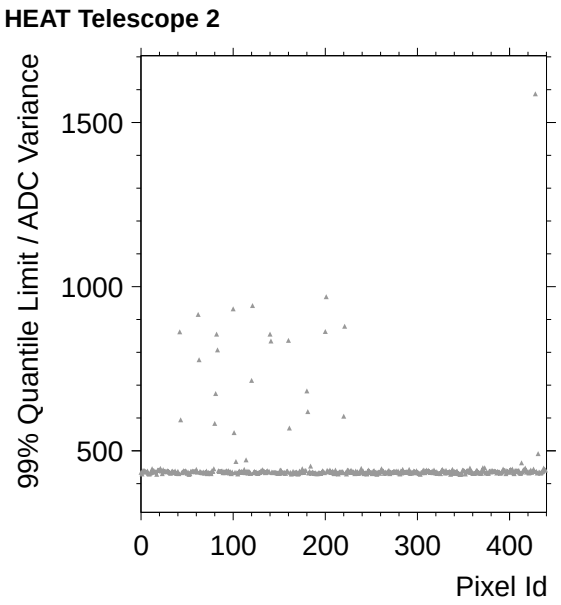
HEAT Telescope 2
99% Quantile Limit / ADC Variance
1500
1000
500
0
100
200
300
400
Pixel Id

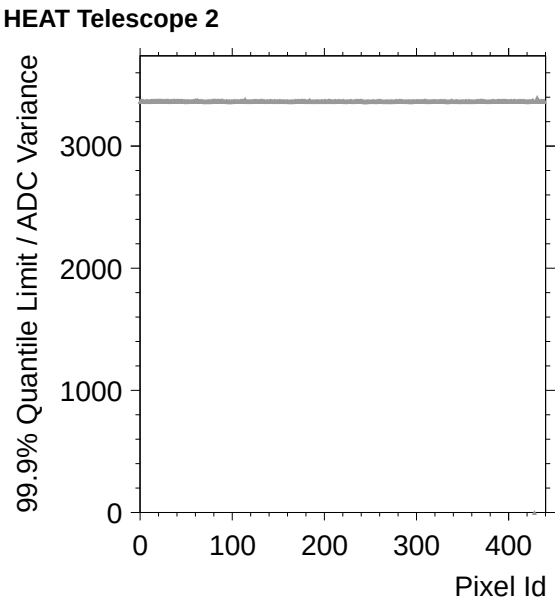
HEAT Telescope 2
99.9% Quantile Limit / ADC Variance
3000
2000
1000
0
0
100
200
300
400
Pixel Id

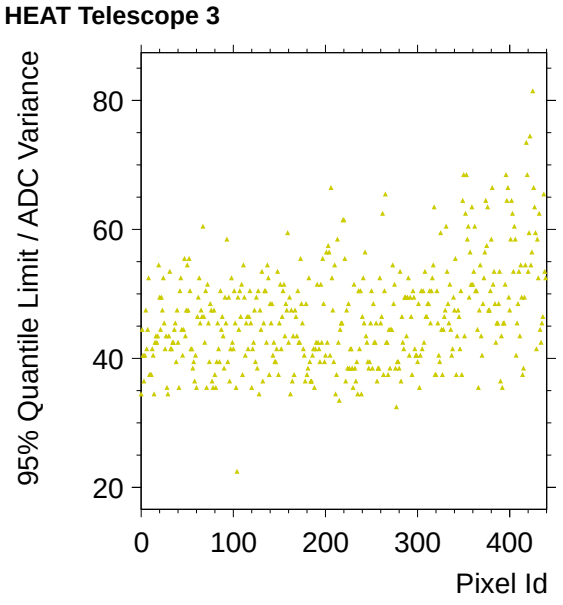
HEAT Telescope 3
95% Quantile Limit / ADC Variance
80
60
40
20
0
100
200
300
400
Pixel Id

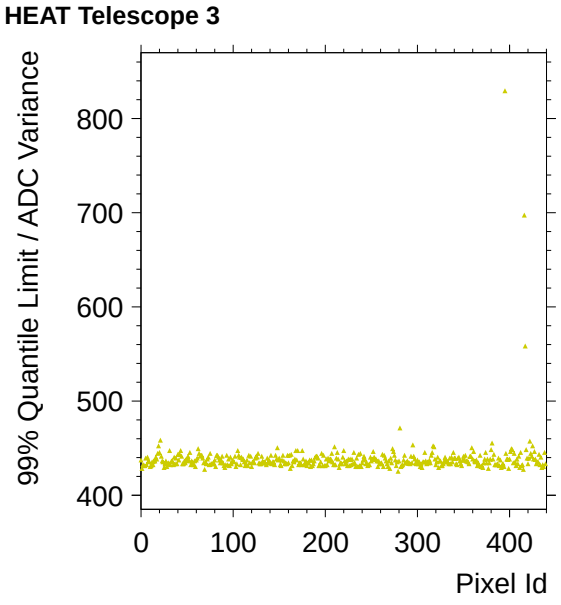
HEAT Telescope 3
99% Quantile Limit / ADC Variance
800
700
600
500
400
0
100
200
300
400
Pixel Id

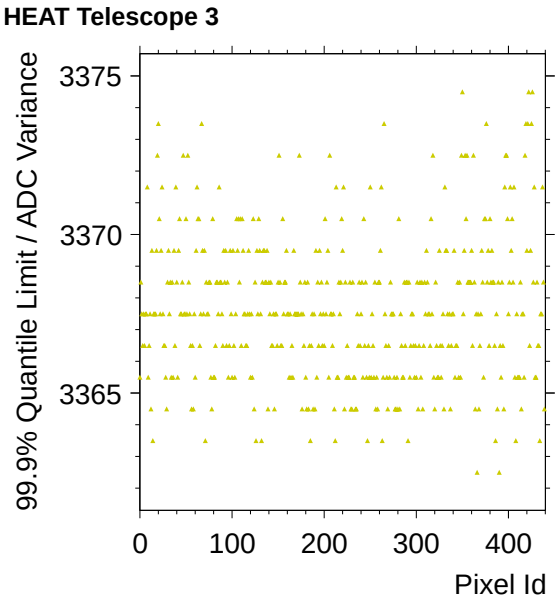
HEAT Telescope 3
99.9% Quantile Limit / ADC Variance
3375
3370
3365
0
100
200
300
400
Pixel Id

Appendix D.

Model Predictions

10000 CONEX showers per model and primary were simulated to determine the predictions for $\langle X_{\max} \rangle$ and $RMS(X_{\max})$. Therefore the CONEX showers were used directly without a detector simulation. The output was energy binned in tenth decades from 10^{17} eV to 10^{19} eV. On the resulting distributions of $\langle X_{\max} \rangle$ and $RMS(X_{\max})$ a log-linear function ($y = b + m \cdot \log_{10}(x)$) was fitted. The results of the fits are shown in tab. D.1.

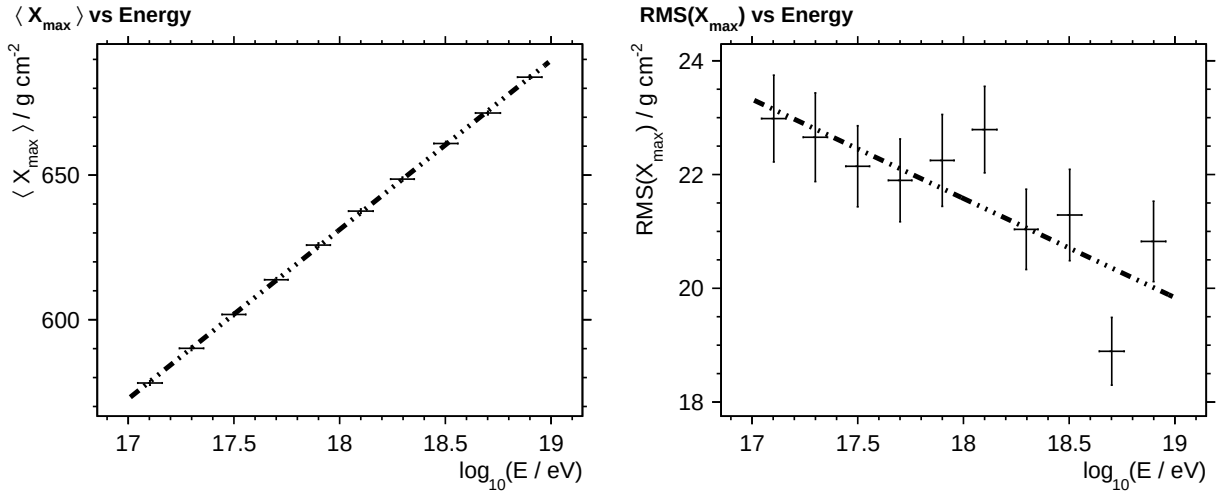

Figure D.1.: Fit on $\langle X_{\max} \rangle$ and RMS($X_{\max}$) distribution generated with CONEX from QGSJet01 hadronic interaction model for iron primaries.

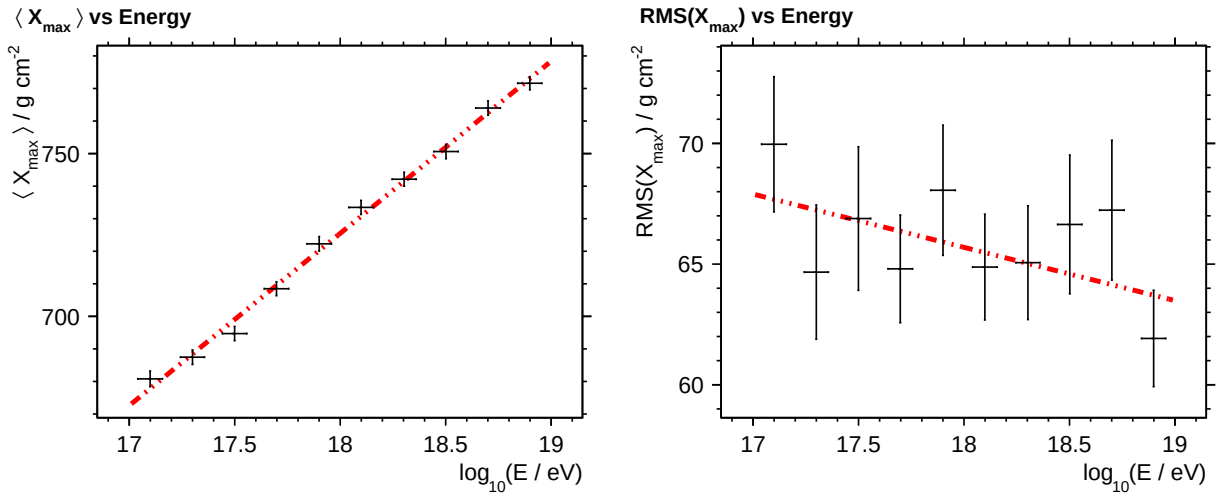

Figure D.2.: Fit on $\langle X_{\max} \rangle$ and RMS($X_{\max}$) distribution generated with CONEX from QGSJet01 hadronic interaction model for proton primaries.

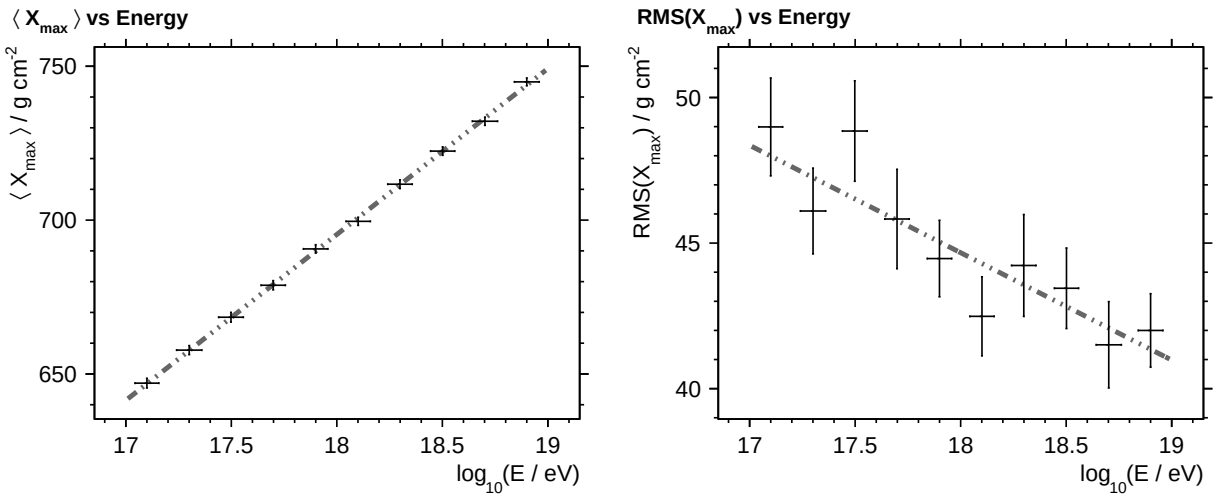

Figure D.3.: Fit on $\langle X_{\max} \rangle$ and RMS($X_{\max}$) distribution generated with CONEX from QGSJet01 hadronic interaction model for helium primaries.

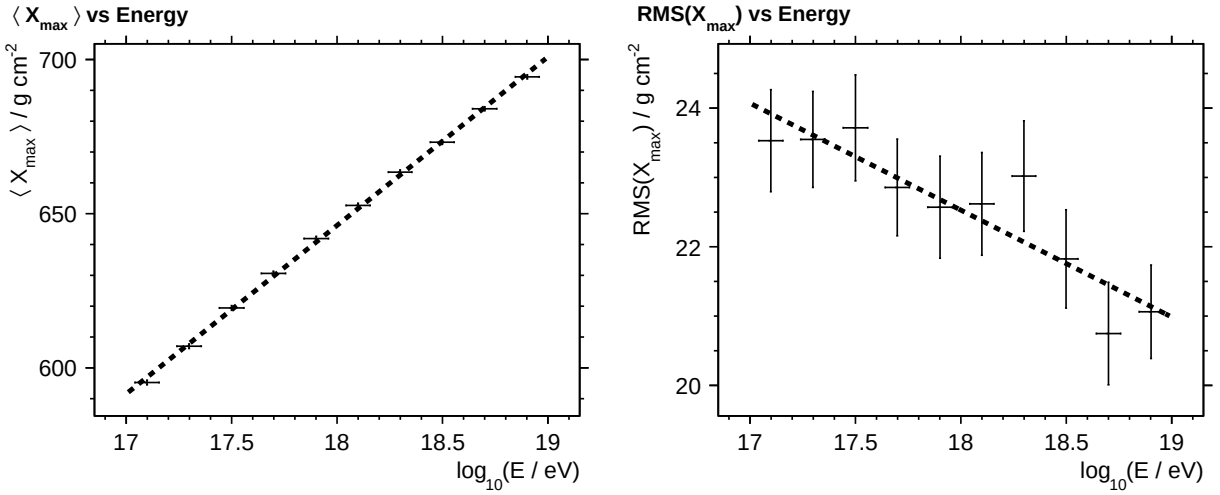

Figure D.4.: Fit on $\langle X_{\max} \rangle$ and RMS($X_{\max}$) distribution generated with CONEX from QGSJetII hadronic interaction model for iron primaries.

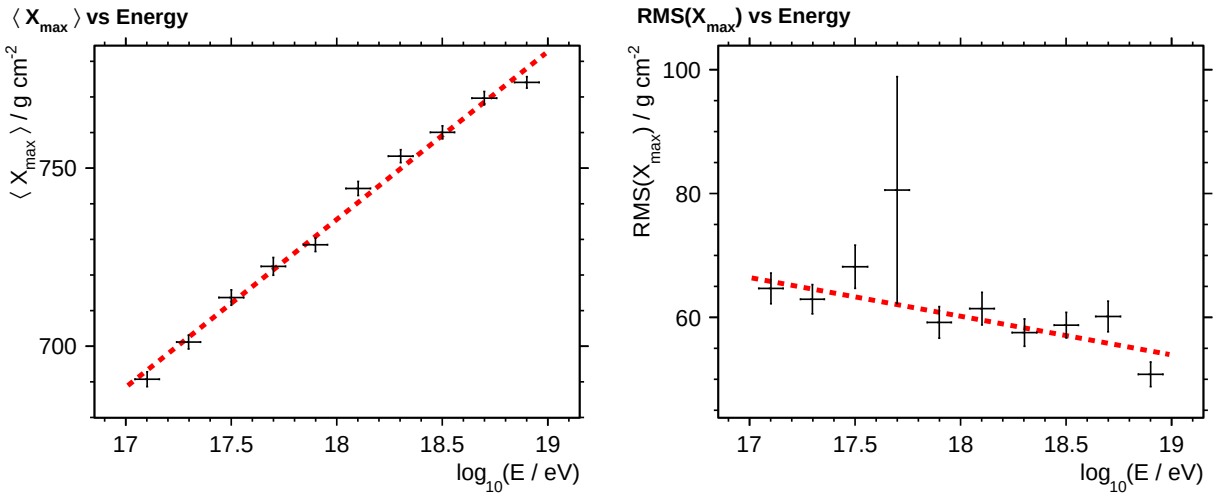

Figure D.5.: Fit on $\langle X_{\max} \rangle$ and RMS($X_{\max}$) distribution generated with CONEX from QGSJetII hadronic interaction model for proton primaries.

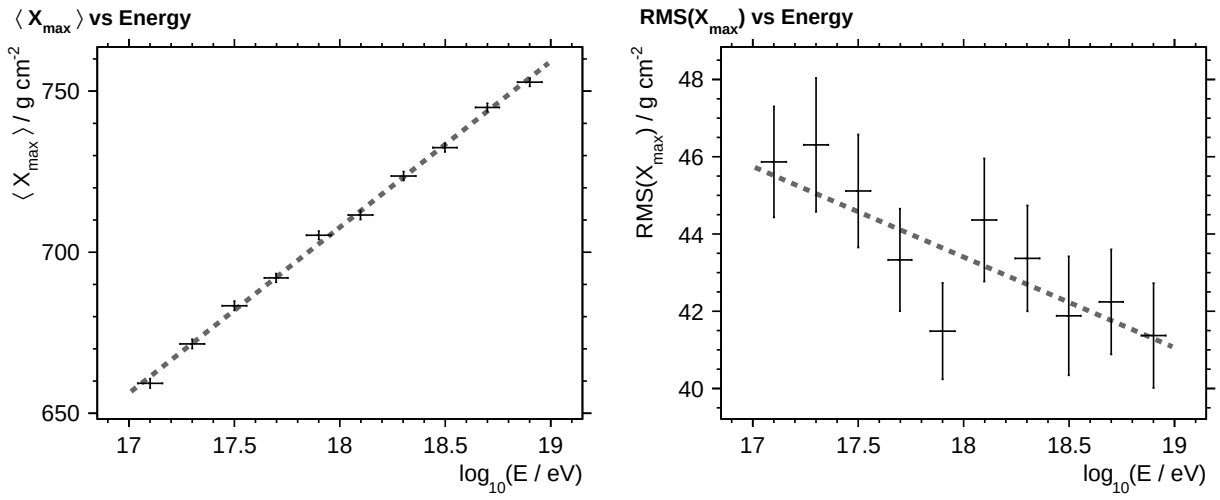

Figure D.6.: Fit on $\langle X_{\max} \rangle$ and RMS($X_{\max}$) distribution generated with CONEX from QGSJetII hadronic interaction model for helium primaries.

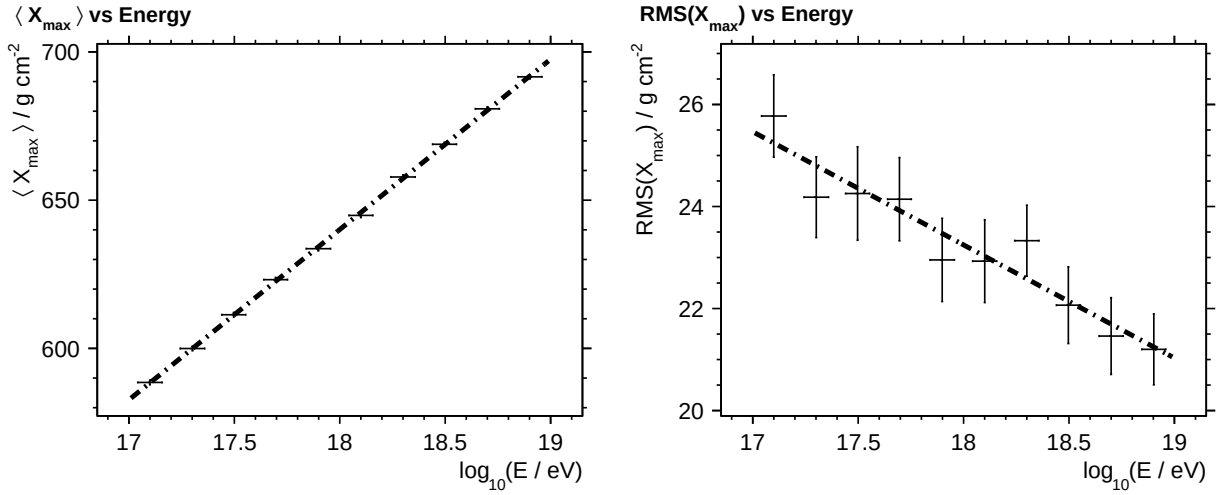

Figure D.7.: Fit on $\langle X_{\max} \rangle$ and RMS($X_{\max}$) distribution generated with CONEX from Sibyll 2.1 hadronic interaction model for iron primaries.

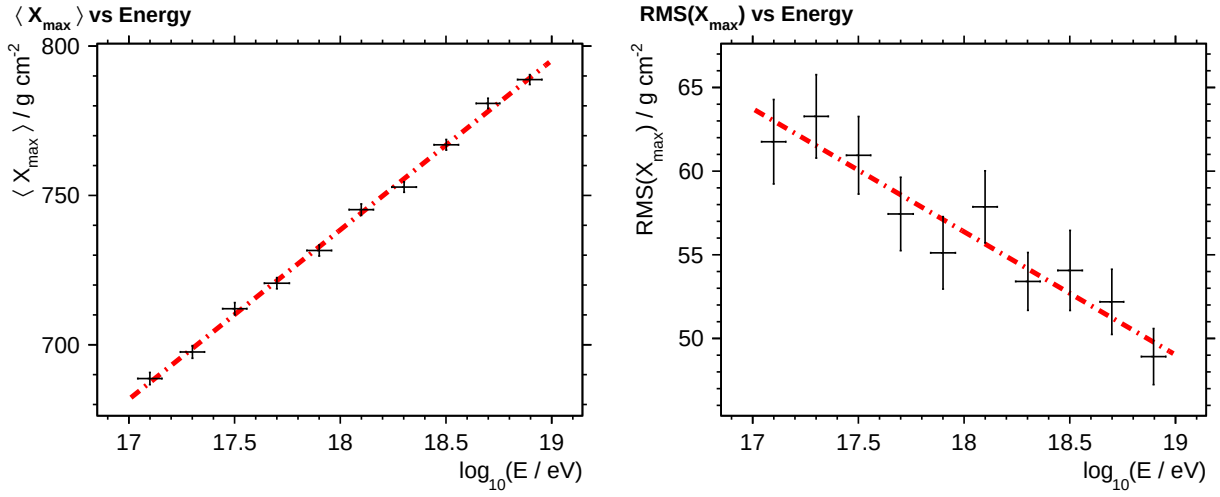

Figure D.8.: Fit on $\langle X_{\max} \rangle$ and RMS($X_{\max}$) distribution generated with CONEX from Sibyll 2.1 hadronic interaction model for proton primaries.

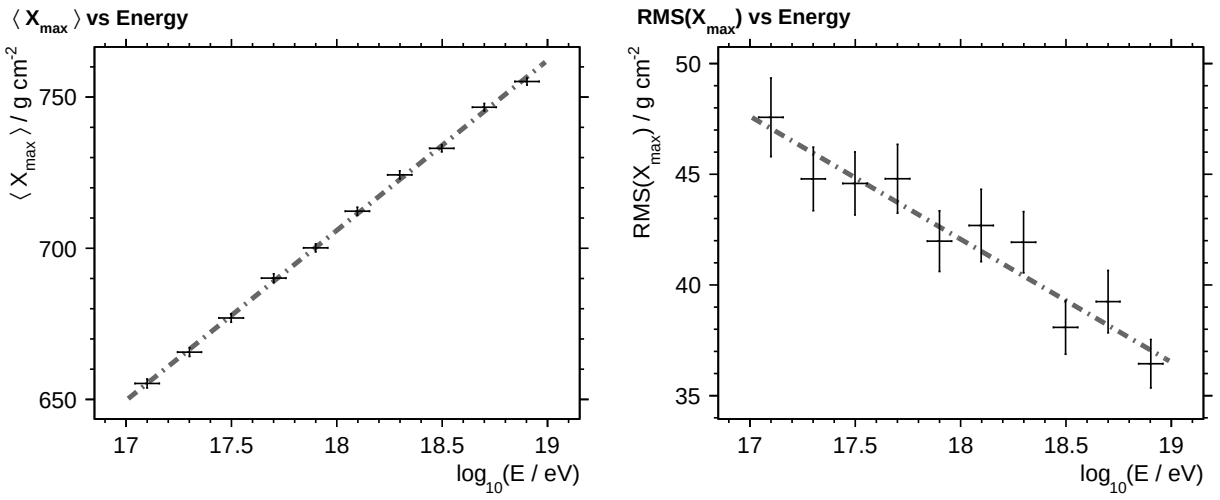

Figure D.9.: Fit on $\langle X_{\max} \rangle$ and RMS($X_{\max}$) distribution generated with CONEX from Sibyll 2.1 hadronic interaction model for helium primaries.

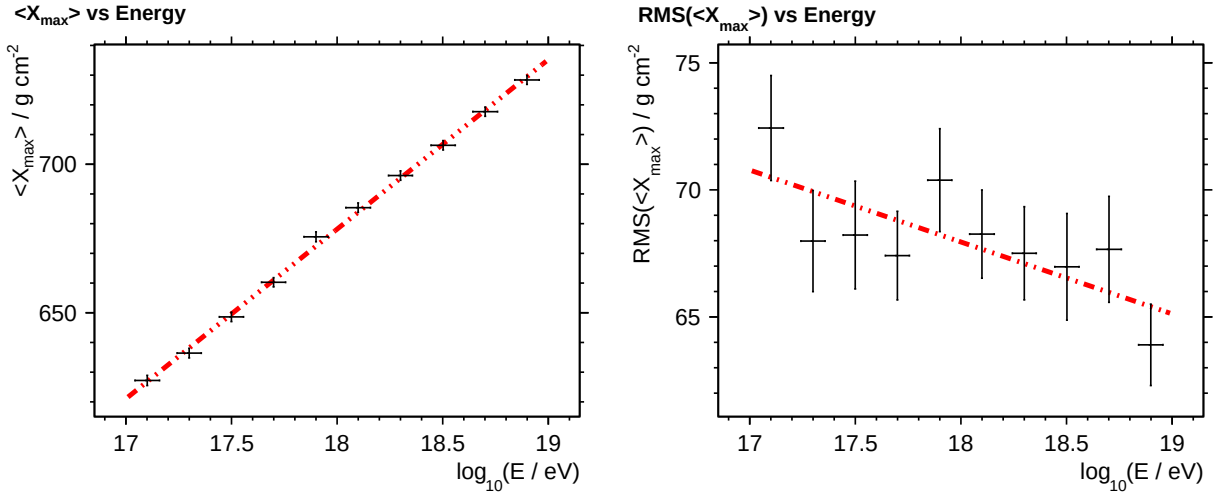

Figure D.10.: Fit on $\langle X_{\max} \rangle$ and RMS($X_{\max}$) distribution generated with CONEX from QGSJet01 hadronic interaction model for 50 % proton and 50 % iron primaries.

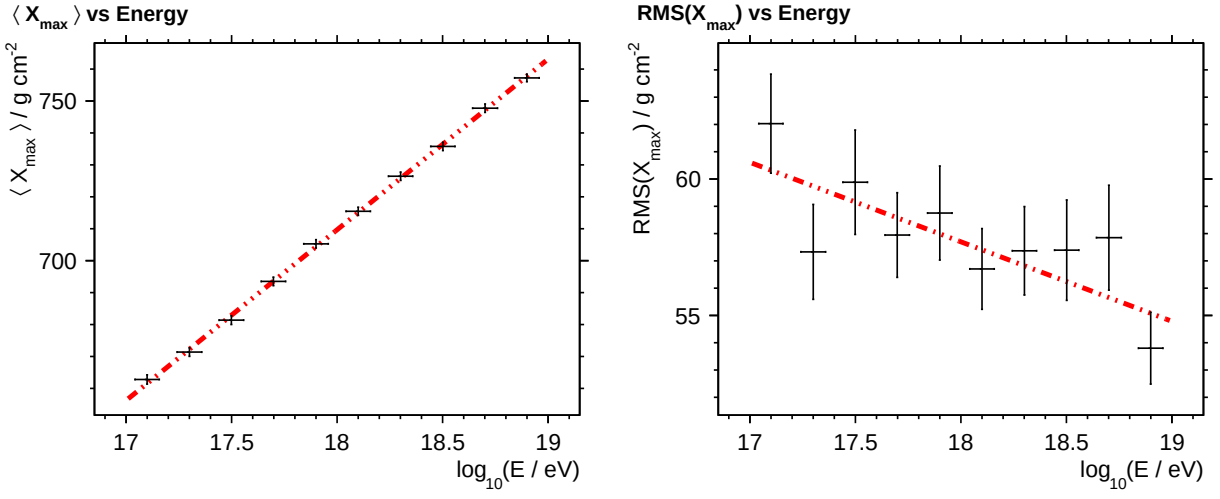

Figure D.11.: Fit on $\langle X_{\max} \rangle$ and RMS($X_{\max}$) distribution generated with CONEX from QGSJet01 hadronic interaction model for 50 % proton and 50 % helium primaries.

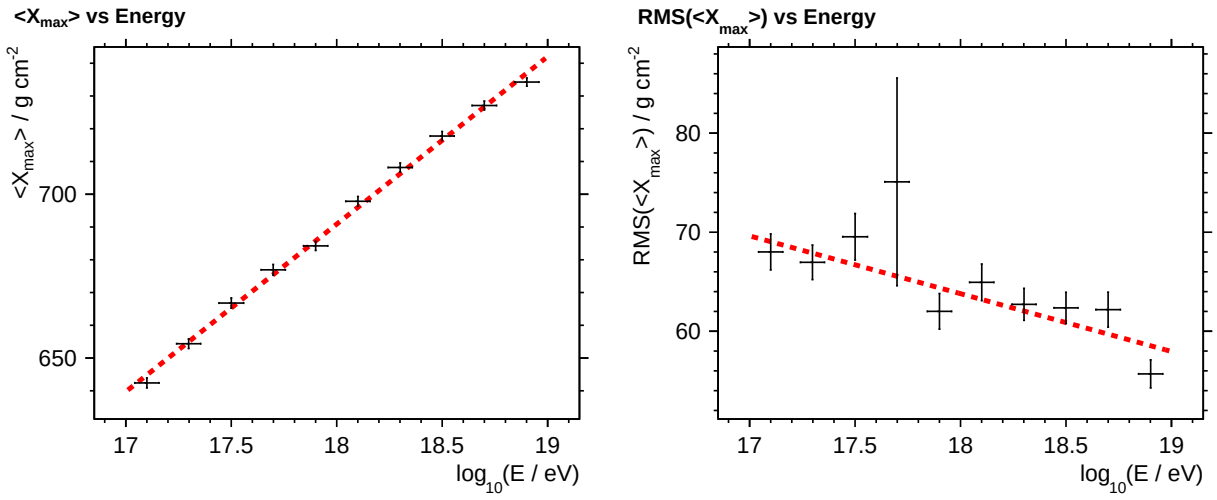

Figure D.12.: Fit on $\langle X_{\max} \rangle$ and RMS($X_{\max}$) distribution generated with CONEX from QGSJetII hadronic interaction model for 50 % proton and 50 % iron primaries.

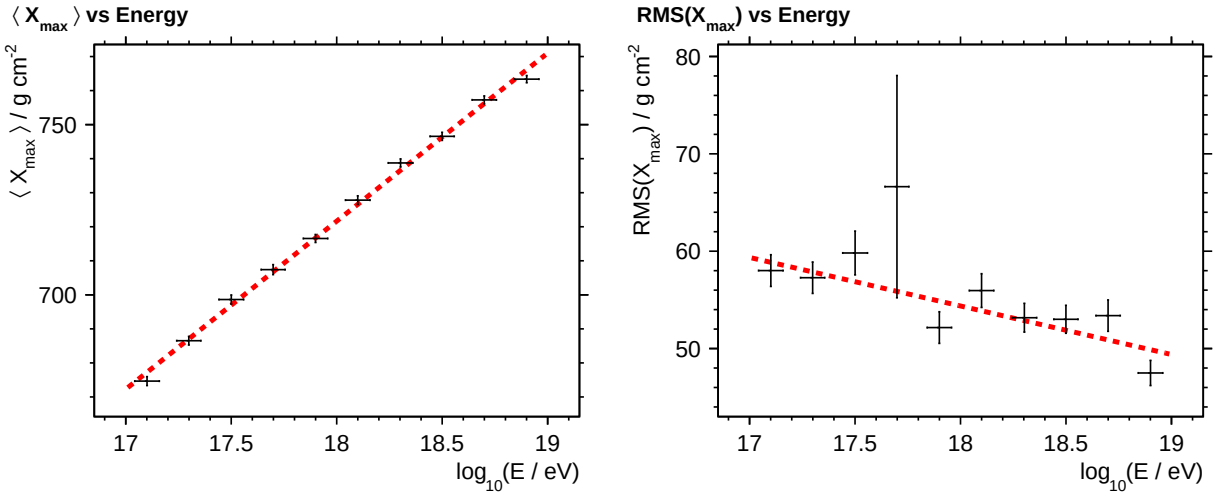

Figure D.13.: Fit on $\langle X_{\max} \rangle$ and RMS($X_{\max}$) distribution generated with CONEX from QGSJetII hadronic interaction model for 50 % proton and 50 % helium primaries.

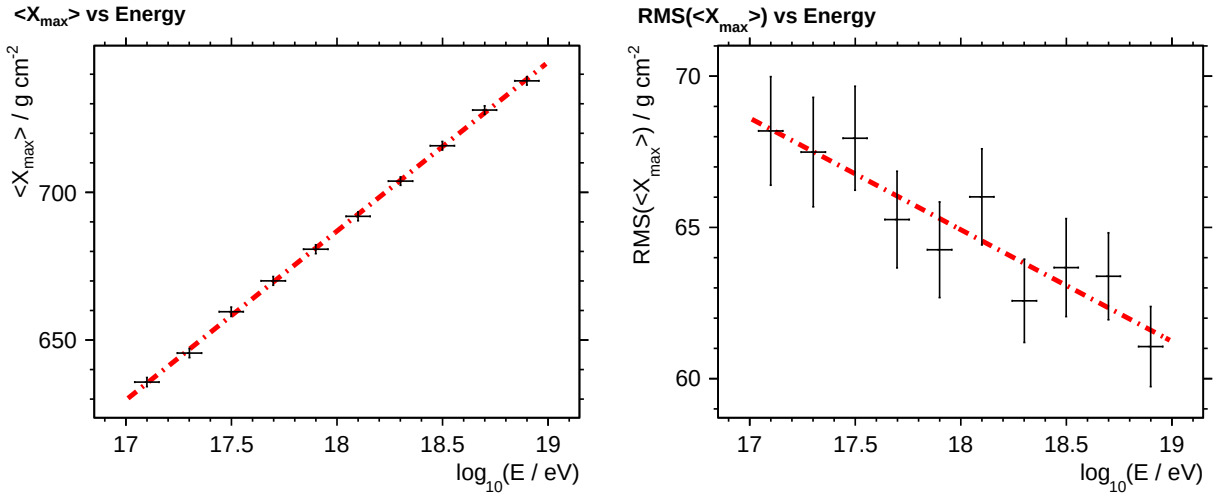

Figure D.14.: Fit on $\langle X_{\max} \rangle$ and RMS($X_{\max}$) distribution generated with CONEX from Sibyll 2.1 hadronic interaction model for 50 % proton and 50 % iron primaries.

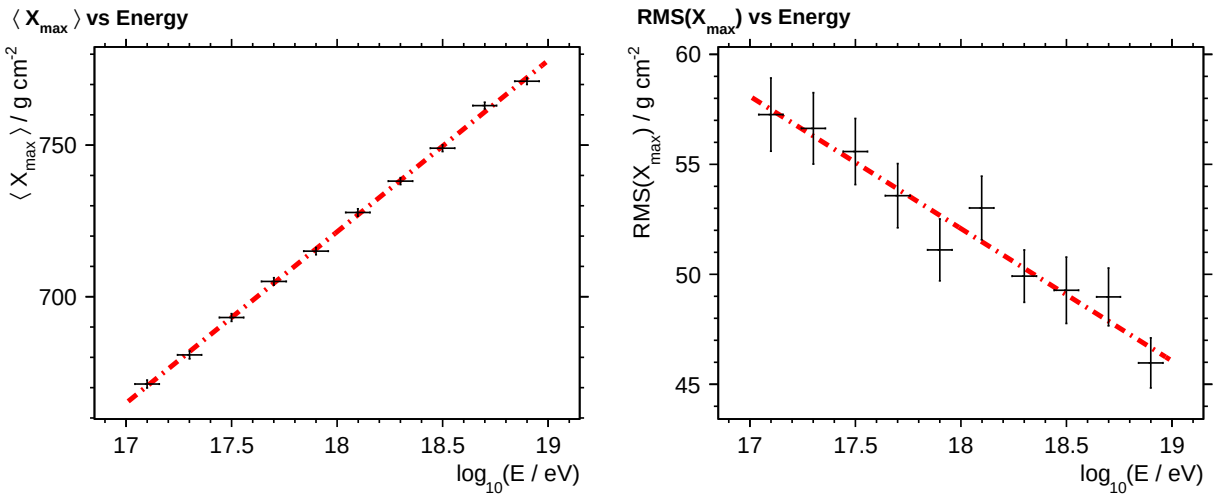

Figure D.15.: Fit on $\langle X_{\max} \rangle$ and RMS($X_{\max}$) distribution generated with CONEX from Sibyll 2.1 hadronic interaction model for 50 % helium and 50 % iron primaries.

Model	Primary	Fit on $\langle X_{max} \rangle$				Fit on RMS(X_{max})			
		b	**m**	χ^2/N_{dof}	$P(\chi^2\|N_{dof})$	**b**	**m**	χ^2/N_{dof}	$P(\chi^2\|N_{dof})$
QGSJet01	Iron	-422±7	58.5±0.4	0.4	0.9	53±7	-1.7±0.4	1.5	0.2
	Helium	-275±14	53.9±0.8	0.3	1.0	111±15	-3.7±0.8	0.7	0.7
	Proton	-227±22	52.9±1.2	1.2	0.3	105±25	-2.2±1.4	0.6	0.7
	Mixed (p/Fe)	-350±16	57.1±0.9	0.9	0.5	119±19	-2.8±1.0	0.7	0.7
	Mixed (p/He)	-252±13	53.5±0.7	0.5	0.9	110±16	-2.9±0.9	0.8	0.6
QGSJetII	Iron	-338±7	54.7±0.4	2.3	0.02	50±7	-1.5±0.4	0.4	0.9
	Helium	-219±14	51.5±0.8	1.3	0.2	86±14	-2.3±0.8	0.6	0.8
	Proton	-113±19	47.1±1.0	2.3	0.02	173±24	-6.2±1.3	1.5	0.2
	Mixed (p/Fe)	-230±14	51.2±0.8	1.8	0.06	169±17	-5.8±1.0	1.6	0.1
	Mixed (p/He)	-167±12	49.4±0.7	2.2	0.02	144±16	-5.0±0.9	1.7	0.1
Sibyll2.1	Iron	-394±7	57.4±0.4	0.6	0.8	63±8	-2.2±0.4	0.4	0.9
	Helium	-306±13	56.2±0.7	0.8	0.6	142±14	-5.6±0.8	0.6	0.8
	Proton	-283±19	56.7±1.0	1.0	0.5	189±21	-7.4±1.2	0.5	0.8
	Mixed (p/Fe)	-343±15	57.2±0.8	0.3	1.0	131±16	-3.7±0.9	0.5	0.9
	Mixed (p/He)	-296±12	56.5±0.7	0.9	0.5	160±14	-6.0±0.8	0.5	0.9

Table D.1.: Result from fits on the CONEX shower simulations. The unit of the parameters m and b is $\mathrm{g\,cm^{-2}}$.

Fitted function

$$Y(\langle E \rangle) = m \cdot \log_{10}(\langle E \rangle / \mathrm{eV}) + b \tag{D.1}$$

with Y denoting the quantities X_{max} and RMS(X_{max}).

Appendix E.

Results

E.1. Mass Composition

$\mathbf{E}$ bin / eV	$\langle \mathbf{E} \rangle$ / eV	N	$\langle \mathbf{X}_{\max} \rangle$ / g cm^{-2}			$\mathbf{RMS}(\mathbf{X}_{\max})$ / g cm^{-2}		
			value±stat.	syst.	res.	value±stat.	syst.	res.
$10^{18.38}..10^{18.62}$	$10^{18.5}$	187	741± 5	$^{+2}_{-2}$	19	57.0± 3.3	$^{+4.2}_{-4.2}$	0.5
$10^{18.12}..10^{18.38}$	$10^{18.25}$	467	727± 3	$^{+2}_{-2}$	20	53.7± 1.9	$^{+4.1}_{-4.1}$	0.5
$10^{17.88}..10^{18.12}$	10^{18}	952	716± 2	$^{+3}_{-3}$	22	57.4± 1.5	$^{+3.2}_{-3.2}$	0.5
$10^{17.62}..10^{17.88}$	$10^{17.75}$	1652	697± 2	$^{+2}_{-2}$	24	56.1± 1.1	$^{+3.5}_{-3.5}$	0.7
$10^{17.38}..10^{17.62}$	$10^{17.5}$	1924	685± 2	$^{+2}_{-2}$	26	56.3± 1.0	$^{+4.6}_{-4.6}$	0.9
$10^{17.12}..10^{17.38}$	$10^{17.25}$	1179	677± 2	$^{+4}_{-4}$	24	60.8± 1.4	$^{+4.5}_{-4.5}$	0.8
$10^{16.88}..10^{17.12}$	10^{17}	318	655± 4	$^{+7}_{-7}$	27	63± 3	$^{+4}_{-4}$	1

Table E.1.: Result from analysis of combined HEAT and Coihueco data

E.2. Detector Resolution and Reconstruction Bias

E / eV	Energy ($\Delta E/E_{true} \cdot 100$) Resolution					
	Proton			Iron		
	EPOS	QGSJetII	Sibyll	EPOS	QGSJetII	Sibyll
10^{17}	8.6±0.2	8.4±0.3	8.6±0.2	7.2±0.5	6.4±0.4	6.8±0.4
$10^{17.25}$	8.5±0.1	8.6±0.1	8.8±0.2	7.8±0.3	7.7±0.2	7.4±0.2
$10^{17.5}$	9.2±0.2	9.4±0.2	8.6±0.2	9.0±0.4	7.8±0.3	7.7±0.2
$10^{17.75}$	8.7±0.1	8.5±0.1	9.2±0.2	7.5±0.1	7.5±0.1	7.4±0.1
10^{18}	8.75±0.07	8.69±0.09	8.45±0.09	7.35±0.09	7.63±0.09	7.31±0.08
$10^{18.25}$	8.03±0.08	7.84±0.08	7.94±0.08	7.03±0.07	7.11±0.08	6.88±0.08
$10^{18.5}$	7.52±0.08	7.42±0.07	7.69±0.08	6.93±0.07	6.57±0.06	6.61±0.07

E / eV	$\langle X_{max} \rangle$ / g cm^{-2} Resolution					
	Proton			Iron		
	EPOS	QGSJetII	Sibyll	EPOS	QGSJetII	Sibyll
10^{17}	24.6±0.9	25.9±0.9	26.3±0.9	28±1	29±1	28±1
$10^{17.25}$	22.6±0.8	21.7±0.6	23.5±0.7	28.6±0.9	25.4±0.8	23.2±0.8
$10^{17.5}$	24.8±0.8	27.9±0.8	24.5±0.7	28±1	28±1	24.8±0.9
$10^{17.75}$	23.4±0.6	23.3±0.6	24.1±0.7	25.3±0.8	24.1±0.7	23.0±0.6
10^{18}	22.9±0.5	22.2±0.5	22.3±0.5	21.2±0.5	22.2±0.5	20.3±0.5
$10^{18.25}$	20.5±0.5	20.6±0.5	22.8±0.8	19.6±0.5	19.8±0.5	19.1±0.5
$10^{18.5}$	20.5±0.5	20.2±0.5	19.7±0.5	18.9±0.5	18.7±0.4	18.6±0.5

E / eV	RMS(X_{max}) / g cm^{-2} Resolution					
	Proton			Iron		
	EPOS	QGSJetII	Sibyll	EPOS	QGSJetII	Sibyll
10^{17}	0.88±0.05	0.90±0.05	0.88±0.04	1.3±0.1	0.96±0.07	1.16±0.08
$10^{17.25}$	0.77±0.03	0.64±0.03	0.67±0.03	0.93±0.06	0.83±0.04	0.80±0.04
$10^{17.5}$	0.85±0.04	0.84±0.04	0.73±0.03	1.00±0.06	0.98±0.05	0.86±0.05
$10^{17.75}$	0.64±0.03	0.62±0.03	0.71±0.03	0.78±0.03	0.66±0.03	0.62±0.03
10^{18}	0.47±0.02	0.52±0.02	0.52±0.02	0.50±0.02	0.52±0.02	0.50±0.02
$10^{18.25}$	0.47±0.02	0.47±0.02	0.80±0.02	0.48±0.02	0.46±0.02	0.46±0.01
$10^{18.5}$	0.48±0.02	0.49±0.02	0.49±0.02	0.49±0.02	0.44±0.01	0.47±0.02

Table E.2.: Detector resolution of energy, $\langle X_{max} \rangle$ and RMS(X_{max}) for each primary and primary per energy bin.

E / eV	Energy ($\Delta E/E_{true} \cdot 100$) Bias					
	Proton			Iron		
	EPOS	QGSJetII	Sibyll	EPOS	QGSJetII	Sibyll
10^{17}	-0.1±0.3	2.1±0.3	3.1±0.3	-12.1±0.5	-9.0±0.4	-8.8±0.4
$10^{17.25}$	-0.7±0.2	1.3±0.2	1.6±0.2	-10.8±0.3	-8.0±0.2	-7.9±0.2
$10^{17.5}$	0.0±0.3	0.8±0.3	2.1±0.3	-9.3±0.3	-7.5±0.3	-6.8±0.3
$10^{17.75}$	-0.8±0.2	0.8±0.2	1.5±0.2	-8.3±0.1	-6.5±0.1	-6.9±0.1
10^{18}	-1.39±0.09	-0.3±0.1	0.6±0.1	-7.8±0.1	-5.9±0.1	-5.9±0.1
$10^{18.25}$	-1.32±0.09	-0.68±0.09	0.03±0.09	-7.29±0.08	-5.90±0.08	-5.60±0.08
$10^{18.5}$	-2.27±0.09	-1.32±0.08	0.37±0.09	-7.38±0.08	-5.76±0.07	-5.24±0.07

E / eV	$\langle X_{max} \rangle$ / g cm^{-2} Bias					
	Proton			Iron		
	EPOS	QGSJetII	Sibyll	EPOS	QGSJetII	Sibyll
10^{17}	-4.9±0.9	-6±1	-2±1	4±2	0±2	0±2
$10^{17.25}$	-1.9±0.4	-1.2±0.4	-2.5±0.5	1.2±0.9	3.1±0.7	1.7±0.7
$10^{17.5}$	-2.6±0.8	-1.8±0.8	-4.3±0.7	-1±1	2±1	-0.6±0.8
$10^{17.75}$	-4.8±0.4	-3.3±0.4	-3.7±0.4	-1.7±0.5	-0.9±0.4	-1.4±0.4
10^{18}	-6.7±0.2	-5.7±0.3	-6.4±0.3	-4.3±0.3	-3.3±0.3	-4.8±0.3
$10^{18.25}$	-6.8±0.2	-5.9±0.2	-6.8±0.3	-5.1±0.2	-4.6±0.2	-5.4±0.2
$10^{18.5}$	-7.3±0.2	-6.7±0.2	-6.3±0.2	-6.0±0.2	-5.8±0.2	-5.6±0.2

E / eV	RMS(X_{max}) / g cm^{-2} Bias					
	Proton			Iron		
	EPOS	QGSJetII	Sibyll	EPOS	QGSJetII	Sibyll
10^{17}	0±2	6±2	5±2	9±2	11±2	12±2
$10^{17.25}$	4±2	3±1	3±1	15±1	10±1	7±1
$10^{17.5}$	2±2	7±2	4±2	17±1	13±1	10±1
$10^{17.75}$	5±1	5±1	5±1	12±1	10.5±0.9	8.4±0.9
10^{18}	4±1	4±1	5±1	9.4±0.7	8.7±0.8	7.8±0.8
$10^{18.25}$	4±1	4±1	3±1	8.7±0.7	7.2±0.7	6.6±0.7
$10^{18.5}$	4±1	4±1	4±1	8.1±0.7	7.0±0.6	7.3±0.7

Table E.3.: Reconstruction bias of energy, $\langle X_{max} \rangle$ and RMS(X_{max}) for each primary and primary per energy bin.

Erklärung

Hiermit versichere ich, dass ich diese Arbeit einschließlich beigefügter Zeichnungen, Darstellungen und Tabellen selbstständig angefertigt und keine anderen als die angegebenen Hilfsmittel und Quellen verwendet habe. Alle Stellen, die dem Wortlaut oder dem Sinn nach anderen Werken entnommen sind, habe ich in jedem einzelnen Fall unter genauer Angabe der Quelle deutlich als Entlehnung kenntlich gemacht.

Aachen, den 09. Januar 2012

Marcel Straub